
Hybrid Noise Simulation for Enclosed Configurations

Hybride Lärmsimulation von eingeschlossenen Konfigurationen

Zur Erlangung des akademischen Grades Doktor-Ingenieur (Dr.-Ing.)

genehmigte Dissertation von Kilian Lackhove, M.Sc. aus Osnabrück

Tag der Einreichung: 2018-04-09, Tag der Prüfung: 2018-06-19

Darmstadt – D 17

1. Gutachten: Prof. Dr.-Ing. J. Janicka
2. Gutachten: Prof. Dr. rer. nat. M. Schäfer



TECHNISCHE
UNIVERSITÄT
DARMSTADT



Hybrid Noise Simulation for Enclosed Configurations
Hybride Lärmsimulation von eingeschlossenen Konfigurationen

Genehmigte Dissertation von Kilian Lackhove, M.Sc. aus Osnabrück

1. Gutachten: Prof. Dr.-Ing. J. Janicka
2. Gutachten: Prof. Dr. rer. nat. M. Schäfer

Tag der Einreichung: 2018-04-09

Tag der Prüfung: 2018-06-19

Darmstadt – D 17

Bitte zitieren Sie dieses Dokument als:

URN: urn:nbn:de:tuda-tuprints-urn:nbn:de:tuda-tuprints-76117

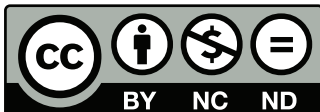
URL: <http://tuprints.ulb.tu-darmstadt.de/id/eprint/7611>

Dieses Dokument wird bereitgestellt von tuprints,

E-Publishing-Service der TU Darmstadt

<http://tuprints.ulb.tu-darmstadt.de>

tuprints@ulb.tu-darmstadt.de



Die Veröffentlichung steht unter folgender Creative Commons Lizenz:
Namensnennung – Nicht kommerziell – Keine Bearbeitungen 4.0 International
<http://creativecommons.org/licenses/by-nc-nd/4.0/>

Preface

This thesis is the result of my work as a doctoral candidate at the Institute for Energy and Power Plant Technology at the TU Darmstadt. I would like to express my deepest gratitude to the head of the institute, Prof. Dr. Johannes Janicka for this opportunity and his support. I very much appreciate his confidence in me, the freedom in almost every aspect of my work and the many opportunities to present it outside of TU Darmstadt. I wish to thank Prof. Dr. Michael Schäfer for his interest in my work and his willingness to report on this thesis.

Moreover, I would like to express my gratitude to my contacts at Rolls-Royce for their continuous support and collaboration. Dr. Max Staufer laid the foundation of this thesis by pointing me towards Nektar++. He and Dr. Ruud Eggels accompanied my work from the first day on with helpful feedback and inspirational discussions. Dr. André Fischer offered his invaluable expertise in acoustics and gave advice regarding publications of all kinds.

I am very grateful to the Nektar++ team, including Prof. Dr. Spencer Sherwin, Prof. Dr. Mike Kirby, Dr. David Moxey and Dr. Chris Cantwell for welcoming me in their developer group and supporting my work on the project.

My special thanks are extended to my numerous colleagues, who contributed to the friendly and productive atmosphere at the institute. I would like to thank Dr. Guido Künne for his counseling on reacting flow simulations, Félix Raynaud for guiding my first steps at the institute and Dr. Timo Klenke for his previous work on hybrid CAA methods. I am particularly grateful to my colleagues Dr. Ayane Johchi, Carl-Philipp Ding, Dr. Jens Hermann, Maresa Tannich, Robert Knappstein and Wibke Leudesdorff for their friendship, their team spirit and the many insightful discussions.

Furthermore, I would like to express my gratitude to my parents and my family for their outright support and encouragement. My heartfelt appreciation goes to my wife Julia, who steadily lifted my spirit and patiently stood by my side, especially during the final months of this work.

Darmstadt, April 2018

Kilian Lackhove



Contents

1	Introduction	1
1.1	Motivation	1
1.2	State of Research	2
1.3	Aims and Scope of this Work	5
1.4	Structure of this Work	6
2	Mathematical Model	9
2.1	Governing Equations for Fluid Dynamics	9
2.1.1	Conservation of Mass	9
2.1.2	Conservation of Momentum	10
2.1.3	Species Transport	10
2.1.4	Conservation of Energy	11
2.1.5	Equation of State	12
2.1.6	The Low Mach Number Approximation	13
2.2	Turbulent Flows	14
2.2.1	Turbulent Scales	15
2.2.2	Turbulence Modeling	17
2.2.2.1	RANS Models	17
2.2.2.2	Large Eddy Simulation	18
2.3	Reactive Flows	22
2.3.1	Reaction Kinetics	22
2.3.2	Premixed Flames	24
2.3.3	Combustion Modeling	26
2.3.3.1	Flamelet Generated Manifolds	27
2.3.3.2	Artificially Thickened Flame	31
2.4	Governing Equations for Aeroacoustics	33
2.4.1	Acoustic Perturbation Equations	34
2.4.2	Acoustic Perturbation Equations for Reacting Low Mach Number Flows	35
2.4.3	Acoustic Perturbation Equations in Characteristic Variables	37
2.4.4	Acoustic Feedback onto the Low Mach Number Flow Govern- ing Equations	39

3	Numerical Implementation of the Acoustics Solver	41
3.1	Spectral/hp Element Method	42
3.1.1	h -type Extension	44
3.1.2	p -type Extension	45
3.1.3	Integration	50
3.1.4	Differentiation	52
3.1.5	Forward- and Backward Transform	54
3.2	Discontinuous Galerkin Formulation	56
3.2.1	Lax-Friedrichs and Local Lax-Friedrichs Flux	59
3.2.2	First Order Upwind Flux	60
3.3	Boundary Conditions	62
3.3.1	Rigid Wall Boundary	63
3.3.2	Farfield Boundary	64
3.4	Temporal Discretization	65
3.5	Solution Algorithm	66
3.6	Verification	67
3.6.1	Method of Manufactured Solution	67
3.6.2	Dispersion and Diffusion Errors	72
3.6.3	Application to a Spinning Vortex Pair	74
4	Numerical Implementation of the Flow Solver	77
4.1	Finite Volume Method	78
4.1.1	Integration	78
4.1.2	Advective and Diffusive Fluxes	79
4.1.3	Differentiation	80
4.2	Temporal Discretization	81
4.3	Pressure-Velocity Coupling	82
4.3.1	Interpolation of Velocity Corrections	83
4.4	Solution Algorithm	85
5	Implementation of the Coupling Layer	87
5.1	Preparation of the Required Fields	89
5.2	Data Transfer	89
5.3	Spatial Representation	90
5.3.1	Forward Coupling	90
5.4	Temporal Interpolation	95
5.5	Full Coupling Algorithm	96
6	Application to a Half-Dump Combustor	99
6.1	Configuration	99

6.2	Numerical Setup	101
6.3	Flow Fields	105
6.4	Noise Sources	106
6.5	Acoustic Fields	108
6.6	Sampling Resolution and Filter Width	112
6.7	Acoustic Feedback	114
6.8	Summary	114
7	Application to a Swirl Stabilized Burner	117
7.1	Configuration	118
7.2	Numerical Setup	120
7.3	Flow Fields	124
7.3.1	Operating Point OP-16-2	124
7.3.2	Operating Point OP-13-5	125
7.4	Noise sources	128
7.5	Acoustic Fields	129
7.5.1	Acoustic Modes	129
7.5.2	OP-16-2	133
7.5.3	OP-13-5	134
7.6	Sampling Resolution and Filter Width	136
7.7	Computational Efficiency	136
7.8	Summary	137
8	Conclusions	139
	Bibliography	141



List of Figures

2.1	Spectrum of the turbulent kinetic energy over progressively smaller eddies	16
2.2	Qualitative structure of a premixed propane flame.	24
2.3	Laminar and turbulent flame fronts.	25
2.4	A propane-flamelet at $Z = 0.6$, $p = 2.01$ bar and $T = 315$ K	28
2.5	Propane manifold for $p = 2.01$ bar and $T = 315$ K.	29
3.1	One-dimensional modal expansion bases with a polynomial order of $P = 5$	46
3.2	Representation of a triangular element in global, local and collapsed coordinates.	52
3.3	Direction and location of the relevant variables at the element interface.	58
3.4	Direction and location of the relevant variables at the boundary for the element Ω_e	62
3.5	Flow Diagram of the CAA Solution Algorithm for a single time step.	66
3.6	Velocity perturbations of the two-dimensional MMS.	69
3.7	L_2 errors for the 2D manufactured solution.	70
3.8	L_2 errors for the 3D manufactured solution.	71
3.9	Dispersion and diffusion errors obtained with local Lax-Friedrichs and first order upwind Riemann solvers.	74
3.10	Normalized acoustic pressure for $\Gamma/(cr_0) = 1.0$ and $Ma_r = 0.0795$ at $t = 1$ s.	76
4.1	CDS Interpolation at the face center.	80
4.2	Flow diagram of the SIMPLE algorithm with outer iteration counter variable m	85
5.1	Schematic of the bi-directional coupling with exchanged fields during forward and backward coupling steps.	88
5.2	Schematic of the three stage coupling strategy.	92
5.3	Normalized transfer function of the linear differential filter (5.3).	94
5.4	Implementation of the coupling algorithm.	97

6.1	Schematic overview of the half-dump combustor geometry.	100
6.2	CAA (blue) and CFD (green) domains.	101
6.3	Detail of the CFD and CAA meshes in the vicinity of the step.	102
6.4	CAA mesh.	103
6.5	Filtered and extrapolated representation of baseflow velocity \tilde{u}_1 within the CAA.	104
6.6	Mean axial velocity and temperature fields. Slice through the $x_3 = 0$ plane.	105
6.7	Mean velocity profiles at different locations.	106
6.8	Instantaneous acoustic source term as represented in CFD and CAA using different scales. Slice through the $x_3 = 0$ plane.	107
6.9	Spectrum of the integral acoustic source term $\Upsilon(f)$	108
6.10	Instantaneous acoustic pressure field. Slice through the $x_3 = 0$ plane.	108
6.11	Noise Spectra at different microphone locations obtained from the experiments and the current simulation.	110
6.12	Normalized acoustic pressure amplitude $K_{pa}(\mathbf{x})$ at the phase that corresponds to the largest amplitudes for two eigenmodes.	111
6.13	Noise Spectra at $x_1 = 0.63$ m obtained from the experiments, the current simulation and from the simulation published by Klenke et al. [67].	112
6.14	Noise Spectra at $x_1 = 0.63$ m obtained from the LES-CAA at different filter widths for $\tilde{\mathbf{u}}$ and $\bar{\rho}$	113
6.15	Noise Spectra at $x_1 = 0.63$ m obtained from the LES-CAA with and without oversampling.	113
6.16	Spectra of acoustic pressure p^a from CAA and modified hydrodynamic pressure $\overline{p^{\text{mod}}}$ from CFD, using uni-directional coupling and bi-directional coupling at $x_1 = 0.63$ m.	114
7.1	Considered geometry of the CESAM-HP test rig.	119
7.2	Regular tetrahedron equivalent edge length $h = \sqrt[3]{12/\sqrt{2}V}$ for CAA (blue) and CFD (green) meshes.	120
7.3	Instantaneous ratio of resolved to total turbulent kinetic energy for OP-13-5 and OP-16-2.	121
7.4	Instantaneous Thickening Factor for OP-13-5 and OP-16-2.	121
7.5	Mean axial velocity and temperature fields for OP-16-2 obtained from current LES (slice through the $x_3 = 0$ plane).	124
7.6	Axial velocity spectrum at $\mathbf{x} = [0.01, 0.015, 0]^T$ m for OP-16-2.	125
7.7	Mean axial velocity and temperature fields for OP-13-5 obtained from current LES (slice through the $x_3 = 0$ plane).	126

7.8 Mean vertical velocity $\langle \tilde{u}_2 \rangle$ and directions of the planar mean velocity projection inside premixing duct and swirler ducts.	127
7.9 Instantaneous CO mass fractions for OP-13-5, 34544 time steps (86.36 ms) apart.	127
7.10 Instantaneous noise source field for OP-16-2.	128
7.11 Noise sources spectra for OP-16-2 and OP-13-5. Original LES values from [136].	129
7.12 Sampling locations for the different spectra.	130
7.13 Noise spectra obtained from LES-CAA for OP-16-2 at different axial locations.	131
7.14 Normalized acoustic pressure amplitudes $K_{pa}(\mathbf{x})$	132
7.15 Noise spectra for OP-16-2.	133
7.16 Noise spectra for OP-13-5.	135
7.17 Noise spectra for OP-16-2, obtained with the presented hybrid CAA method using different filter widths and sampling resolutions.	136
7.18 Normalized histogram of CAA waiting times for a single run.	137





List of Tables

- 3.1 Different choices of weighting functions $v_j(\mathbf{x})$ and their corresponding projections. 44
- 3.2 Upper bounds in cartesian and collapsed coordinates for different three-dimensional element types. 48

- 6.1 Unstable operating point of the generic combustor in the current simulation. 101

- 7.1 Investigated operating points of the CESAM-HP test rig. 119



Nomenclature

Latin Uppercase		Unit
A	Coefficient Matrix	*
B^e	Elemental Basis Matrix	-
C	Progress Variable	-
\mathcal{D}	Diffusion Coefficient	m^2/s
\mathcal{E}	Efficiency Function	-
\mathcal{E}	Error	*
\mathcal{F}	Thickening Factor	-
\mathcal{F}	Discrete Fourier Transform	*
F_i	Flux Vector of Direction i	*
F^R	Numerical Flux Vector	*
$F^{C/D}$	Convective (C) and Diffusive (D) Flux Vectors	*
\mathcal{G}	Filtering Operator	*
\mathbb{G}	Generic Operator	*
H	Vector of Characteristic Variables	*
J	Jacobian	*
K^e	Elemental Inner Product Matrix	-
L_p	Sound Pressure Level	dB
Le_k	Lewis Number of the Species k	-
L_i	Matrix of Eigenvectors for Direction i	*
Ma	Mach Number	-
M^e	Elemental Mass Matrix	-

\mathcal{M}_k	Molecular Mass	kg/mol
N_{CV}	Number of Control Volumes	-
N_{DOF}	Number of Degrees of Freedom	-
N_{el}	Number of Elements	-
N_R	Number of Reactions	-
N_S	Number of Species	-
P_i	Polynomial Order of Direction i	-
$P_p^{\alpha,\beta}$	Jacobi Polynomial of Order p	-
Q_i	Number of Quadrature Points of Direction i	-
R	Residual	*
\mathcal{R}	Reflection Coefficient	-
Re	Reynolds Number	-
Re_t	Turbulent Reynolds Number	-
R_s	Specific Gas Constant	J/(kg K)
R_u	Universal Gas Constant	J/(kg mol)
S	Surface	m ²
\mathcal{S}	Flame Sensor	-
Sc_k	Schmidt Number of the Species k	-
$Sc_{t,k}$	Turbulent Schmidt Number of the Species k	-
S_{ij}	Rate of Strain	1/s
T	Temperature	K
\mathbf{U}	Solution Vector	*
\mathbf{W}	Source Term Vector	*
Y_k	Mass Fraction of Species k	-
\mathcal{Z}	Mixture Fraction	-

Latin Lowercase		Unit
\mathbf{b}^e	Internal Flux Vector	*
c	Speed of Sound	m/s
c_p	Specific Heat Capacity at Constant Pressure	J/(kg K)
\mathbf{c}^e	Numerical Flux Vector	*
\mathbf{e}_i	Unit Vector of Direction i	-
f	Frequency	Hz
\mathbf{g}, g_i	Body Force	m/s ²
h	Specific Enthalpy	J/kg
$\Delta h_{f,k}$	Enthalpy of Formation of the Species k	J/kg
h	Mesh Spacing	m
Δh_{filt}	Filter Width	m
\mathcal{h}	Characteristic Variable	*
k	Wave Number	1/m
\mathcal{K}	Turbulent Kinetic Energy	m ² /s ²
l	Length	m
ℓ_p	Lagrange Polynomial of the order p	-
m	Mass	kg
\mathbf{n}, n_i	Normal Vector	-
p	Pressure	Pa
p^{dyn}	Hydrodynamic Pressure	Pa
p^{mod}	Modified Pressure	Pa
p^{stat}	Static Pressure	Pa
q	Generic Quantity	*
s_l	Laminar Flame Speed	m/s
s_t	Turbulent Flame Speed	m/s

t	Time	s
\mathbf{u}, u_i	Velocity	m/s
v_j	Weighting Functions	-
w_i	Quadrature Weights	-
\mathbf{x}, x_i	Location	m
x_q	Node of a Lagrange Polynomial	-

Greek Uppercase

Unit

Λ_i	Matrix of Eigenvalues for Direction i	*
Φ	Equivalence Ratio	-
Φ_i	Expansion Function i	-
Φ_p^e	Element-wise Expansion Function p	-
Υ	Integral Density Fluctuation	kg/s
Ω	Computational Domain	m ³
Ω_e	Elemental Domain	m ³
Ω_{st}	Standard Element Domain	-

Greek Lowercase

Unit

γ	Isentropic Exponent	-
δ_1	Laminar Flame Thickness	m
η, η_i	Collapsed Coordinate	-
η_K	Kolmogorov Length Scale	m
θ_i	Time Stage Values	*
κ	Thermal Conductivity	W/(mK)
λ	Wave Length	m
$\Delta\lambda$	Filter Width	m

λ_i	i -th Eigenvalue	*
μ	Dynamic viscosity	kg/(s m)
ν	Kinematic Viscosity	m ² /s
ν_t	Turbulent Kinematic Viscosity	m ² /s
ξ, ξ_i	Local Coordinate	-
ξ_j, ξ_{ij}	Quadrature Point j of Direction i	-
ρ	Density	kg/m ³
ρ_e	Excess Density	kg/m ³
τ, τ_{ij}	Viscous Stress Tensor	kg/(m s ²)
$\tau^{sgs,h}$	Subgrid Enthalpy Tensor	J m/(s kg)
$\tau_{ij}^{sgs,u}$	Subgrid Stress Tensor	m ² /s ²
$\tau_k^{sgs,Y}$	Subgrid Species Tensor	m/s
ϕ_p	Local Expansion Function	-
ϕ_{pqr}	Tensorial Expansion Basis	-
ψ_p	Modified Expansion Basis	-
ω	Angular Frequency	1/s
$\dot{\omega}_c$	Acoustic Source Term	kg/(m ³ s)
$\dot{\omega}_{c\&e}$	Acoustic Source Term	Pa/s
$\dot{\omega}_e$	Acoustic Source Term	Pa/s
$\dot{\omega}_m$	Acoustic Source Term	m/s ²
$\dot{\omega}_k$	Chemical Source Term of the Species k	kg/(m ³ s)
$\dot{\omega}_h$	Enthalpy Source Term	J/(m ³ s)

Mathematical Operators, Subscripts and Superscripts

δ_{ij}	Kronecker Delta
$\ \square\ $	Euclidean or L^2 Norm

$(\square, \square)_\Omega$	Inner Product over Domain Ω
\square^δ	Approximation
$\hat{\square}$	Complex Amplitude of a Fourier Component
$\check{\square}_i$	Expansion Coefficient of Mode i
$\check{\square}_p^e$	Element-Wise Expansion Coefficient of Mode p
$\langle \square \rangle$	Temporal Mean
\square'	Temporal Fluctuation
\square_{rms}	Temporal Standard Deviation (Root Mean Square)
$\bar{\square}$	Spatial Filter
\square''	Subgrid Part of the Spatial Filter
$\tilde{\square}$	Density Weighted Spatial Filter
\square^{sgs}	Subgrid Part of the Density Weighted Spatial Filter
\square^a	Acoustic Part
\square^{loMa}	Low Mach Number Part
\square_{tab}	Quantity Obtained from Chemistry Table
\square_{int}	Quantity Obtained from Pre-Integrated Chemistry Table

Abbreviations

APE	Acoustic Perturbation Equations
ATF	Artificially Thickened Flame
CAA	Computational Aeroacoustics
CDS	Central Differences Scheme
CFD	Computational Fluid Dynamics
CV	Control Volume
DG	Discontinuous Galerkin
DNC	Direct Noise Computation
DNS	Direct Numerical Simulation

FDM	Finite Differences Method
FGM	Flamelet Generated Manifold
FVM	Finite Volume Method
LEE	Linearized Euler Equations
LES	Large Eddy Simulation
LLF	Local Lax-Friedrichs
LNSE	Linearized Navier-Stokes Equations
LODI	Local One-Dimensional Inviscid
MMS	Method of Manufactured Solution
PDE	Partial Differential Equation
PDF	Probability Density Function
PIV	Particle Image Velocimetry
PPDF	Presumed Probability Density Function
PVC	Precessing Vortex Core
RANS	Reynolds Averaged Navier-Stokes
RK4	Fourth Order Runge-Kutta



1 Introduction

Within this work, a hybrid computational aeroacoustics method is devised, implemented and applied to two enclosed, reactive configurations. It comprises a finite volume based flow solver, a discontinuous Galerkin based acoustics tool and a coupling layer, which bridges the different numerical schemes and physical phenomena. In addition to traditional aeroacoustic problems, the method is applicable to enclosed configurations with complex geometries, while maintaining the favorable computational efficiency of common hybrid methods. Its key components are the newly developed acoustics solver and the corresponding coupling layer.

In the following, the motivation for the developed method is laid out, followed by an overview of the current state of research. The chapter concludes with a specification of the aims of this work and an outline of its structure.

1.1 Motivation

According to the 2017 Industry Forecast of the IATA¹, commercial passenger air traffic² saw a steady growth of 5.2% to 7.4% between 2011 and 2016 [56]. The IATA 20 Forecast [55] estimates that passenger air traffic will nearly double until 2036. The increasing amount of air traffic however, entails severe ecological challenges. Without exception, all currently operated commercial passenger aircraft are propelled by the combustion of fuel and hence emit CO₂, NO_x and noise. To counteract the environmental and health damages these emissions bring about, the aircraft manufacturers agreed to implement the SRIA³ agenda, which specifies a reduction of CO₂, NO_x and noise emissions by 75%, 90% and 65%, respectively until 2050 [1]. These ambitious goals, in particular the NO_x reduction, can only be met by the comprehensive migration towards lean premixed combustion based aero engine designs [28].

Compared to conventional rich-quench-lean setups, these next generation combustion systems are more prone to thermoacoustic instabilities caused by combustion noise [28, 81]. Combustion noise originates from the unsteady heat release

¹ IATA: International Air Transport Association

² In terms of total *Revenue Passenger Kilometers* (RPK), i.e. the number of passengers aboard a vehicle times the traveled distance.

³ SRIA: Strategic Research and Innovation Agenda

of a fluctuating flame. When reflected, the acoustic waves can instigate these fluctuations, causing the two phenomena to amplify each other. This constructive interference results in excessive sound pressure levels and flame deflection, which can ultimately lead to the destruction of the combustor [28, 17]. For this reason, improved methods for the prediction and investigation of combustion noise and thermoacoustic instabilities are crucial for the implementation of the SRIA goals.

In this regard, the numerical simulation of combustion noise problems by means of *Computational Aeroacoustics* (CAA) is an economical alternative to experiments. Compared to the field of *Computational Fluid Dynamics* (CFD), CAA simulations involve a much wider range of physical scales [25, 128, 138] while at the same time requiring a higher numerical accuracy. This combination considerably increases the computational cost of *Direct Noise Computation* (DNC) simulations [25, 128, 138]. As a consequence, hybrid CAA methods were developed, which are based on the notion of using two separate numerical tools, that provide optimal computational efficiency and numerical accuracy for their respective sub problem.

Historically, CAA has been focused on external aeroacoustics, where the sound emission on the environment was investigated [139, 138]. However, combustion noise differs significantly from this assumption, since sound generation and propagation are confined to coinciding, enclosed domains. Traditional hybrid CAA methods are based on domain decomposition and are hence not applicable to combustion noise problems. Moreover, the corresponding CAA solvers fail to reliably account for the complex geometries of technical combustion systems, due to their limitation to smooth, structured computational meshes. Consequently, novel hybrid CAA methods and CAA solvers are required, that qualify for combustion noise simulations in industrial environments.

1.2 State of Research

The following section aims to classify the current method with regard to existing approaches. To this end, research activities in the field of hybrid CAA methods are summarized, starting from CAA in general and narrowing down from combustion noise applications to hybrid CAA methods, with the focus on the CFD-CAA coupling schemes.

Computational Aeroacoustics

The foundation of aeroacoustics was laid by Sir James Lighthill in the 1950s by pioneering his *acoustic analogy* [83, 84]. Sparked by the immense noise generation of jet engines, which saw an increasing adoption in commercial aircraft designs, the main subject of research was jet noise, airframe, propeller and combustion noise

[129, 139, 138, 28]. Due to the growing availability of computational power in the 1990s, the field of aeroacoustics saw a transition towards numerical methods, which allowed the investigation of more complex setups and phenomena. This novel discipline, referred to as Computational Aeroacoustics, established the ongoing "second golden age of aeroacoustics" [79]. Colonius and Lele [25] classify the various CAA methods into two categories, DNC simulations, that treat flow and acoustic fields at once and *hybrid CAA* methods, where both fields are computed separately. By accounting for all relevant phenomena in a single simulation, the DNC can provide the most accurate results. Such simulations however, entail significant computational costs, as they need to resolve much smaller time and larger length scales than in most CFD applications [25, 128, 138]. At the same time, CAA problems require very long integration times and distances in order to account for low frequencies and far-field propagation. This calls for more rigorous requirements regarding the numerical accuracy of the employed discretization schemes [25, 128, 138], which further increases the computational effort. DNC simulations are therefore mostly used to study individual phenomena or to provide reference solutions [25, 138]. Compared to DNC, hybrid CAA methods can significantly reduce the computational effort by capturing the acoustics in a separate, dedicated simulation that augments the flow simulation. In such a setup, both simulations can operate at significantly lower computational cost, since their temporal and spatial resolutions, their sets of governing equations and their numerical schemes can be optimized for the respective problems. Consequently, a wide range of hybrid setups for various applications is currently used [125].

CAA for Combustion Noise

In external aeroacoustics, hybrid methods are typically based on a domain decomposition, where the regions of noise generation and acoustic wave propagation are treated separately. When studying combustion noise however, enclosed configurations are common and a decomposition is not feasible, since both domains coincide. Accordingly, DNC simulations have been more common, covering simple laboratory scale combustors [92], complex gas turbine combustors [53, 114, 43, 15] and complete, annular combustors [38, 87]. However, these simulations entail computational costs of several million CPU hours, and even on large high performance computers take months to complete. For this reason, hybrid methods were developed, that are based on a decomposition by physical phenomena [48], instead of the computational domains. In such hybrid simulations, the flow field is split from the acoustic field and accounted for by incompressible or low Mach number governing equations. The resulting noise sources and the temporal mean flow field are then used as input for the acoustics simulation.

Commonly used hybrid CAA methods are based on one-dimensional, analytical approaches [28] such as network models [86, 47, 135]. These provide limited accuracy on the one hand, but require very few computational time on the other hand. Consequently, they can easily be repeated for e.g. testing different design parameters. Other methods, which take more of the combustor's geometric features into account, can deliver more reliable predictions. They either operate in frequency [49, 45] or time domain. In particular in time-domain, hybrid CAA tools were successfully applied to academic, open flames [57, 41], simple [36, 68, 61, 67] and more complex, enclosed configurations [31].

Hybrid CAA in Time Domain

In the context of hybrid CAA with conforming domains, specialized CAA governing equations, such as the *Linearized Euler Equations* (LEE) are employed, which describe a variation around a reference flow state. In addition to the desired acoustic modes, the LEE account for entropy and vortical modes, which are prone to instabilities and hence require special treatment [9, 111]. Due to this limitation, alternative governing equations were proposed [126, 120, 34, 119, 98]. In particular the *Acoustic Perturbation Equations* (APE) [33, 34] have seen wide adoption, due to their unconditional stability. For combustion noise applications, modified formulations, such as the APE-RF (APE for Reacting Flows) [12, 13, 11] or the revised APE [39, 41, 40] are available.

In most applications, the spatial discretization of the CAA governing equations is achieved by means of the *Finite Differences Method* (FDM) [130, 78], for which detailed reviews are given in [72, 128]. Within the *Finite Volume Method* (FVM), which is dominant in CFD applications the implementation of high order methods is difficult. Besides a few exceptions [137, 99], it is hence rarely used in CAA. The most prominent limitation of high order FDM schemes is their inability to account for non-trivial geometries due to their requirement of very smooth, (block-) structured numerical meshes. A class of high order methods that does not suffer from this restraint, are the *Discontinuous Galerkin* (DG) [24] schemes. They are based on an element-wise, spectral discretization by means of local polynomials, which are coupled by interface fluxes, similar to the FVM method. This approach allows for arbitrary convergence orders on unstructured meshes at excellent parallel performance. Its accuracy was demonstrated e.g. in [2, 52, 51, 90, 95]. In CAA, DG methods based on nodal expansion bases, also referred to as spectral elements [107], have been successfully applied to two- [63, 7, 76] and three-dimensional [8, 23, 113] configurations. Due to the complexity of the DG method however, available tools have been limited to academic applications, where flexibility, robustness and performance are of subsidiary importance.

CFD-CAA Coupling

A central component of hybrid CAA methods is the coupling between the CFD and the CAA solvers. For most applications, a *uni-directional coupling*, where only data is transferred from the CFD to the CAA is sufficient. A common implementation is to extract the flow fields and noise sources from the CFD, write them to disk and load the corresponding files into the CAA. In combustion noise simulations, this approach entails a significant performance overhead and requires excessive storage capacities due to temporal variations related to the highly transient flame movements. A run-time coupling, where both solvers run in parallel and exchange data in memory does not suffer from this limitation. Moreover, this is a requirement for *bi-directional coupling*, which is imperative for the correct representation of interactions between combustion and acoustics, e.g. in thermoacoustic instabilities. A uni-directional, run-time coupled hybrid CAA was first applied to combustion noise by Flemming et al. [36]. Other works [61, 68, 67] extended this approach and introduced bi-directional coupling and alternative governing equations, but still relied on FDM, limiting its application to basic, academic configurations. Moreover, the use of simple, radial basis function based CFD-CAA interpolation [121] required the CAA to maintain a similar spatial resolution as the CFD, canceling an important aspect of the computational efficiency of hybrid CAA methods.

In order to allow for coarser spatial CAA resolutions, the presented implementation features a novel interpolation technique, based on direct sampling at the quadrature points of the CAA. Previous high fidelity CFD-CAA interpolation schemes have been focused on finite difference methods [131, 122], on domain decomposition [73, 77], or on setups with similar CFD and CAA length scales [77, 117, 118]. Cunha and Redonnet [27] investigated spatial interpolation for hybrid CAA and determined similar sources of errors for finite differences methods, as identified for FVM-DG interpolations in the current work. In a subsequent study [26], the authors propose a mitigation that is related to the current implementation, as it also involves a spatial low-pass filter. A similar approach is pursued in [46] for FVM-DG interpolation, which, however, includes several additional steps that require further computational resources.

1.3 Aims and Scope of this Work

Based on the preceding summary of current research, a lack of hybrid CAA methods, that maintain their computational efficiency and stability, when applied to complex, enclosed configurations can be identified. Consequently, the aim of the current work is the development of such a hybrid CAA method. The goal is pursued by developing a novel acoustics solver, that accounts for three-dimensional, com-

plex geometries of open and enclosed domains with variable density base flows. As in CAA a low discretization error is essential, the solver employs a high order discontinuous Galerkin method. To this end, it is based on the open-source Nektar++ framework [19, 62], which has shown to give excellent stability and performance for large, complex problems [96, 10, 19]. In order to maintain the computational efficiency of the hybrid CAA method in coinciding domains, a coupling scheme is devised and implemented, that bridges the different time and length scales of the flow and acoustic fields. Therein, the transient behavior of reactive flows is accounted for by continuous data exchanges at run-time with minimal overhead. As CFD solver, an existing FVM based tool is used, that has been an integral part of the combustor design process and, apart from the added coupling interface, was not modified. Accordingly, the current work is focused on the novel CAA solver and the corresponding coupling scheme. The major aims of this work are:

- Development of an efficient, stable and flexible CAA solver, that qualifies for combustion noise simulations in complex, enclosed configurations.
- Development of a coupling layer, that facilitates continuous, bi-directional data exchange at run-time and bridges the different scales of acoustics and flow, without limiting the accuracy, stability or efficiency of the solvers.
- Investigation of the method's applicability to laboratory scale combustors, as preliminary stage towards industrial combustion systems.

1.4 Structure of this Work

The work is divided into eight chapters. Following this introduction, the mathematical model inherent to the presented method is established in **chapter 2**. To this end, the low Mach number governing equations of fluid dynamics are reviewed and extended with special treatments for turbulence and combustion. The model is augmented by a matching set of governing equations for the generation and propagation of acoustic waves, that can be solved separately by the CAA solver. Subsequently, the temporal and spatial discretizations, as well as the implemented solution algorithms are laid out for the CAA and CFD in **chapters 3** and **4**, respectively. In light of the work's focus, the description of the CAA solver is more detailed. It features different strategies for Riemann solvers and boundary conditions, as well as a verification of the current implementation. In **chapter 5**, the coupling scheme is developed based on an identification of the different error sources involved in the spatial interpolation.

The developed methods and implementations are validated by means of two test cases, with both investigations supported by reference data, available from numerical simulations and experiments. The setup considered in **chapter 6** comprises a generic half-dump combustor, with relatively simple geometry and flow field, that allows for a straightforward assessment of the coupling layer. Accordingly, special emphasis is put on the exploration of different coupling parameters, including the spatial filtering and sampling resolutions. Building on this validation, the thermoacoustic properties of a swirl stabilized burner are characterized in **chapter 7** for two operating points. This configuration features a more complex geometry, flow field and flame behavior and thereby promotes the evaluation of the developed method and the CAA solver in particular. To this end, an in-depth analysis of the prevalent flow features, flame behavior and dominant acoustic modes is performed, as well as an exemplary investigation of the computational efficiency of the coupling layer. In **chapter 8**, the main findings of the preceding chapters are summarized and possible starting points for future works are highlighted.



2 Mathematical Model

This chapter gives an overview of the mathematical modeling of the phenomena considered throughout this work. Aim of the description is to establish a consistent nomenclature and to outline the formulations and simplifications, used to arrive at the final sets of governing equations. In the following, all expressions are based on the three-dimensional, Cartesian coordinate system with unit base vectors \mathbf{e}_1 , \mathbf{e}_2 and \mathbf{e}_3 . Scalars are indicated by a normal font, e.g. q . For higher order tensors, a bold font is used, e.g. $\mathbf{q} = q_1\mathbf{e}_1 + q_2\mathbf{e}_2 + q_3\mathbf{e}_3$. Besides this symbolic notation, the coordinate notation is used, e.g. q_i , where Einstein's index summation convention is implied. With this notation, the location vector is given as $\mathbf{x} = x_i\mathbf{e}_i$ or x_i and the time as t .

2.1 Governing Equations for Fluid Dynamics

In the following section, the basic governing equations of fluid dynamics are summarized. If not stated otherwise, the descriptions are based on Poinot and Veynante [109], where derivations and more detailed explanations can be found.

2.1.1 Conservation of Mass

Mass can neither be created nor destroyed. Consequently, a temporal change of mass inside a volume has to be compensated by the sum of mass fluxes through the volume's surface. This relation is formalized in the equation of mass conservation

$$\frac{\partial \varrho}{\partial t} + \frac{\partial \varrho u_i}{\partial x_i} = 0, \quad (2.1)$$

with the density ϱ and the velocity $u_i = \mathbf{u}$.

2.1.2 Conservation of Momentum

An other quantity, for which conservation must be ensured is the momentum ϱu_i . To this end, its temporal change inside a volume must be in equilibrium with the momentum transported across the volume's surface and the forces acting on it:

$$\frac{\partial \varrho u_i}{\partial t} + \frac{\partial \varrho u_i u_j}{\partial x_j} = -\frac{\partial p}{\partial x_i} + \frac{\partial \tau_{ij}}{\partial x_j} + \varrho g_i. \quad (2.2)$$

Here, the pressure p , the stress tensor τ_{ij} and the body forces g_i were introduced. Throughout this work, body forces are neglected, so $g_i = 0$. Moreover, all fluids are assumed to be Newtonian fluids, so the stress tensor is defined by the pressure p , the dynamic viscosity μ and the velocity gradients through the corresponding material law:

$$\tau_{ij} = \mu \left(\frac{\partial u_i}{\partial x_j} + \frac{\partial u_j}{\partial x_i} \right) - \frac{2}{3} \mu \frac{\partial u_m}{\partial x_m} \delta_{ij}. \quad (2.3)$$

The momentum equation for Newtonian fluids with neglected body forces then reads:

$$\frac{\partial \varrho u_i}{\partial t} + \frac{\partial \varrho u_i u_j}{\partial x_j} = -\frac{\partial p}{\partial x_i} + \frac{\partial}{\partial x_j} \left(\mu \left(\frac{\partial u_i}{\partial x_j} + \frac{\partial u_j}{\partial x_i} \right) - \frac{2}{3} \mu \frac{\partial u_m}{\partial x_m} \delta_{ij} \right). \quad (2.4)$$

2.1.3 Species Transport

Reactive flows are typically a mixture of N_s different species, occurring in varying concentrations. The composition of a fluid is described by the mass fraction Y_k of the species k

$$Y_k := \frac{m_k}{m}, \quad (2.5)$$

which can be obtained from the corresponding transport equations

$$\frac{\partial \varrho Y_k}{\partial t} + \frac{\partial \varrho u_i Y_k}{\partial x_i} = \frac{\partial \varrho V_{ki} Y_k}{\partial x_i} + \dot{\omega}_k, \quad (2.6)$$

with the chemical source term $\dot{\omega}_k$ and the diffusion velocity V_{ki} for each species k . The latter is approximated by Fick's law from the species mass fraction gradient and its diffusion coefficient \mathcal{D}_k

$$\varrho V_{ki} Y_k = -\varrho \mathcal{D}_k \frac{\partial Y_k}{\partial x_i}. \quad (2.7)$$

The diffusion coefficient can in turn be expressed as Schmidt number

$$Sc_k := \frac{\mu}{\varrho \mathcal{D}_k}, \quad (2.8)$$

which specifies the ratio between diffusive momentum and diffusive species transport. By definition, the sum of species mass fractions, chemical source terms and species diffusion are given as

$$\sum_{k=1}^{N_S} Y_k = 1, \quad \sum_{k=1}^{N_S} \dot{\omega}_k = 0, \quad \sum_{k=1}^{N_S} Y_k V_{ki} = 0. \quad (2.9)$$

With Fick's law and the definition of the Schmidt number, the species transport equation (2.6) reads

$$\frac{\partial \varrho Y_k}{\partial t} + \frac{\partial \varrho u_i Y_k}{\partial x_i} = \frac{\partial}{\partial x_i} \left(\frac{\mu}{Sc_k} \frac{\partial Y_k}{\partial x_i} \right) + \dot{\omega}_k. \quad (2.10)$$

2.1.4 Conservation of Energy

The first law of thermodynamics states that the total energy of an isolated system is constant. Within this work, the specific enthalpy h is used as state variable. It results from the mass weighted enthalpies of each species h_k with

$$h = \sum_{k=1}^{N_S} Y_k h_k \quad \text{and} \quad h_k = \Delta h_{f,k}^{\text{ref}} + \int_{T_{\text{ref}}}^T c_{p,k} dT. \quad (2.11)$$

They consist of a chemical part, represented by the enthalpy of formation $\Delta h_{f,k}^{\text{ref}}$ at temperature T_{ref} and a temperature dependent part, given by the integration of the specific heat capacity at constant pressure c_p over the temperature T . The full enthalpy conservation equation reads

$$\frac{\partial \varrho h}{\partial t} + \frac{\partial \varrho u_i h}{\partial x_i} = \frac{Dp}{Dt} + \tau_{ij} \frac{\partial u_i}{\partial x_j} - \frac{\partial q_i}{\partial x_i} + \dot{\omega}_h + \varrho \sum_{k=1}^{N_S} Y_k g_{ki} V_{ki}. \quad (2.12)$$

In Eq. (2.12), the last two terms represent the input or removal of enthalpy by external sources and the enthalpy change due to body forces, respectively. Both phenomena are not considered in this work and the corresponding terms vanish.

The third term on the right hand side denotes the enthalpy flux due to species diffusion and heat conduction

$$q_i = -\kappa \frac{\partial T}{\partial x_i} + \varrho \sum_{k=1}^{N_s} h_k Y_k V_{ki} . \quad (2.13)$$

The ratio of these two mechanisms is given by the dimensionless Lewis number for the species k :

$$Le_k := \frac{\kappa}{c_p \mathcal{D}_k \varrho} . \quad (2.14)$$

Assuming this ratio to be unity for all species, i.e. $Le_k = 1$, the enthalpy flux q_i simplifies to

$$q_i = -\frac{\kappa}{c_p} \frac{\partial h}{\partial x_i} . \quad (2.15)$$

For unity Lewis number and neither external sources nor body forces, the full enthalpy equation (2.12) reduces to:

$$\frac{\partial \varrho h}{\partial t} + \frac{\partial \varrho u_i h}{\partial x_i} = \frac{Dp}{Dt} + \tau_{ij} \frac{\partial u_i}{\partial x_j} + \frac{\partial}{\partial x_i} \left(\frac{\kappa}{c_p} \frac{\partial h}{\partial x_i} \right) . \quad (2.16)$$

2.1.5 Equation of State

The previously described system of governing equations, consisting of Eqs. (2.1), (2.4), (2.10) and (2.16) contains $6 + N_s$ unknowns, ϱ , u_i , Y_k , h and p but only $5 + N_s$ equations. One additional relation, the thermal equation of state is required to close the system:

$$p = p(\varrho, T) . \quad (2.17)$$

In this work, only ideal gases are considered, so the above relation can be replaced with

$$p = \varrho R_s T , \quad (2.18)$$

where the specific gas constant of the mixture R_s was introduced. For ideal gases, the isentropic relation with the isentropic exponent γ

$$\frac{p_1}{p_2} = \left(\frac{\varrho_1}{\varrho_2} \right)^\gamma , \quad (2.19)$$

can be used to define the speed of sound as

$$c^2 := \left. \frac{\partial p}{\partial \rho} \right|_{\text{isentropic}} = \gamma \frac{p}{\rho}. \quad (2.20)$$

The ratio of the velocity $\|\mathbf{u}\|$ and the speed of sound is the Mach number

$$Ma := \frac{\|\mathbf{u}\|}{c}. \quad (2.21)$$

2.1.6 The Low Mach Number Approximation

By decomposing the pressure p into a hydrodynamic p^{dyn} and a static component p^{stat} :

$$p = p^{\text{stat}} + p^{\text{dyn}}, \quad (2.22)$$

their ratios

$$\frac{p^{\text{dyn}}}{p^{\text{stat}}} = \frac{1}{2} \gamma Ma^2 \quad (2.23)$$

can be used to expand the dependent variables of the compressible governing equations (2.1, 2.4, 2.10, 2.16) in a power series [100]. For low Mach numbers, the high order terms are small and can be neglected, resulting in the low Mach number flow governing equations¹:

$$\frac{\partial \rho}{\partial t} + \frac{\partial \rho u_i}{\partial x_i} = 0 \quad (2.24a)$$

$$\frac{\partial \rho u_j}{\partial t} + \frac{\partial \rho u_i u_j}{\partial x_i} = -\frac{\partial p^{\text{dyn}}}{\partial x_j} + \frac{\partial}{\partial x_i} \left(\mu \left(\frac{\partial u_i}{\partial x_j} + \frac{\partial u_j}{\partial x_i} \right) - \frac{2}{3} \mu \frac{\partial u_m}{\partial x_m} \delta_{ij} \right) \quad (2.24b)$$

$$\frac{\partial \rho Y_k}{\partial t} + \frac{\partial \rho u_i Y_k}{\partial x_i} = \frac{\partial}{\partial x_i} \left(\frac{\mu}{Sc_k} \frac{\partial Y_k}{\partial x_i} \right) + \dot{\omega}_k \quad (2.24c)$$

$$\frac{\partial \rho h}{\partial t} + \frac{\partial \rho u_i h}{\partial x_i} = \frac{\partial}{\partial x_i} \left(\frac{\kappa}{c_p} \frac{\partial h}{\partial x_i} \right). \quad (2.24d)$$

¹ Unlike the incompressible governing equations ($\lim_{Ma \rightarrow 0}$), the low Mach number equations (2.24) support variable density.

Notable differences are the absence of the first two terms on the right hand side of the enthalpy equation and the use of the dynamic pressure p^{dyn} in the momentum equation. The terms which denote enthalpy change due to pressure variations and viscous heating are negligible for low Mach number flames and were neglected. The hydrodynamic pressure occurring exclusively in the momentum equation has more severe effects. There is no relation between p^{dyn} and the density, so density perturbations do not cause pressure and velocity perturbations anymore, prohibiting the transport of pressure or acoustic waves. This also renders the continuity equation incapable of closing the momentum equation. Instead, the continuity (2.1) and momentum equations (2.4) are combined, to obtain a Poisson equation for the pressure [35]:

$$\frac{\partial^2 p}{\partial x_i \partial x_i} = -\frac{\partial}{\partial x_i} \left[\frac{\partial}{\partial x_j} \left(\rho u_i u_j - \mu \left(\frac{\partial u_i}{\partial x_j} + \frac{\partial u_j}{\partial x_i} \right) + \frac{2}{3} \mu \frac{\partial u_m}{\partial x_m} \delta_{ij} \right) \right] + \frac{\partial^2 \rho}{\partial t^2}. \quad (2.25)$$

This equation is elliptic, which means that with the low Mach number approximation, pressure perturbations are transported at infinite velocity, unlike the predominantly hyperbolic compressible Navier-Stokes equations, where they travel at $u_i \pm c$. Consequently, propagation of acoustic waves cannot be correctly modeled by the low Mach number flow governing equations (2.24). In addition, only the gradient of the dynamic pressure is available from Eq. (2.24), not its absolute value. To avoid excessively small or large p^{dyn} , an arbitrary value at an arbitrary point inside the domain must be prescribed.

2.2 Turbulent Flows

Depending on the magnitudes of inertial and viscous forces, a small perturbation of a flow field can be either instigated or dampened. The ratio of these forces is given by the Reynolds number

$$Re := \frac{u_c l_c}{\nu}, \quad (2.26)$$

where u_c is a characteristic flow velocity, l_c a characteristic length scale and ν the kinematic viscosity $\nu = \mu/\rho$. The inertial forces in the numerator of the Reynolds number cause the perturbation to be instigated, while the viscous forces in the denominator cause them to be dampened. Consequently, for small Reynolds numbers, a flow field tends to be characterized by parallel motions and is accordingly referred to as laminar. For high Re , it is strongly chaotic and referred to as turbulent. Both regimes can be represented by the same set of governing equations

(2.24) and transition from one regime to another is possible. Turbulence is by definition stochastic, unsteady and necessarily three-dimensional [110]. The turbulent motions lead to advective transport in flow normal direction and therefore have the same effect as an increased diffusion. Due to its quasi-random character, an instantaneous, turbulent flow field is difficult to interpret and analyze. A simplified description is the decomposition of an instantaneous quantity q into its temporal mean $\langle q \rangle$ and a fluctuation

$$q' := q - \langle q \rangle . \quad (2.27)$$

Therein, the temporal mean is computed as

$$\langle q \rangle := \frac{1}{\Delta t} \int_{t_0}^{t_0 + \Delta t} q(t) dt , \quad (2.28)$$

where Δt marks a time interval, which has to be sufficiently large. The mean value of the fluctuation q' is by definition zero, i.e. $\langle q' \rangle = 0$. Thus, fluctuations are characterized by the variance of q , $\langle q'^2 \rangle$. Accordingly, the standard deviation, or root mean square, is given in terms of the variance as:

$$q_{\text{rms}} := \sqrt{\langle q'^2 \rangle} . \quad (2.29)$$

In analogy to the Reynolds number above, a turbulent Reynolds number Re_t can be defined from the characteristic scales of the turbulence:

$$Re_t := \frac{u_{\text{rms}} l_1}{\nu} , \quad (2.30)$$

where the characteristic length scale l_1 was introduced [110].

2.2.1 Turbulent Scales

The chaotic motions in turbulent flows may be viewed as hierarchy of vortices, so called *eddies*, that span a wide range of length, time and velocity scales. The largest structures are fed by energy from the mean flow and depend on the geometry of the domain and the direction of the flow. Hence, their size and velocity are determined by the characteristic length and velocity scales of the flow, l_c and u_c , respectively. The energy contained in the turbulent structures is the *turbulent kinetic energy*:

$$\mathcal{K} := \frac{1}{2} \langle u'_i u'_i \rangle \quad (2.31)$$

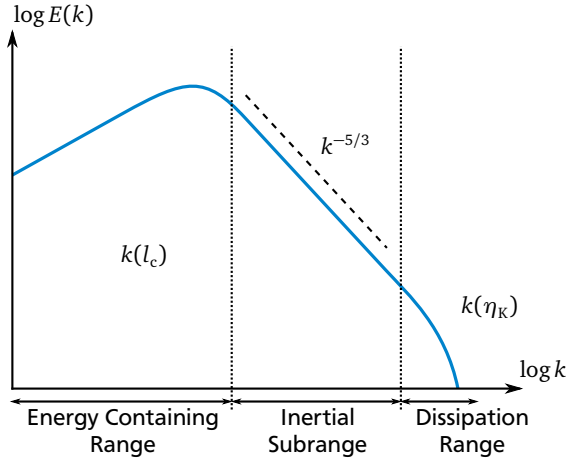


Figure 2.1: Spectrum of the turbulent kinetic energy over progressively smaller eddies with wave number $k = 2\pi/l$ and energy $E(k)$ for homogeneous, isotropic turbulence.

The Reynolds number of the large eddies is too high to dissipate energy due to viscous forces. Instead, the energy is passed on to progressively smaller eddies until the viscous forces prevail. This mechanism is referred to as the energy cascade of turbulent flows. The energy spectrum in Fig. 2.1 illustrates the distribution of \mathcal{E} over eddies with the wave number $k = 2\pi/l$. The major part of the turbulent kinetic energy is contained in the largest structures of the energy containing range (l_c), from where it is passed on to the inertial subrange and finally to the dissipation range. The smallest structures of the cascade in the dissipation range are characterized by the viscosity and the rate at which turbulent kinetic energy is dissipated. Their length scale, which marks the smallest eddies is the Kolmogorov length scale η_K . A relation between the largest (l_c) and smallest (η_K) scales of a flow is given as [110]:

$$\frac{\eta_K}{l_c} = Re_t^{-3/4}. \quad (2.32)$$

2.2.2 Turbulence Modeling

The system of governing equations (2.24) is closed and can therefore be solved by e.g. using one of the numerical methods presented in chapter 4. With this approach, called *Direct Numerical Simulation* (DNS), even the smallest turbulent scales, the Kolmogorov scales, need to be resolved by the spatial discretization method. The number of required control volumes N_{CV} can be estimated for isotropic, homogeneous turbulence and a finite volume discretization as

$$N_{CV} \propto \eta_K^{-3} \propto Re_t^{9/4}. \quad (2.33)$$

The computational cost of a CFD simulation grows with the number of degrees of freedom that must be accounted for to obtain the flow field. This amounts to the product of the number of control volumes and the number of time steps required to account for the flow's temporal evolution. The latter is again inversely proportional to the smallest length scales, so the total number of degrees of freedom N_{DOF} is estimated as:

$$N_{DOF} \propto \eta_K^{-1} N_{CV} \propto Re_t^3. \quad (2.34)$$

This illustrates how even slight increases of the Reynolds number can easily cause the computational effort required to simulate even simple flow problems, to exceed the available resources. Given that for most technical applications, high Reynolds numbers and large, complex geometries are the norm, direct numerical simulations are not a viable option for efficient noise simulations.

2.2.2.1 RANS Models

A more economical approach is the *Reynolds Averaged Navier-Stokes* (RANS) description, where the Reynolds averaging (2.28) is applied to the governing equations (2.24) to obtain a mean flow field. In the RANS equations, the expensive resolution of the turbulent scales is avoided entirely. However, due to the averaging, the Reynolds stresses $\langle u'_i u'_j \rangle$ arise from the advective term, which need to be modeled in order to close the equation system again. Various models for this purpose, with different fields of application, advantages and shortcomings have been proposed and are still being developed [110]. One category is the Reynolds stress models, where each component of the Reynolds stress tensor is calculated independently. This introduces six² additional governing equations that need to be

² The Reynolds stress tensor $\langle u'_i u'_j \rangle$ has nine components but is symmetric, so only six components need to be modeled.

solved and therefore increases the computational cost accordingly. An other, more economical category of RANS models are the eddy viscosity based models, which are based on the Boussinesq hypothesis [110]. This approximation allows for the expression of the nine Reynolds stresses in terms of the mean flow gradients and a single quantity, the turbulent viscosity. The latter needs modeling in turn and a vast number of models with varying fidelity and computational cost are available.

While by design, the RANS equations describe a temporal mean, they allow for modeling of transient processes, that do not exhibit the stochastic character of turbulence. They can be caused by e.g. varying boundary conditions or transient, non-turbulent flow phenomena like vortex shedding over a stalled airfoil. Despite not being turbulence in the phenomenological sense, these phenomena contribute to the low wave number regime of energy spectrum in Fig. 2.1. The actual turbulent motions however, are not resolved by any of the RANS models.

Thanks to their low computational overhead and numerical stability, eddy viscosity based RANS models are used for the majority of the simulations conducted today. They facilitate the solution of flow problems with complex and large computational domains, but interpreting their results requires comprehensive knowledge of their capabilities and limitations as well as experience with the specific flow configuration. Nevertheless, a well tested and tuned RANS model can provide profound insight into familiar flow problems, e.g. when used in parametric studies, frequently conducted in design processes. For reacting flows however, a high fidelity representation of the turbulent motions is crucial. Consequently, RANS models do not qualify for the problems investigated in this work and their description will not be further elaborated.

2.2.2.2 Large Eddy Simulation

The concept of the *Large Eddy Simulation* (LES) is to only resolve the large turbulent motions, while the smallest scales are modeled. This approach marks a middle ground between the expensive but accurate DNS and the economical RANS models. By introducing a spatial filter

$$\bar{q}(\mathbf{x}, t) := \int q(\mathbf{x} - \mathbf{r}, t) \mathcal{G}(\mathbf{r}, \mathbf{x}) \, d\mathbf{r} , \quad (2.35)$$

large \bar{q} and small scale structures q'' are separated according to:

$$q'' := q - \bar{q} . \quad (2.36)$$

Different choices for the filter function \mathcal{G} with different properties in spectral domain are possible. According to the Pope-Criterion [110], the choice of \mathcal{G} should

ensure that at least 80 % of the turbulent spectrum is resolved. In the current implementation, the filter function is not set explicitly but instead prescribed by the mesh of the finite volume discretization. Its control volume size is chosen to be larger than the smallest turbulent scales, allowing the mesh to act as an implicit filter. In terms of a filter function \mathcal{G} , this corresponds to a top-hat filter with the mesh spacing h as filter width. Direct application of the spatial filter (2.35) to the governing equations would give rise to additional terms, containing correlations with the density, which would require additional modeling. Instead, the density based Favre averaging [109] is introduced:

$$\tilde{q} := \frac{\overline{\varrho q}}{\overline{\varrho}}. \quad (2.37)$$

Similar to the spatial filter (2.35), this decomposes the flow field into a resolved part \tilde{q} and an unresolved subgrid scale q^{sgs} :

$$q = \tilde{q} + q^{\text{sgs}}. \quad (2.38)$$

The Favre-averaged, filtered governing equations for low Mach number flows (2.24) read:

$$\frac{\partial \overline{\varrho}}{\partial t} + \frac{\partial \overline{\varrho} \tilde{u}_i}{\partial x_i} = 0 \quad (2.39a)$$

$$\frac{\partial \overline{\varrho} \tilde{u}_j}{\partial t} + \frac{\partial \overline{\varrho} \tilde{u}_i \tilde{u}_j}{\partial x_i} = -\frac{\partial \overline{p^{\text{dyn}}}}{\partial x_j} + \frac{\partial}{\partial x_i} \left(\overline{\mu} \left(\frac{\partial \tilde{u}_i}{\partial x_j} + \frac{\partial \tilde{u}_j}{\partial x_i} \right) - \frac{2}{3} \overline{\mu} \frac{\partial \tilde{u}_m}{\partial x_m} \delta_{ij} - \overline{\varrho} \tau_{ij}^{\text{sgs},u} \right) \quad (2.39b)$$

$$\frac{\partial \overline{\varrho} \tilde{Y}_k}{\partial t} + \frac{\partial \overline{\varrho} \tilde{u}_i \tilde{Y}_k}{\partial x_i} = \frac{\partial}{\partial x_i} \left(\frac{\overline{\mu}}{Sc_k} \frac{\partial \tilde{Y}_k}{\partial x_i} - \overline{\varrho} \tau_k^{\text{sgs},Y} \right) + \overline{\omega}_k \quad (2.39c)$$

$$\frac{\partial \overline{\varrho} \tilde{h}}{\partial t} + \frac{\partial \overline{\varrho} \tilde{u}_i \tilde{h}}{\partial x_i} = \frac{\partial}{\partial x_i} \left(\frac{\overline{\kappa}}{\overline{c}_p} \frac{\partial \tilde{h}}{\partial x_i} - \overline{\varrho} \tau^{\text{sgs},h} \right), \quad (2.39d)$$

where the subgrid parts

$$\tau_{ij}^{\text{sgs},u} := \overline{u_i u_j} - \tilde{u}_i \tilde{u}_j \quad (2.40a)$$

$$\tau_k^{\text{sgs},Y} := \overline{u_i Y_k} - \tilde{u}_i \tilde{Y}_k \quad (2.40b)$$

$$\tau^{\text{sgs},h} := \overline{u_i h} - \tilde{u}_i \tilde{h} \quad (2.40c)$$

arise from the advective term. These new terms are unknown and must be modeled in order to close the system of equations.

As laid out in section 2.2, turbulence has a similar effect as diffusion due to the flow-normal velocity components it introduces. This is reflected by Eqs. (2.39), where the subgrid parts were moved into the diffusive terms due to their similar structure. Consequently, the eddy viscosity approximation inherent to the RANS turbulence models, is a suitable modeling approach for the anisotropic part of the subgrid stress tensor $\tau_{ij}^{sgs,u}$ as well:

$$\tau_{ij}^{sgs,u} - \frac{1}{3}\tau_{mm}^{sgs,u}\delta_{ij} = -2\nu_t \left(\tilde{S}_{ij} - \frac{1}{3}\tilde{S}_{mm}\delta_{ij} \right). \quad (2.41)$$

Here, ν_t denotes the eddy viscosity and \tilde{S}_{ij} the filtered rate of strain:

$$\tilde{S}_{ij} := \frac{1}{2} \left(\frac{\partial \tilde{u}_i}{\partial x_j} + \frac{\partial \tilde{u}_j}{\partial x_i} \right). \quad (2.42)$$

The second term on the left hand side of Eq. (2.41) denotes the isotropic part of the subgrid stress tensor and can be included in a modified pressure

$$\overline{p}^{\text{mod}} := \overline{p}^{\text{dyn}} + \frac{1}{3}\overline{\rho}\tau_{mm}^{sgs,u}. \quad (2.43)$$

While formally similar to the RANS turbulence models, the eddy viscosity based LES models only apply the eddy viscosity approximation to the smallest turbulent scales, instead of the entire spectrum. This increases the simulation's fidelity by reducing its amount of modeling. In addition, the assumption of isotropic turbulence is more appropriate for the small scales, which further adds to the accuracy of the LES technique.

Smagorinsky Model

A simple eddy viscosity based subgrid model is the Smagorinsky model. Based on a dimensional analysis, ν_t is expressed via the filtered rate of strain \tilde{S}_{ij} , the filter width Δh_{filt} and a model constant C_S :

$$\nu_t = (C_S \Delta h_{\text{filt}})^2 \mathcal{S} \quad \text{with} \quad \mathcal{S} := \sqrt{2\tilde{S}_{ij}\tilde{S}_{ij}} \quad \text{and} \quad C_S = \text{constant}. \quad (2.44)$$

One prominent limitations of the model is the constant C_S , which has to be specified based on experience for each setup. The other major restriction is that the eddy viscosity does not tend towards zero when approaching the wall, as physics would dictate.

Germano Procedure

The Germano procedure, or dynamic Smagorinsky model tries to alleviate these drawbacks by replacing the model constant with a temporally and spatially varying, dynamically computed parameter C_G :

$$\nu_t = C_G(\mathbf{x}, t) \Delta h_{\text{filt}}^2 \mathcal{S}. \quad (2.45)$$

The model's general idea is to apply a coarser test filter $\widetilde{\Delta} h_{\text{filt}} > \Delta h_{\text{filt}}$ to the resolved field \widetilde{q} and use the result $\widetilde{\widetilde{q}}$ to dynamically calibrate the parameter C_G . Throughout this work, the test filter is chosen as top-hat filter that contains all neighboring control volumes and is hence implicitly defined by the mesh as well. The unresolved stresses of the test filter then read:

$$\tau_{ij}^{\text{test},u} := \widetilde{\widetilde{u_i u_j}} - \widetilde{\widetilde{u_i}} \widetilde{\widetilde{u_j}} \quad (2.46)$$

and the filtered subgrid stresses of the first filter are:

$$\overline{\tau_{ij}^{\text{sgs},u}} = \overline{\widetilde{u_i u_j}} - \overline{\widetilde{u_i}} \overline{\widetilde{u_j}}. \quad (2.47)$$

The difference between these two stresses is the Germano identity

$$L_{ij} := \tau_{ij}^{\text{test},u} - \overline{\tau_{ij}^{\text{sgs},u}} = \widetilde{\widetilde{u_i u_j}} - \widetilde{\widetilde{u_i}} \widetilde{\widetilde{u_j}}, \quad (2.48)$$

which can be obtained from the resolved field. With the assumption that a single Germano parameter $C_G(\mathbf{x}, t)$ applies to both filters equally, the eddy viscosity approximation gives:

$$\tau_{ij}^{\text{sgs},u} - \frac{1}{3} \tau_{mm}^{\text{sgs},u} \delta_{ij} = -2 C_G \Delta h_{\text{filt}}^2 \mathcal{S} \left(\widetilde{S}_{ij} - \frac{1}{3} \widetilde{S}_{mm} \delta_{ij} \right) =: -2 C_G m_{ij}^{\text{sgs}} \quad (2.49)$$

$$\tau_{ij}^{\text{test},u} - \frac{1}{3} \tau_{mm}^{\text{test},u} \delta_{ij} = -2 C_G \widetilde{\Delta} h_{\text{filt}}^2 \widetilde{\mathcal{S}} \left(\widetilde{\widetilde{S}}_{ij} - \frac{1}{3} \widetilde{\widetilde{S}}_{mm} \delta_{ij} \right) =: -2 C_G m_{ij}^{\text{test}}. \quad (2.50)$$

Using the Germano identity (2.48), this leads to the system of equations

$$L_{ij} - \frac{1}{3} L_{mm} \delta_{ij} = 2 C_G M_{ij} \quad \text{with} \quad M_{ij} := \overline{m_{ij}^{\text{sgs}}} - m_{ij}^{\text{test}}. \quad (2.51)$$

Since C_G is a scalar, this linear equation system is over-determined and hence poses an optimization problem. Lilly [85] proposed using a least squares procedure to finally obtain the Germano parameter as

$$C_G = \frac{M_{ij} L_{ij}}{2 M_{ij} M_{ij}}. \quad (2.52)$$

The described Germano procedure can yield negative values for C_G . This is caused by backscatter, i.e. when energy is fed from the small scale turbulence to the larger scales. Despite being physically reasonable, the Germano parameter was limited to positive values in the current implementation, consequently disabling backscatter, for the sake of numerical stability.

Scalar Subgrid Terms

Besides the subgrid stress tensor $\tau_{ij}^{sgs,u}$, the unresolved transport of species $\tau_k^{sgs,Y}$ and enthalpy $\tau_k^{sgs,h}$ need to be modeled. To this end, a gradient flux approach is used

$$\tau_k^{sgs,Y} = -\frac{\nu_t}{Sc_{t,k}} \frac{\partial \tilde{Y}_k}{\partial x_j}, \quad (2.53)$$

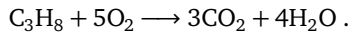
where the turbulent Schmidt number $Sc_{t,k}$ was introduced. Consistent with the treatment of the molecular Schmidt number (2.8), identical turbulent Schmidt numbers of $Sc_{t,k} = Sc_k = Sc = 0.7$ are prescribed for all species. The identical approach is used for the unresolved enthalpy transport with identical turbulent Lewis numbers of unity for all species.

2.3 Reactive Flows

Although not a flow feature, the chemical reactions inherent to the combustion can be modeled within a fluid dynamics simulation. The processes are simplified so that the phenomena relevant for the investigated configurations are sufficiently recovered. To this end, the significantly smaller length and time scales of the chemistry are eliminated from the governing equations, facilitating an efficient treatment within the realm of low Mach number fluid dynamics.

2.3.1 Reaction Kinetics

As soon as the energy available on the molecular level exceeds the activation energy, a mixture of fuel and oxidator reacts. The conversion from educts to products is described by a global reaction equation. A propane C_3H_8 flame, for example, reacts with oxygen O_2 to carbon-dioxide CO_2 and water H_2O , while the nitrogen of the air does not contribute to the process. This global view, which considers only the products and educts of the entire reaction is formalized in a global reaction equation:

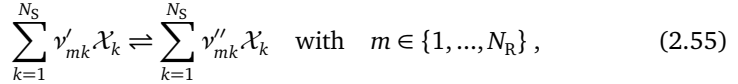


This equation is only valid for a stoichiometric mixture, when the educts are completely converted to products. The composition of the mixture is characterized by the equivalence ratio Φ , which denotes the ratio of the actual fuel-air ratio to the stoichiometric ratio:

$$\Phi = \frac{Y_{fuel}/Y_{air}}{(Y_{fuel}/Y_{air})_{stoich}}. \quad (2.54)$$

Based on this ratio, three conditions can be identified. At $\Phi = 1$, the reaction is stoichiometric, as in the global reaction above. For values greater 1, referred to as rich combustion, the fuel is in excess and cannot be fully consumed. In the opposite, lean case $\Phi < 1$, insufficient fuel is available and the air is not fully consumed.

While useful for e.g determining the equivalence ratio, the global reaction equation does not reflect the actual chemical process. In reality, the molecules of the reactants are broken into smaller molecules, atoms and radicals before they recombine to new species and eventually form the final reaction products. Therefore, a global reaction usually consists of a system of numerous elementary reactions, which have to be considered as well. A system of N_R reactions with N_S species \mathcal{X}_k has the form:



with the stoichiometric coefficients of the reactants ν'_k and products ν''_k . The arrow pointing in both directions indicates the reaction can proceed in both directions, depending on the forward r_{fwd} and backward r_{bwd} reaction rates:

$$r_m = r_{\text{fwd},m} - r_{\text{bwd},m} = k_{\text{fwd},m} \prod_{k=1}^{N_S} c_k^{\nu'_{km}} - k_{\text{bwd},m} \prod_{k=1}^{N_S} c_k^{\nu''_{km}} \quad \text{with } m \in \{1, \dots, N_R\}, \quad (2.56)$$

with the concentrations c_k . The rate coefficients $k_{\text{fwd},m}$ and $k_{\text{bwd},m}$ are approximated by an exponential expression, the Arrhenius law:

$$k_{\text{dir}} = B_{\text{dir}} T^{\alpha_{\text{dir}}} \exp\left(\frac{-E_{\text{dir}}}{R_u T}\right). \quad (2.57)$$

Here, the reaction rate constant B_{dir} describes the number of collisions between reactants per time, E_{dir} denotes the activation energy, α_{dir} a correction factor and R_u the universal gas constant. With the molecular mass \mathcal{M}_k , the source term of the species equation (2.10) follows as:

$$\dot{\omega}_k = \mathcal{M}_k \frac{\partial c_k}{\partial t} = \mathcal{M}_k \sum_{m=1}^{N_R} (\nu''_{km} - \nu'_{km}) r_m \quad \text{with } k \in \{1, \dots, N_S\}. \quad (2.58)$$

2.3.2 Premixed Flames

Depending on the initial state of fuel and oxidizer, combustion is generally classified as either premixed or non-premixed. In non-premixed flames, fuel and oxidizer are initially separate so that the combustion takes place at their interface, where both components mix and eventually reach stoichiometry. In premixed flames, the reactants are already mixed on a molecular level before the reaction occurs. However, in most technical applications, no clear distinction between either of these categories is possible, as both modes can be present simultaneously. In this work, only premixed flames are considered, which are consequently described in more detail.

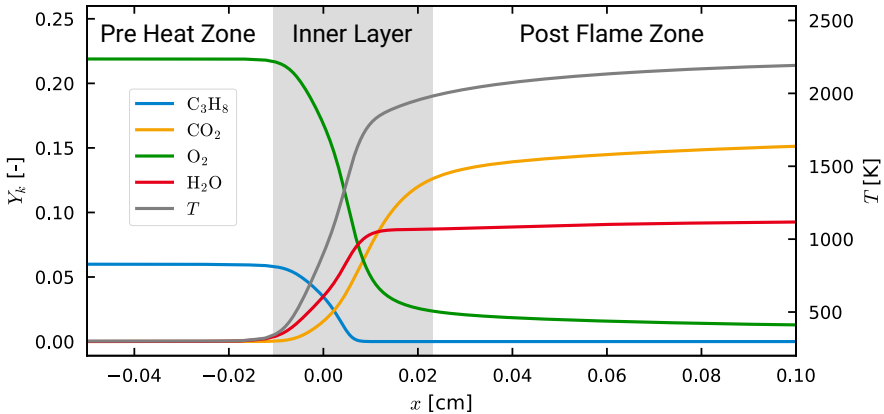


Figure 2.2: Qualitative structure of a premixed propane flame.

The three regions of an ideal, one-dimensional premixed propane flame are depicted in Fig. 2.2. In the preheat zone, the reactants are already mixed, but do not react. With progressing spatial coordinate x , heat from the inner layer diffuses into the preheat zone, causing the temperature to rise until the activation energy is reached. The ongoing reaction converts C_3H_8 and O_2 into CO_2 and H_2O , as evident from their mass fractions. Since the reaction is exothermic, the temperature rises rapidly. In the post flame zone, most elementary reactions are completed and only slower reactions take place, causing the temperature to increase more slowly. Finally, equilibrium is reached and the reaction is completed.

In a quiescent, unburnt mixture, the propagation of a flame is only determined by the chemical reactions and the thermodynamic properties of the medium. Its

propagation velocity, the *laminar flame velocity* s_l only depends on the stoichiometric conditions, the unburnt temperature and the pressure. The *laminar flame thickness* δ_l is defined as the temperature difference between burnt T_b and unburnt T_u state, divided by the maximum temperature gradient

$$\delta_l = \frac{T_b - T_u}{\max\left(\frac{\partial T}{\partial x}\right)}. \quad (2.59)$$

Typical values for the laminar flame thickness are in the range of 0.1 mm, with smaller values close to stoichiometry.

As laid out in section 2.2, the turbulent motions can be perpendicular to the direction of the mean flow. Consequently, in turbulent combustion, the flame front does not propagate at spatially and temporally constant velocity but is wrinkled by the turbulent motions as depicted in Fig. 2.3b. Compared to the laminar flame

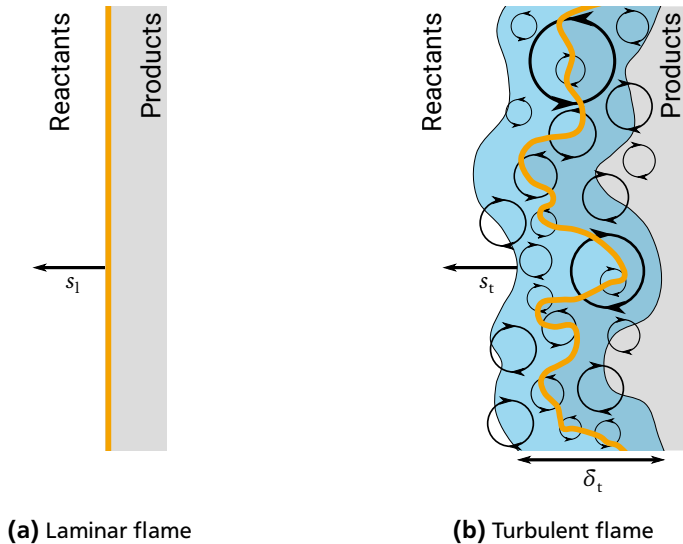


Figure 2.3: Laminar and turbulent flame fronts.

in Fig. 2.3a, the surface of the turbulent flame is enlarged. From a macroscopic view, its overall thickness is hence increased, so that the flame is now perceived as the blue area, the so called flame brush. Its thickness is denoted by the turbulent flame thickness δ_t . The increased surface effects an increased fuel consumption

rate and effective flame speed, the *turbulent flame speed* s_t . The ratio of turbulent and laminar flame speed is therefore given by the enlargement of the flame surface:

$$\frac{s_t}{s_l} = \frac{S_t}{S_l}. \quad (2.60)$$

According to the Boussinesq approximation, the effect of turbulence can be modeled as an increased diffusivity. For small scale turbulence, the turbulent flame speed is therefore expressed in terms of the laminar flame speed and the ratio of turbulent and laminar viscosity:

$$\frac{s_t}{s_l} \propto \sqrt{\frac{\nu_t}{\nu}}. \quad (2.61)$$

2.3.3 Combustion Modeling

For the combustion of propane, Eq. (2.3.1), the detailed GRI-3.0 reaction mechanism [127] involves a total number of 325 elementary reactions and 53 species. A detailed treatment of the individual reactions would hence require the solution of an additional 53 transport equations (2.39c) and 325 reaction rate equations (2.56) at every time step. Moreover, the time scales of the different reactions span a wide range from $10E-9$ s to 1 s, that need to be resolved by an appropriately small CFD time step size. The wide range of scales also increases the stiffness of the system of reaction rate equations, which aggravates its numerical treatment. Each point by itself, the small timescales, the high number of additional transport equations and the stiff reaction rate system requires an excessive amount of computational time. A modeling procedure based on the elementary reactions is therefore not feasible for technical applications.

These restrictions are partly alleviated by approximating the detailed mechanisms with reduced ones, bringing the number of additional transport equations to a level that can be met for academic test cases. However, this technique is only applicable to a specific range of operating conditions, which the mechanisms were designed for and does not necessarily solve the problem of the small time scales.

A more economical alternative is the tabulated chemistry approach. Instead of accounting for the reactions during the CFD simulation, a chemistry database is created prior to the CFD simulation, that contains densities, temperatures, viscosities, source terms and mass fractions. These values are looked up from the database at run time using only a few parameters, for which transport equations need to be solved. In addition to avoiding the solution of the reaction rate system and the high number of additional transport equations, this approach encodes the small time scale reactions in the database. Therefore, it does not introduce any time step restrictions.

2.3.3.1 Flamelet Generated Manifolds

For premixed combustion, two similar approaches have been developed independently of each other, the *Flamelet Generated Manifold* (FGM) method [104, 106, 105] and the *Flame Prolongation of Intrinsic Low Dimensional Manifold* (FPI) [44, 43]. The current state of the art in FGM modeling is reviewed in [103]. The fundamental idea of this modeling technique is that a three-dimensional, turbulent flame can be sufficiently described by an ensemble of states found in a set of corresponding laminar flames. These *flamelets* can be computed for a variety of different boundary conditions and stored in a table, referred to as *manifold*.

In the current work, the combustion is accounted for by means of the FGM technique and the flamelets are computed with the software tool CHEM1D [32]. In this process, a universal Lewis number of $Le = 1$ is assumed and extrapolation is used outside the flammability limits, as described by Aschmoneit [6]. The manifold is accessed by two parameters, the mixture fraction \mathcal{Z} and a progress variable \mathcal{C} . For a finite number of mixture fractions, flamelets are precomputed and stored, while the progress variable is used to identify a state within each flamelet.

Mixture Fraction

The mixture fraction indicates the mixing of fuel and oxidizer, attaining values between zero (pure oxidizer) and one (pure fuel). With $Le = 1$, its transport equation follows as:

$$\frac{\partial \rho \mathcal{Z}}{\partial t} + \frac{\partial \rho u_i \mathcal{Z}}{\partial x_i} = \frac{\partial}{\partial x_i} \left(\frac{\mu}{Sc} \frac{\partial \mathcal{Z}}{\partial x_i} \right). \quad (2.62)$$

Just like for the velocity, enthalpy and species equations, the Favre averaging gives rise to a subgrid mixture fraction part $\tau^{\text{sgs}, \mathcal{Z}}$. It is modeled consistently with its enthalpy and species counterparts (2.53), by means of a gradient flux approach:

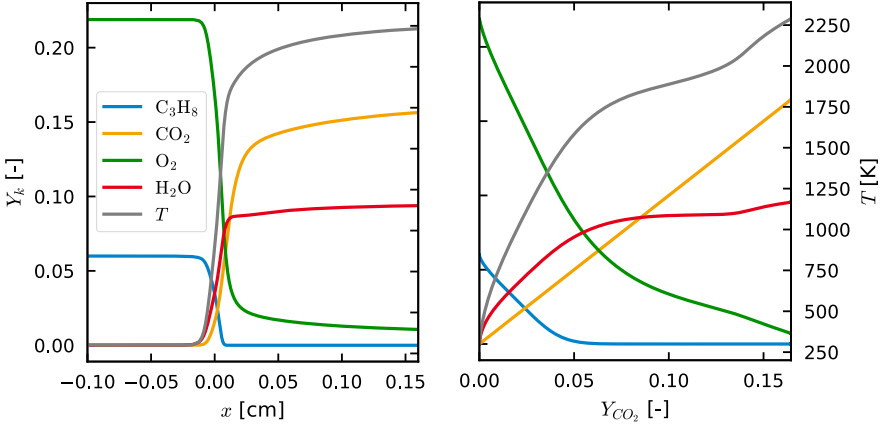
$$\tau^{\text{sgs}, \mathcal{Z}} = - \frac{\nu_t}{Sc_t} \frac{\partial \tilde{\mathcal{Z}}}{\partial x_i}. \quad (2.63)$$

In the LES context, the mixture fraction then reads:

$$\frac{\partial \bar{\rho} \tilde{\mathcal{Z}}}{\partial t} + \frac{\partial \bar{\rho} \tilde{u}_i \tilde{\mathcal{Z}}}{\partial x_i} = \frac{\partial}{\partial x_i} \left(\frac{\bar{\mu} + \mu_t}{Sc} \frac{\partial \tilde{\mathcal{Z}}}{\partial x_i} \right). \quad (2.64)$$

Progress Variable

In order to link a location \mathbf{x} in a three-dimensional flame to a state within a flamelet, a mapping between flamelet and flame is required. While for the flamelet



(a) Mass fractions and temperature over location.

(b) Mass fractions and temperature over progress variable Y_{CO_2} .

Figure 2.4: A propane-flamelet at $\mathcal{Z} = 0.6$, $p = 2.01$ bar and $T = 315$ K. Discretized by 25 equidistant nodes along the Y_{CO_2} -axis.

location, no corresponding quantity can be easily identified in a 3D flame, transport equations for the species mass fractions Y_k are available. Therefore, instead of parameterizing the flamelet by its location, a new quantity, the progress variable \mathcal{C} is introduced. As long as it is monotone along the spatial coordinate x and defined for all stoichiometric conditions, any mass fraction or linear combination of mass fractions qualifies as progress variable. For the methane and propane flames explored in this work, the CO_2 mass fraction Y_{CO_2} was chosen for its wide and therefore easily resolvable source term. To simplify the modeling of turbulence-chemistry interaction with the *presumed PDF* (PPDF) approach, introduced in section 2.3.3.1, the progress variable is normalized with its equilibrium value:

$$\mathcal{C} := \frac{Y_{CO_2} - \min(Y_{CO_2})}{\max(Y_{CO_2}) - \min(Y_{CO_2})}. \quad (2.65)$$

As evident from Fig. 2.4, the parametrization of a flamelet over \mathcal{C} instead of x is equivalent to a coordinate transform. When the flamelet is stored in the manifold using an equidistant discretization, this transform is identical to a node refinement at steep \mathcal{C} gradients. If this gradient coincides well with the gradients of other species, the progress variable transformation can also vastly reduce the discretiza-

tion error of the flamelet. The smooth gradients of the parametrized flamelet in 2.4b indicate that this applies very well to Y_{CO_2} , which corroborates this choice.

Chemistry Table

With one transformed and discretized flamelet for each mixture fraction, the chemistry database or *manifold* holds the results of the detailed flamelet computations, accessible from two parameters, the progress variable \mathcal{C} and the mixture fraction \mathcal{Z} :

$$q_{\text{tab}}(\mathcal{Z}, \mathcal{C}). \quad (2.66)$$

For each quantity stored in the table, the manifold can be visualized as three-dimensional surface over mixture fraction and progress variable, see Fig. 2.5.

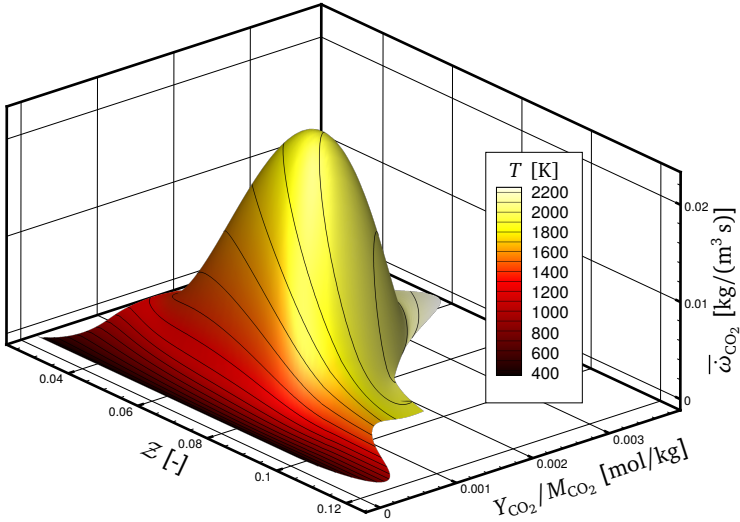


Figure 2.5: Propane manifold for $p = 2.01$ bar and $T = 315$ K, using 100 discrete mixture fraction values and 25 nodes for each flamelet. Temperature and CO_2 -source term over mixture fraction and progress variable (Y_{CO_2}).

The Manifold holds redundant information, such as the temperature, enthalpy, or density, which is computed from solving the system of governing equations. For adiabatic conditions, where no thermal conduction across the domain boundaries is considered, this information is identical. Therefore, the enthalpy equation can be omitted and replaced by a much faster table lookup.

Turbulence-Chemistry Interaction

In the LES context, transport equations are only solved for the Favre averaged quantities, while their corresponding subgrid parts are modeled. Therefore, the filtered equivalents of viscosity, density and source terms are required to close the governing equations. However, due to the non-linearity of the Favre averaging, a lookup with the filtered mixture fraction \tilde{Z} and the progress variable \tilde{C} does not yield a filtered quantity:

$$\tilde{q}_{\text{tab}}(\mathcal{Z}, \mathcal{C}) \neq q_{\text{tab}}(\tilde{Z}, \tilde{C}). \quad (2.67)$$

The difference between a filtered and unfiltered quantity stems from the chemistry-turbulence interaction and is mathematically represented as unknown joint *Probability Density Function* (PDF) $\mathcal{P}(\mathcal{Z}, \mathcal{C})$. A filtered quantity \tilde{q} in a single cell is then given as:

$$\tilde{q}_{\text{tab}}(\mathcal{Z}, \mathcal{C}) = \iint q_{\text{tab}}(\mathcal{Z}, \mathcal{C}) \mathcal{P}(\mathcal{Z}, \mathcal{C}) d\mathcal{Z} d\mathcal{C}. \quad (2.68)$$

Due to the normalization of the progress variable (2.65), the statistical dependency between \mathcal{Z} and \mathcal{C} is minimized. This allows for splitting the joint PDF into two separate probability density functions:

$$\mathcal{P}(\mathcal{Z}, \mathcal{C}) \approx \mathcal{P}(\mathcal{Z}) \mathcal{P}(\mathcal{C}). \quad (2.69)$$

In the presumed PDF approach, the distributions for $\mathcal{P}(\mathcal{C})$ and $\mathcal{P}(\mathcal{Z})$ are assumed to be only functions of the filtered access parameters and their statistical moments. This allows to perform the above integration during preprocessing and to store the results in the chemistry table. Thereby, the computational effort is significantly reduced compared to e.g. introducing and solving additional transport equations for the PDFs. As rationalized by Aschmoneit [6], a β -PDF is used for the mixture fraction and a δ -PDF for the progress variable. After integration of the original chemistry table $q_{\text{tab}}(\mathcal{Z}, \mathcal{C})$, all values are stored in a new, pre-integrated table $\tilde{q}_{\text{int}}(\tilde{Z}, \overline{Z''^2}, \tilde{C})$:

$$\tilde{q}_{\text{tab}}(\mathcal{Z}, \mathcal{C}) = \tilde{q}_{\text{int}}(\tilde{Z}, \overline{Z''^2}, \tilde{C}) := \iint q_{\text{tab}}(\mathcal{Z}, \mathcal{C}) \mathcal{P}_{\beta}(\tilde{Z}, \overline{Z''^2}) \mathcal{P}_{\delta}(\tilde{C}) d\mathcal{Z} d\mathcal{C}. \quad (2.70)$$

The filtered quantities are then accessed by the filtered mixture fraction \tilde{Z} , the filtered progress variable \tilde{C} and the variance of the mixture fraction $\overline{Z''^2}$. \tilde{Z} and \tilde{C} are obtained from their respective transport equations (2.64) and (2.10), whereas for $\overline{Z''^2}$, an additional transport equation, as derived by Jiménez et al. [59] and Kemenov et al. [64] is employed:

$$\frac{\partial \overline{\rho} \overline{Z''^2}}{\partial t} + \frac{\partial \overline{\rho} \tilde{u}_i \overline{Z''^2}}{\partial x_i} = \frac{\partial}{\partial x_i} \left(\frac{\bar{\mu} + \mu_t}{Sc} \frac{\partial \overline{Z''^2}}{\partial x_i} \right) - 2 \frac{\mu_t}{Sc} \left(\frac{\partial \tilde{Z}}{\partial x_i} \right)^2 - 2 \mu_t \frac{\overline{Z''^2}}{\Delta h_{\text{filt}}^2}. \quad (2.71)$$

2.3.3.2 Artificially Thickened Flame

The flame thickness is generally in the range of 0.1 mm and becomes even thinner under e.g. high pressure or when turbulence is involved [71]. In this case, the flame is about one magnitude thinner than the smallest resolved scales of the LES technique and spatially resolving it becomes excessively inefficient. The *Artificially Thickened Flame* (ATF) approach [16, 102] was developed to overcome this problem by locally thickening the flame so that its dimensions are within the LES resolution. In this work, the implementation of the ATF technique is based on Aschmoneit [6], where further information and derivations can be found.

By introducing a thickening factor \mathcal{F} in the species equation (2.10), the diffusivity is artificially increased and the source term is decreased:

$$\frac{\partial \rho Y_k}{\partial t} + \frac{\partial \rho u_i Y_k}{\partial x_i} = \frac{\partial}{\partial x_i} \left(\mathcal{F} \frac{\mu}{Sc_k} \frac{\partial Y_k}{\partial x_i} \right) + \frac{\dot{\omega}_k}{\mathcal{F}}. \quad (2.72)$$

According to premixed flame theories [140], the laminar flame speed and thickness follow as

$$\delta_1 \propto \sqrt{\frac{\mathcal{D}}{\dot{\omega}}} = \sqrt{\mathcal{F} \frac{\mu}{Sc_k} \frac{\mathcal{F}}{\dot{\omega}_k}} \quad \text{and} \quad s_1 \propto \sqrt{\mathcal{D} \dot{\omega}} = \sqrt{\mathcal{F} \frac{\mu}{Sc_k} \frac{\dot{\omega}_k}{\mathcal{F}}}. \quad (2.73)$$

Therefore, the thickening factor linearly increases the laminar flame thickness while the laminar flame speed is not affected.

With this technique, the thickening factor should ideally be chosen to allow for a proper flame resolution without adding unnecessary diffusion to the model. In the FGM context described in section 2.3.3.1, Kuenne et al. [71] found the resolution of the progress variable source term to be crucial. Based on numerical experiments with FVM discretization, they conclude that the flame should be discretized by at least three control volumes, suggesting a thickening factor of

$$\mathcal{F}_{\max}(\mathbf{x}) = \max \left(1, \frac{h}{1/3 \delta_1} \right). \quad (2.74)$$

Besides by combustion, species gradients can also be caused by mixing. Globally increasing the species diffusivity can therefore lead to an unwanted smoothing of the flow field. This is avoided by disabling thickening outside of the flame by setting $\mathcal{F} = 1$. To this end, the flame is detected by a flame sensor \mathcal{S} , which adjusts the thickening factor as:

$$\mathcal{F}(\mathbf{x}) = 1 + (\mathcal{F}_{\max}(\mathbf{x}) - 1) \mathcal{S}(\mathbf{x}). \quad (2.75)$$

The flame sensor is based on the progress variable [30] and takes values between zero and one:

$$\mathcal{S} = 16[\mathcal{C}(1 - \mathcal{C})]^2. \quad (2.76)$$

Turbulence-Chemistry Interaction

Since for turbulent flames, the ATF technique only alters the flame thickness without changing the turbulent scales, the interaction between the turbulent motions and the flame is distorted. This causes the wrinkling of the flame front, described in section 2.3.2 to be underpredicted, leading to a reduced turbulent flame speed and consequently a degraded accuracy of the model. The decreased flame speed is counteracted by introducing an efficiency function \mathcal{E} , which emulates the surface increase due to turbulence and therefore the increased flame speed:

$$\mathcal{E} = \frac{S_t}{S_1} = \frac{s_t}{s_1}. \quad (2.77)$$

It is multiplied with both, the diffusion and source term of the thickened species equation

$$\frac{\partial \rho Y_k}{\partial t} + \frac{\partial \rho u_i Y_k}{\partial x_i} = \frac{\partial}{\partial x_i} \left(\mathcal{F} \mathcal{E} \frac{\mu}{Sc_k} \frac{\partial Y_k}{\partial x_i} \right) + \frac{\mathcal{E}}{\mathcal{F}} \dot{\omega}_k \quad (2.78)$$

and contrary to the thickening factor increases the flame speed, while leaving the flame thickness unaffected.

The efficiency function is not easily determined and hence requires additional modeling. In the present work, the definition proposed by Charlette et al. [22] is used. The unresolved flame surface is described by a power law that was derived from DNS data of flame-vortex interaction as described by Aschmoneit [6].

Implementation with the FGM Method

The ATF technique is independent from the combustion modeling approach, as it does not contain any assumptions regarding the actual model. In this work, it is combined with the FGM model, as first reported by Kuenne et al. [71]. To resolve the flame, the thickening is applied to the transport equations for mixture fraction \tilde{Z} and progress variable \tilde{C} . In the thickened region, the flame is fully resolved by the mesh and the subgrid parts of \mathcal{Z} and \mathcal{C} vanish. Consequently, the variance of the mixture fraction $\overline{\mathcal{Z}''^2}$ is zero in the flame region and no such transport equation needs to be solved. Since for $\overline{\mathcal{Z}''^2} = 0$, the values obtained from $\tilde{q}_{\text{int}}(\tilde{Z}, \overline{\mathcal{Z}''^2}, \tilde{C})$ and $q_{\text{tab}}(\mathcal{Z}, \mathcal{C})$ are identical, the pre-integrated chemistry table can still be used with ATF.

Outside of the flame, where no thickening is applied ($\mathcal{E} = \mathcal{F} = 1$), the model resorts to the gradient flux approach for \tilde{Z} and \tilde{C} and uses the flame sensor to blend between the two strategies. In summary, the low Mach number, Favre-averaged

governing equations with LES turbulence modeling, FGM combustion modeling and ATF are given as

$$\frac{\partial \bar{\rho}}{\partial t} + \frac{\partial \bar{\rho} \tilde{u}_i}{\partial x_i} = 0 \quad (2.79a)$$

$$\frac{\partial \bar{\rho} \tilde{u}_j}{\partial t} + \frac{\partial \bar{\rho} \tilde{u}_i \tilde{u}_j}{\partial x_i} = -\frac{\partial \overline{p^{\text{mod}}}}{\partial x_j} + \frac{\partial}{\partial x_i} \left(\bar{\mu} \left(\frac{\partial \tilde{u}_i}{\partial x_j} + \frac{\partial \tilde{u}_j}{\partial x_i} \right) - \frac{2}{3} \bar{\mu} \frac{\partial \tilde{u}_m}{\partial x_m} \delta_{ij} - \bar{\rho} \tau_{ij}^{\text{sgs},u} \right) \quad (2.79b)$$

$$\frac{\partial \bar{\rho} \tilde{Z}}{\partial t} + \frac{\partial \bar{\rho} \tilde{u}_i \tilde{Z}}{\partial x_i} = \frac{\partial}{\partial x_i} \left(\frac{\mathcal{F} \mathcal{E} \bar{\mu} + (1 - \mathcal{S}) \mu_t}{Sc} \frac{\partial \tilde{Z}}{\partial x_i} \right) \quad (2.79c)$$

$$\frac{\partial \bar{\rho} \tilde{C}}{\partial t} + \frac{\partial \bar{\rho} \tilde{u}_i \tilde{C}}{\partial x_i} = \frac{\partial}{\partial x_i} \left(\frac{\mathcal{F} \mathcal{E} \bar{\mu} + (1 - \mathcal{S}) \mu_t}{Sc} \frac{\partial \tilde{C}}{\partial x_i} \right) + \frac{\mathcal{E}}{\mathcal{F}} \bar{\omega}_c \quad (2.79d)$$

$$\tilde{q}_{\text{int}}(\tilde{Z}, 0, \tilde{C}) \mapsto \bar{\mu}, \bar{\rho}, \bar{\omega}_c, \quad (2.79e)$$

where the turbulent subgrid stresses $\tau_{ij}^{\text{sgs},u}$ are modeled according to section 2.2.2.2.

2.4 Governing Equations for Aeroacoustics

Under certain conditions, an equation system such as the compressible flow governing equations (2.1, 2.4, 2.16) can be rearranged to yield an equivalent system of linear independent equations. Each of these *characteristic equations* autonomously describes the transport of a single quantity, a *characteristic variable* of the original governing equations. For the single species, compressible flow governing equations (2.1, 2.4, 2.16), these quantities correspond to acoustic, entropy and vorticity waves [50]. As laid out in section 2.1.6, the low Mach number flow governing equations (2.24) only describe propagation of the vorticity and entropy waves and therefore do not qualify for modeling acoustic phenomena. Consequently, they must be augmented by an additional set of governing equations that does account for acoustic wave propagation. The compressible field is thereby decomposed into a low Mach number part q^{loMa} , described by the low Mach number flow governing equations (2.24) and an acoustic perturbation q^a :

$$q = q^{\text{loMa}} + q^a. \quad (2.80)$$

For the sake of brevity, the superscript q^{loMa} is omitted hereafter.

Exploiting the small amplitudes of the acoustic part q^a , the acoustic decomposition can be used to linearize a set of compressible governing equations with regard

to the low Mach number state q^{loMa} . To this end, all higher order terms and the acoustic mechanisms they account for, are neglected. Examples of such governing equations are the Linearized Euler Equations and the *Linearized Navier-Stokes Equations* (LNSE). In addition to the aforementioned reduced computational cost due to the scale separation, the numerical treatment of linearized equations requires significantly less computational effort than solving their non-linearized counterparts, which further improves the efficiency of the hybrid CAA.

2.4.1 Acoustic Perturbation Equations

Besides acoustic wave propagation, the linearized equation systems still model vorticity and entropy transport. These non-acoustic waves tend to become unstable [34] and spoil the result of the simulation. As a remedy, Ewert and Schröder proposed four APE variants [34, 33], which are based on a source filtering technique, that prevents these modes from being excited a priori. To this end, a system of flow governing equations is established, that accounts for acoustic and entropy wave transport. This system is then transformed into wave number/frequency space, so that an acoustic source vector can be derived, which only excites acoustic eigenmodes. Due to the initial choice of equations and the filtered source formulation, possibly unstable entropy and vorticity modes are hence excluded a priori. By introducing a decomposition and rearranging the resulting system, the authors finally arrive at the APE-1 system. The APE-1 exclusively describe the transport of acoustic perturbations³ without considering non-linear effects, but are valid for non-uniform base flows.

Starting from the APE-1, the authors derive the APE-2 system for incompressible base flows. Although this reintroduces the entropy modes, the APE-2 are shown to be unconditionally stable for arbitrary base flows. Since the source terms of the APE-1 require the solution of a Poisson equation, the authors go on to propose the APE-4 system, whose source terms can be computed explicitly. The APE-4 are derived by rearranging a disturbance formulation of the continuity and Navier-Stokes equations, to yield an identical left hand side as in the APE-1. This left hand side, referred to as *APE-1/4 operator*, hence possesses the same favorable properties

³ Vorticity waves are still present in the APE-1/4 operator, but as shown in section 2.4.3, they are not transported.

as the APE-1 and consequently forms the basis of the acoustic governing equations used throughout this work. The homogeneous APE-1/4 equations read:

$$\frac{\partial p^a}{\partial t} + \langle c \rangle^2 \nabla \cdot \left(\langle \varrho \rangle \mathbf{u}^a + \langle \mathbf{u} \rangle \frac{p^a}{\langle c^2 \rangle} \right) = 0 \quad (2.81a)$$

$$\frac{\partial \mathbf{u}^a}{\partial t} + \nabla (\langle \mathbf{u} \rangle \cdot \mathbf{u}^a) + \nabla \left(\frac{p^a}{\langle \varrho \rangle} \right) = 0. \quad (2.81b)$$

It is only because this operator models acoustic wave propagation exclusively, that the decomposition 2.80 into a low Mach number and acoustic part is valid. Unlike the APE, the operators of other linearized systems, such as the LEE, do account for vorticity and entropy wave transport. Since this is already covered by the low Mach number governing equations (2.79), such a combination would give ambiguous results without special treatment of e.g. the corresponding source terms.

2.4.2 Acoustic Perturbation Equations for Reacting Low Mach Number Flows

Based on [34], specialized APE variants for reacting flows have been proposed. With a similar procedure used to arrive at the APE-2 equations, Bui [11] derived the APE-RF equations by rearranging the compressible flow governing equations for reacting flows (2.1, 2.4, 2.16) to yield:

$$\frac{\partial \varrho^a}{\partial t} + \nabla \cdot (\langle \varrho \rangle \mathbf{u}^a + \varrho^a \langle \mathbf{u} \rangle) = \dot{\omega}_c \quad (2.82a)$$

$$\frac{\partial \mathbf{u}^a}{\partial t} + \nabla (\langle \mathbf{u} \rangle \cdot \mathbf{u}^a) + \nabla \left(\frac{p^a}{\langle \varrho \rangle} \right) = \dot{\omega}_m \quad (2.82b)$$

$$\frac{\partial p^a}{\partial t} - \langle c \rangle^2 \frac{\partial \varrho^a}{\partial t} = \dot{\omega}_e, \quad (2.82c)$$

where $\dot{\omega}_c$, $\dot{\omega}_m$ and $\dot{\omega}_e$ denote the acoustic source terms. The APE-2 and APE-RF only differ with regard to the source terms on the right hand side, which are computed from a compressible or low Mach number based flow simulation. However, the APE-2 operator is designed to be used in conjunction with incompressible flow governing equations that do not account for the transport of entropy perturbations, unlike the low Mach number equations used in this work. A more adequate formulation with an APE-1/4 type operator was derived by Geiser et al. [39], who combined (2.82c) and (2.82a) to obtain the *revised APE*:

$$\frac{\partial p^a}{\partial t} + \langle c^2 \rangle \nabla \cdot \left(\langle \varrho \rangle \mathbf{u}^a + \langle \mathbf{u} \rangle \frac{p^a}{\langle c^2 \rangle} \right) = \langle c^2 \rangle \dot{\omega}_c + \dot{\omega}_e + \dot{\omega}_{c\&e} \quad (2.83a)$$

$$\frac{\partial \mathbf{u}^a}{\partial t} + \nabla (\langle \mathbf{u} \rangle \cdot \mathbf{u}^a) + \nabla \left(\frac{p^a}{\langle \varrho \rangle} \right) = \dot{\omega}_m. \quad (2.83b)$$

Besides using $\langle c^2 \rangle$ instead of $\langle c \rangle^2$, the revised APE operator is identical to the original APE-1/4 formulation by Ewert and Schröder [34]. The individual source terms arise from the equation of mass conservation ($\dot{\omega}_c$), the energy equation ($\dot{\omega}_e$), the momentum equation ($\dot{\omega}_m$) and the coupling of linearized mass conservation and pressure-density relation ($\dot{\omega}_{c\&e}$):

$$\dot{\omega}_c = -\nabla \cdot (\rho' \mathbf{u}') \quad (2.84a)$$

$$\dot{\omega}_e = -\langle c^2 \rangle \frac{\partial \rho_e}{\partial t} \quad (2.84b)$$

$$\dot{\omega}_{c\&e} = -\langle c^2 \rangle \nabla \cdot (\langle \mathbf{u} \rangle \rho_e) \quad (2.84c)$$

$$\dot{\omega}_m = -((\nabla \times \mathbf{u}) \times \mathbf{u})' - \nabla \kappa' + \nabla \left(\frac{p}{\langle \rho \rangle} \right)' - \left(\frac{\nabla p}{\rho} \right)' + \left(\frac{\nabla \cdot \boldsymbol{\tau}}{\rho} \right)' + \sum_{k=1}^{N_s} (\rho_k \mathbf{g}_k)' , \quad (2.84d)$$

where the excess density

$$\rho_e = \rho' - \frac{p'}{\langle c^2 \rangle} \quad (2.85)$$

originates from the pressure density relation (2.82c). Eqs. (2.84) involve several temporal fluctuations and even fluctuations of terms that involve fluctuations. In order to compute these quantities, their temporal means are required first. However, these are only available after a sufficiently long simulated time span. This significantly increases the computational cost of the overall method and hence deteriorates its efficiency and applicability to industrial applications. For this reason, a simpler formulation by Geiser et al. [41] is used, that neglects most source terms by limiting the scope to reacting low Mach number flows.

Under these conditions, the pressure perturbation is negligible compared to the density perturbation [11] and accordingly, ρ_e simplifies to:

$$\frac{p'}{\langle c^2 \rangle} \ll \rho' \quad \Rightarrow \quad \rho_e \approx \rho' . \quad (2.86)$$

While in non-reactive, isothermal flows, the acoustic source terms are usually dominated by the lamb vector $((\nabla \times \mathbf{u}) \times \mathbf{u})$ in the momentum source $\dot{\omega}_m$, Geiser et al. [41] found the energy source $\dot{\omega}_e$ to be essential in reactive flows. With these two

simplifications, the low Mach number source terms [11] for reactive flows take the form

$$\dot{\omega}_{c,\text{lowMa}} = 0 \quad (2.87a)$$

$$\dot{\omega}_{e,\text{lowMa}} = -\langle c^2 \rangle \frac{\partial \varrho'}{\partial t} \quad (2.87b)$$

$$\dot{\omega}_{c\&e,\text{lowMa}} = 0 \quad (2.87c)$$

$$\dot{\omega}_{m,\text{lowMa}} = 0. \quad (2.87d)$$

The revised APE-1/4 operator (2.83) is derived based on the temporal means of c^2 , \mathbf{u} and ϱ . For the simulation of highly unstable flames, such as the pressurized combustor in chapter 7, the flame movement significantly alters all three quantities in large regions of the computational domain. Consequently, an acoustic modeling based on temporal means is not able to adequately account for sound propagation under these conditions. However, for the investigated application of low Mach number combustion noise, the time scales of the flow field are magnitudes larger than those of the acoustics described by the APE. Exploiting this discrepancy, the mean quantities of the APE-1/4 operator (2.83) are replaced by their instantaneous, Favre-averaged equivalents. Since $\partial \langle \varrho \rangle / \partial t = 0$, the temporal derivative in the energy source term (2.87b) can be directly evaluated as $\partial \varrho / \partial t$. This removes all temporal means and perturbations from the acoustic governing equations and no expensive time averaging is required anymore, before a coupled CFD-CAA simulation can be started. While the simplifying assumptions inherent to this reduced source term formulation may impact its applicability to complex flow problems, the mechanisms involved in the essential noise generation due to unsteady heat release are accounted for. For low Mach number, reacting flows, the revised APE are given as:

$$\frac{\partial p^a}{\partial t} + \overline{c^2} \nabla \cdot \left(\overline{\varrho} \mathbf{u}^a + \tilde{\mathbf{u}} \frac{p^a}{c^2} \right) = -\overline{c^2} \frac{\partial \overline{\varrho}}{\partial t} \quad (2.88a)$$

$$\frac{\partial \mathbf{u}^a}{\partial t} + \nabla (\tilde{\mathbf{u}} \cdot \mathbf{u}^a) + \nabla \left(\frac{p^a}{\overline{\varrho}} \right) = 0. \quad (2.88b)$$

2.4.3 Acoustic Perturbation Equations in Characteristic Variables

To further illustrate how the APE-1/4 operator accounts for acoustic wave propagation only, it is rewritten in terms of characteristic variables. Therefore, a uniform speed of sound is assumed, so that the c^2 term can be moved into the divergence.

While this is not warranted in reactive flows, it serves the purpose of illustration. As laid out in chapter 3 the resulting diagonalized form is also inherent to the Riemann solvers and the boundary conditions. For these applications, the constant c assumption still holds, since only different states in identical locations with identical c are considered. Consequently, the homogeneous APE-1/4 equations (2.81) can be brought into a fluxes based formulation as:

$$\frac{\partial \mathbf{U}}{\partial t} + \frac{\partial \mathbf{F}_1}{\partial x_1} + \frac{\partial \mathbf{F}_2}{\partial x_2} + \frac{\partial \mathbf{F}_3}{\partial x_3} = \mathbf{W} \quad (2.89)$$

with

$$\mathbf{U} = \begin{bmatrix} p^a \\ u_1^a \\ u_2^a \\ u_3^a \end{bmatrix}, \quad \mathbf{W} = \begin{bmatrix} 0 \\ 0 \\ 0 \\ 0 \end{bmatrix},$$

$$\mathbf{F}_1 = \begin{bmatrix} \bar{\rho} \bar{c}^2 u_1^a + p^a \tilde{u}_1 \\ \tilde{u}_j u_j^a + p^a / \bar{\rho} \\ 0 \\ 0 \end{bmatrix}, \quad \mathbf{F}_2 = \begin{bmatrix} \bar{\rho} \bar{c}^2 u_2^a + p^a \tilde{u}_2 \\ 0 \\ \tilde{u}_j u_j^a + p^a / \bar{\rho} \\ 0 \end{bmatrix}, \quad \mathbf{F}_3 = \begin{bmatrix} \bar{\rho} \bar{c}^2 u_3^a + p^a \tilde{u}_3 \\ 0 \\ 0 \\ \tilde{u}_j u_j^a + p^a / \bar{\rho} \end{bmatrix}.$$

For the three-dimensional formulation, the aforementioned diagonalization is not possible because no single eigenvector, that applies to all three flux jacobians $\mathbf{J}_i = \partial \mathbf{F}_i / \partial \mathbf{U}$ exists. Consequently, the special case where a plane wave travels in x_1 -direction through a uniform flow field is considered. With these simplifications, Eq. (2.89) becomes

$$\frac{\partial \mathbf{U}}{\partial t} + \mathbf{J}_1 \frac{\partial \mathbf{U}}{\partial x_1} = 0. \quad (2.90)$$

The eigendecomposition $\mathbf{J}_1 = \mathbf{L}_1 \mathbf{\Lambda}_1 \mathbf{L}_1^{-1}$ of the flux jacobian \mathbf{J}_1 yields a square matrix of its eigenvectors \mathbf{L}_1 and the diagonal eigenvalue matrix $\mathbf{\Lambda}_1 = \text{diag}(\lambda_j)$:

$$\mathbf{L}_1 = \begin{bmatrix} \frac{\bar{\rho} \bar{c}^2 \tilde{u}_2}{\tilde{u}_1^2 - \bar{c}^2} & \frac{\bar{\rho} \bar{c}^2 \tilde{u}_3}{\tilde{u}_1^2 - \bar{c}^2} & -\bar{\rho} \sqrt{c^2} & \bar{\rho} \sqrt{c^2} \\ \frac{\tilde{u}_1 \tilde{u}_2}{c^2 - \tilde{u}_1^2} & \frac{\tilde{u}_1 \tilde{u}_3}{c^2 - \tilde{u}_1^2} & 1 & 1 \\ 1 & 0 & 0 & 0 \\ 0 & 1 & 0 & 0 \end{bmatrix}, \quad \mathbf{\Lambda}_1 = \begin{bmatrix} 0 & 0 & 0 & 0 \\ 0 & 0 & 0 & 0 \\ 0 & 0 & \tilde{u}_1 - \sqrt{c^2} & 0 \\ 0 & 0 & 0 & \tilde{u}_1 + \sqrt{c^2} \end{bmatrix}.$$

Finally, the diagonalized form of the Eq. (2.90) is obtained by left-multiplication with L_1^{-1} and substitution of J_1 with its eigendecomposition $L_1 \Lambda_1 L_1^{-1}$:

$$\frac{\partial \mathbf{H}_1}{\partial t} + \Lambda_1 \frac{\partial \mathbf{H}_1}{\partial x_1} = 0. \quad (2.91)$$

Therein, the characteristic variables $\mathbf{H}_1 = L_1^{-1} U$ are

$$\mathbf{H}_1 = \begin{bmatrix} \mathcal{h}_1 \\ \mathcal{h}_2 \\ \mathcal{h}_3 \\ \mathcal{h}_4 \end{bmatrix} = \begin{bmatrix} u_2^a \\ u_3^a \\ \frac{\tilde{u}_2 u_2^a (\sqrt{c^2 + \tilde{u}_1})}{2\tilde{u}_1^2 - 2c^2} + \frac{\tilde{u}_3 u_3^a (\sqrt{c^2 + \tilde{u}_1})}{2\tilde{u}_1^2 - 2c^2} + \frac{u_1^a}{2} - \frac{p^a}{2\bar{\rho}\sqrt{c^2}} \\ \frac{\tilde{u}_2 u_2^a (\sqrt{c^2 - \tilde{u}_1})}{2c^2 - 2\tilde{u}_1^2} + \frac{\tilde{u}_3 u_3^a (\sqrt{c^2 - \tilde{u}_1})}{2c^2 - 2\tilde{u}_1^2} + \frac{u_1^a}{2} + \frac{p^a}{2\bar{\rho}\sqrt{c^2}} \end{bmatrix}.$$

Just like the simplified APE (2.90), their diagonalized form (2.91) is an advection equation, describing the transport of \mathbf{H}_1 in x_1 -direction. However, since Λ_1 is diagonal, the transport of each component of \mathbf{H}_1 is now represented independently from the other components. Therefore, each eigenvalue λ_j marks the velocity at which the characteristic \mathcal{h}_j is transported. Since $\lambda_1 = \lambda_2 = 0$, the first two characteristic variables \mathcal{h}_1 and \mathcal{h}_2 , which are related to the vorticity waves are not transported. The third and fourth variables \mathcal{h}_3 and \mathcal{h}_4 account for the acoustic waves, which, for subsonic flows, travel at $\approx \tilde{u}_1 \pm \bar{c}$ into positive and negative x -directions. Accordingly, the APE-1/4 operator does neither model entropy waves, nor does it transport vorticity waves. It accounts for acoustic wave propagation exclusively.

2.4.4 Acoustic Feedback onto the Low Mach Number Flow Governing Equations

By augmenting the low Mach number flow governing equations with the revised APE-1/4 equations (2.88), the resulting system of governing equations is able to account for the transport of all three types of characteristics. In this setup, the acoustic source terms (2.84) model the excitation of acoustic waves by the low Mach number flow field. In order to account for the acoustic flame interaction that causes thermoacoustic instabilities, the effects into the opposite direction must be modeled as well. However, these feedback mechanisms involve numerous physical processes that strongly depend on the considered configuration [28, 17, 81,

82]. Consequently, these interactions must be reflected by the mathematical model of the CFD, and may require an adjusted treatment of e.g. turbulence, mixing, combustion or boundary conditions. The correct description of acoustic flame interaction in time-resolved LES simulations is hence subject to ongoing research [61, 60, 67, 66] and beyond the scope of the current work. For this reason, the developed method is agnostic with regard to the implementation of the thermoacoustic feedback mechanism and facilitates the transfer of arbitrary quantities. Its architecture hence promotes the implementation of said feedback mechanisms.

To demonstrate the feasibility of the developed coupling layer, an acoustic pressure gradient as proposed by Klenke [66] is implemented. Its underlying concept is to superimpose the acoustic pressure on the low Mach number flow field. The perturbations alter the flow field and thereby incorporate the effect of the acoustic field into the low Mach number flow field [66]. The main advantages of the formulation are its independence from the chosen governing equations and that it only requires the transfer of the acoustic pressure p^a . The latter is introduced into the momentum equation via an additional, acoustic pressure gradient $\partial p^a / \partial x_j$:

$$\begin{aligned} \frac{\partial \bar{\rho} \tilde{u}_j}{\partial t} + \frac{\partial \bar{\rho} \tilde{u}_i \tilde{u}_j}{\partial x_i} = \\ - \frac{\partial \bar{p}^{\text{mod}}}{\partial x_j} + \frac{\partial}{\partial x_i} \left(\bar{\mu} \left(\frac{\partial \tilde{u}_i}{\partial x_j} + \frac{\partial \tilde{u}_j}{\partial x_i} \right) - \frac{2}{3} \bar{\mu} \frac{\partial \tilde{u}_m}{\partial x_m} \delta_{ij} - \bar{\rho} \tau_{ij}^{\text{sgs},u} \right) - \frac{\partial p^a}{\partial x_j}. \end{aligned} \quad (2.92)$$

3 Numerical Implementation of the Acoustics Solver

In the previous chapter, a mathematical model was established, that describes the physical processes investigated throughout this work. The model involves two sets of partial differential equations, the low Mach number, Favre-averaged governing equations (2.79) and the Acoustic Perturbation Equations (2.88). Both systems constitute a continuous problem, where for every quantity, a value is defined at every point inside the computational domain. In order to solve the governing equations numerically, the continuous systems have to be approximated with a finite number of values [116], e.g. in specific locations via a numerical mesh or by means of polynomial coefficients. This process, referred to as *discretization*, yields an algebraic equation system, that can be solved, to obtain a numerical solution to the original mathematical model. During this process, three major error sources arise. The *modeling error* refers to deviations of the mathematical model from the actual physical phenomena, e.g. due to inadequate assumptions and simplifications. The discretization introduces a *discretization error*, caused by the approximation of the continuous problem by a finite set of values. Finally, the solution of the algebraic equation system is usually approximated as well, which amounts to the *solution error* [116].

In the current implementation, the acoustic wave propagation is modeled in time domain, which allows for an efficient description over a wide frequency range. Relative to their time and length scales, very long integration times and distances are common in CAA simulations, so that even small discretization errors can accumulate over time and spoil the solution or lead to instabilities. This problem is aggravated by the lack of a diffusive term in the APE, which usually dampens the spurious waves, related to discretization errors. Accordingly, a low discretization error is essential for computational acoustics solvers. As laid out in section 3.6.2, the error can either be minimized by increasing the resolution of the spatial discretization, or by using a higher order discretization scheme. The first option corresponds to a linear growth of the computational cost, while for the latter, the increase is much slower. Accordingly, high order methods are usually preferred for CAA applications, due to their improved numerical efficiency.

The aim of the developed method is to account for wave propagation in complex geometries of technical combustion systems, which is difficult with most tra-

ditional high order discretization schemes. A class of methods, which qualifies for complex geometries, while providing a high discretization order, are the discontinuous Galerkin schemes [24]. They divide the computational domain into non-overlapping elements of different sizes and shapes. For each element, a spectral discretization in terms of local polynomials is performed, which determine the convergence order of the scheme. Due to the element-wise discretization, the method is easily applicable to mixed, unstructured meshes, which vastly simplifies the discretization of complex geometries. The majority of DG schemes is encompassed by the spectral/hp element method [62], which includes nodal and modal expansion bases and is independent of continuous or discontinuous projections. By allowing for arbitrary numbers of elements and polynomial orders at the same time, the method bridges the gap between high order finite element, and low order spectral methods. For the current work, the Nektar++ framework [19] was used, which provides a robust and efficient implementation of the spectral/hp element method. Due to its open source license, the developed solver is contributed to the Nektar++ project and made available to the scientific community.

This chapter is dedicated to the implementation of the novel CAA solver. To this end, the relevant concepts of the spectral/hp element method and the discontinuous Galerkin formulation are revisited first. If not stated otherwise, these descriptions are based on Karniadakis and Sherwin [62], which is also the foundation of Nektar++ and thereby the current implementation. Subsequently, the implemented Riemann solvers and boundary conditions are discussed, where special focus is put on variable density base flows. The temporal discretization scheme is briefly reviewed, before an overview of the complete solution algorithm is given. Since this work constitutes the first application of the novel CAA solver, the chapter closes with a verification of its implementation and an assessment of its numerical error.

3.1 Spectral/hp Element Method

In the following, the general spectral/hp element method is laid out, based on a hyperbolic *Partial Differential Equation* (PDE), defined over a domain Ω :

$$\mathbb{G}(q) = \frac{\partial q}{\partial t} + \nabla \cdot \mathbf{F} = 0. \quad (3.1)$$

Its solution $q = q(\mathbf{x}, t)$ can be approximated by a weighted sum of N_{DOF} trial or *expansion functions* Φ_i :

$$q^\delta(\mathbf{x}, t) = \sum_{i=0}^{N_{\text{DOF}}-1} \tilde{q}_i(t) \Phi_i(\mathbf{x}). \quad (3.2)$$

Here, the coefficients $\check{q}_i(t)$ amount to a spectral discretization in terms of the trial-functions $\Phi_i(\mathbf{x})$, similar to the coefficients of the Fourier transform. Since q^δ only approximates the solution, it does not satisfy the partial differential equation (3.1), which gives rise to a residual $R(q^\delta)$:

$$\mathbb{G}(q^\delta) = R(q^\delta) \neq 0. \quad (3.3)$$

In order to obtain an approximate solution, the original problem $\mathbb{G}(q) = 0$ is weakened, so that the residuals are only required to vanish in terms of a set of test or *weighting functions* $v_j(\mathbf{x})$. The resulting projection is accordingly referred to as the *weak form* of the PDE:

$$\int_{\Omega} v_j(\mathbf{x}) \mathbb{G}(q^\delta) d\Omega \stackrel{!}{=} 0 \quad \text{with } j \in \{1, \dots, N_{\text{DOF}}\}. \quad (3.4)$$

By introducing the inner product

$$(a, b)_{\Omega} := \int_{\Omega} a b d\Omega, \quad (3.5)$$

the weak form is written as

$$(v_j(\mathbf{x}), \mathbb{G}(q^\delta))_{\Omega} \stackrel{!}{=} 0 \quad \text{with } j \in \{1, \dots, N_{\text{DOF}}\}. \quad (3.6)$$

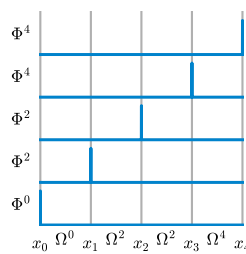
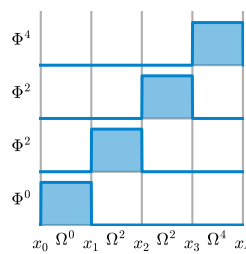
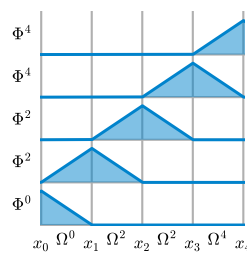
The weak form is also inherent to different other spatial discretization techniques, depending on the choice of weighting functions. Examples are given in Tab. 3.1, where the FDM is based on a number of Dirac functions and in the element-wise description of the FVM scheme, a piecewise defined, constant weighting function is implied. The finite element method is a subclass of the spectral/hp element method, since in both cases the expansion functions Φ serve as weights:

$$v_j = \Phi_j, \quad (3.7)$$

which gives the *Galerkin Projection*

$$(\Phi_j(\mathbf{x}), \mathbb{G}(q^\delta))_{\Omega} \stackrel{!}{=} 0 \quad \text{with } j \in \{1, \dots, N_{\text{DOF}}\}. \quad (3.8)$$

Table 3.1: Different choices of weighting functions $v_j(\mathbf{x})$ and their corresponding projections.

Collocation (Finite Differences)	Subdomain (Finite Volumes)	Galerkin (Finite and Spectral/hp Element Method)
$v_j(x) = \delta(x - x_j)$ 	$v_j(x) = \begin{cases} 1 & : \text{inside } \Omega^e \\ 0 & : \text{outside } \Omega^e \end{cases}$ 	$v_j(x) = \Phi_j$ 

3.1.1 h -type Extension

The expansion (3.2) uses polynomials $\Phi_i(\mathbf{x})$ which are defined in the entire computational domain Ω . While this resembles classical spectral methods, it aggravates handling of complex geometries. Consequently, the domain is split into N_{el} non-overlapping elements Ω_e :

$$\Omega = \bigcup_{e=1}^{N_{\text{el}}} \Omega_e \quad \text{and} \quad \bigcap_{e=1}^{N_{\text{el}}} \Omega_e = \{\}. \quad (3.9)$$

The N_{DOF} global expansion functions Φ_i are replaced by $P = N_{\text{DOF}}/N_{\text{el}}$ element-wise modes Φ_p^e :

$$q^\delta(\mathbf{x}, t) = \sum_{e=1}^{N_{\text{el}}} \sum_{p=0}^P \tilde{q}_p^e \Phi_p^e(\mathbf{x}) \quad (3.10)$$

Since each element is of arbitrary shape, the formulation is further simplified by introducing a standard element Ω_{st} with the local coordinate ξ :

$$\Omega_{\text{st}} = \{-1 \leq \xi_i \leq 1\}. \quad (3.11)$$

In local coordinates, the global modes $\Phi_i(\mathbf{x})$ are replaced with corresponding local expansion modes $\phi_p(\xi)$. At this, the transformation

$$\mathbf{x} = \phi_0(\xi)x_{e-1} + \phi_1(\xi)x_e \quad \text{with} \quad \xi \in \Omega_{\text{st}} \quad (3.12)$$

maps the local coordinate ξ to the global coordinate \mathbf{x} , by expressing it in terms of local expansion functions, referred to as *parametric mapping*. Within the spectral/hp element method, the approximate solution q^δ can be represented either as global, element-wise or local expansion:

$$q^\delta(\mathbf{x}, t) = \underbrace{\sum_{i=0}^{N_{\text{DOF}}-1} \tilde{q}_i(t) \Phi_i(\mathbf{x})}_{\text{Global Expansion}} = \underbrace{\sum_{e=1}^{N_{\text{el}}} \sum_{p=0}^P \tilde{q}_p^e(t) \Phi_p^e(\mathbf{x})}_{\text{Element-wise Expansion}} = \underbrace{\sum_{e=1}^{N_{\text{el}}} \sum_{p=0}^P \tilde{q}_p^e(t) \phi_p(\xi)}_{\text{Local Expansion}}. \quad (3.13)$$

The applicability to an arbitrary number of elements N_{el} with size h marks the h -type extension of the spectral method.

3.1.2 p -type Extension

While the h -type extension allows for adjusting the accuracy of the spatial discretization by changing the number of elements, the p -type extension refers to a variable number of expansion functions P . It is therefore characterized by an adjustable discretization accuracy in spectral domain. To maximize the efficiency of a given expansion, every mode should account for information, which ideally does not overlap with the other modes. This concept is formalized as linear independence or orthogonality.

Common expansions are either modal or nodal. Nodal expansions are composed of the Lagrange polynomials $\ell_p(x)$

$$\ell_p(x) = \frac{\prod_{q=0, q \neq p}^P (x - x_q)}{\prod_{q=0, q \neq p}^P (x_p - x_q)}, \quad (3.14)$$

which have a unit value at their nodal point x_p and are zero at the other polynomials nodal points x_q , i.e. $\ell_p(x_q) = \delta_{pq}$. Therefore, when using Lagrange polynomials

as expansion functions, the coefficients \check{q}_p take the value of the approximate solution $q^\delta(x_q)$ at these points.

Modal expansion bases, in contrast to nodal ones, are hierarchical, meaning an expansion of order P is contained within the expansion of order $P + 1$. This causes the modal bases to be orthogonal by definition, providing an increased numerical efficiency compared to nodal expansions. For this reason, the following description is limited to modal expansions, which were exclusively used in this work. A detailed discussion of nodal expansions can be found in [62].

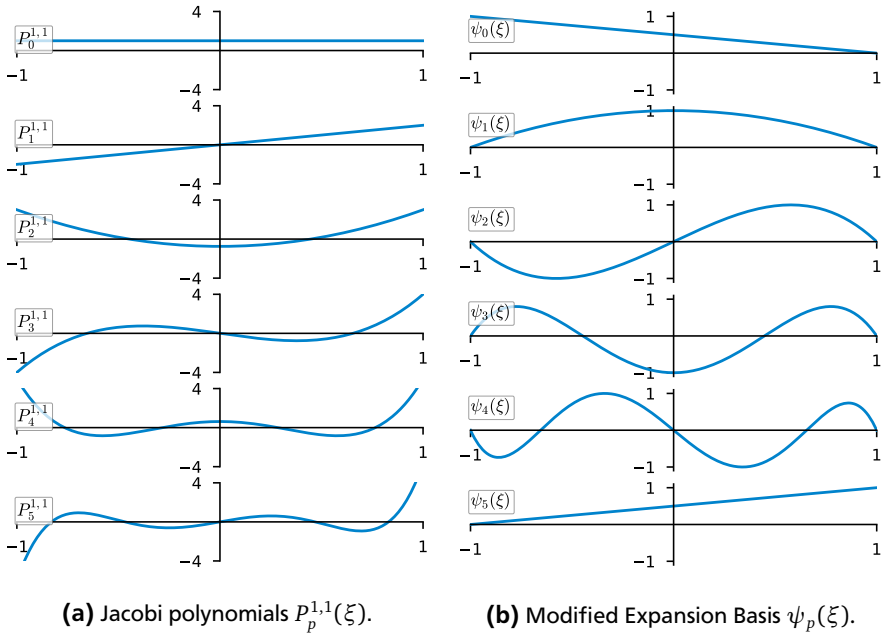


Figure 3.1: One-dimensional modal expansion bases with a polynomial order of $P = 5$

The favorable properties of the modal expansions are due the Jacobi polynomials $P_p^{\alpha,\beta}(x)$, they are constructed from. The Jacobi polynomials represent the solution to a singular Sturm-Liouville problem in the region $-1 < x < 1$ [62]. For $\alpha = \beta = 0$, the Jacobi polynomials give the Legendre polynomials and for $\alpha = \beta = -1/2$, the Chebyshev polynomials are obtained. As evident from the first six polynomials $P_0^{1,1}$ to $P_5^{1,1}$, shown in Fig. 3.1a, their boundary values at $\xi = -1$ and $\xi = 1$ are non-zero. If used as expansion function, this causes every polynomial to contribute to

the boundary values of the element, which complicates the inter-element coupling in combination with the h -type decomposition.

To limit the boundary value contribution to only a single mode, a boundary or interior decomposition is performed, that requires all but the first polynomial ($p = 0$) to vanish at $\xi = -1$ and all but the last polynomial ($p = P$) to vanish at $\xi = 1$. To this end, linear functions are used as first and last modes of the expansion and the Jacobi polynomials are scaled with a quadratic function. The resulting *modified expansion basis* $\psi_p(\xi)$ satisfies the boundary decomposition:

$$\phi_p(\xi) = \psi_p(\xi) = \begin{cases} \frac{1-\xi}{2} & : p = 0 \\ \left(\frac{1-\xi}{2}\right)\left(\frac{1+\xi}{2}\right)P_{p-1}^{1,1}(\xi) & : 1 \leq p \leq P-1 \\ \frac{1+\xi}{2} & : p = P \end{cases} \quad (3.15)$$

It is depicted in Fig. 3.1b. A caveat of this technique is a loss of orthogonality as consequence of the linear functions, which is, however, compensated by a more efficient implementation and the possibility to perform matrix-level optimizations such as static condensation [62].

Multi-Dimensional Expansion Basis

In three dimensions, a hexahedral standard element Ω_{st} with the cartesian coordinates (ξ_1, ξ_2, ξ_3) is described as:

$$\Omega_{\text{st}} = \{-1 \leq \xi_1, \xi_2, \xi_3 \leq 1\}. \quad (3.16)$$

Consequently, a local, three-dimensional expansion basis is constructed by multiplication of the one-dimensional expansions in the respective direction:

$$\phi_{pqr} = \phi_p(\xi_1) \phi_q(\xi_2) \phi_r(\xi_3) \text{ with } 0 \leq p \leq P_1 \wedge 0 \leq q \leq P_2 \wedge 0 \leq r \leq P_3. \quad (3.17)$$

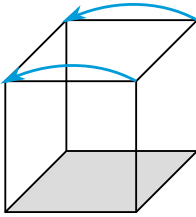
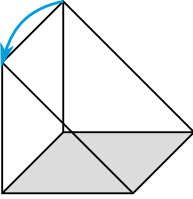
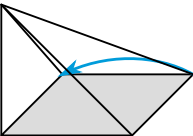
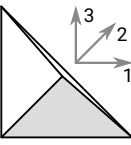
In each direction i , the bases comprise P_i modes. It follows from this notation that ϕ_{pqr} can be interpreted as tensor and is therefore referred to as *tensorial expansion basis*. The corresponding three-dimensional expansion within this standard element is:

$$q^\delta(\xi_1, \xi_2, \xi_3) = \sum_{p=0}^{P_1} \sum_{q=0}^{P_2} \sum_{r=0}^{P_3} \check{q}_{pqr}^e \phi_{pqr}^e(\xi_1, \xi_2, \xi_3),$$

or short:

$$q^\delta(\xi_1, \xi_2, \xi_3) = \sum_{pqr}^{P_{123}} \check{q}_{pqr}^e \phi_{pqr}^e(\xi_1, \xi_2, \xi_3). \quad (3.18)$$

Table 3.2: Upper bounds in cartesian and collapsed coordinates for different three-dimensional element types. In both systems, the lower bound is -1 for all coordinates. The blue arrows indicate which edges are collapsed in order to obtain the element type below.

Type	Cartesian Upper Bounds	Transform	Collapsed Upper Bounds
Hexahedron	$\xi_1 \leq 1$ $\xi_2 \leq 1$ $\xi_3 \leq 1$		$\eta_1 = \xi_1$ $\eta_2 = \xi_2$ $\eta_3 = \xi_3$
Prism	$\xi_1 \leq 1$ $\xi_2 + \xi_3 \leq 0$		$\eta_1 = \frac{2(1+\xi_1)}{1-\xi_3} - 1$ $\eta_2 = \xi_2$ $\eta_3 = \xi_3$
Pyramid	$\xi_1 + \xi_2 \leq 0$ $\xi_2 + \xi_3 \leq 0$		$\eta_1 = \frac{2(1+\xi_1)}{1-\xi_3} - 1$ $\eta_2 = \frac{2(1+\xi_2)}{1-\xi_3} - 1$ $\eta_3 = \xi_3$
Tetrahedron	$\xi_1 + \xi_2 + \xi_3 \leq -1$		$\eta_1 = \frac{2(1+\xi_1)}{-\xi_2-\xi_3} - 1$ $\eta_2 = \frac{2(1+\xi_2)}{1-\xi_3} - 1$ $\eta_3 = \xi_3$

While this formulation is sufficient for one-dimensional, quadrilateral and hexahedral elements, the bounds of the cartesian coordinates (ξ_i) are interdependent for other element types. For e.g. a tetrahedron these are

$$\Omega_{\text{st,tet}} = \{-1 \leq \xi_1, \xi_2, \xi_3 \wedge \xi_1 + \xi_2 + \xi_3 \leq -1\}. \quad (3.19)$$

For a suitable tensorial basis that is valid on all element types, a universal, collapsed coordinate system η_i with independent bounds is required:

$$\Omega_{\text{st}} = \{-1 \leq \eta_1, \eta_2, \eta_3 \leq 1\}. \quad (3.20)$$

For three-dimensional elements, these coordinates are obtained by introducing a coordinate transform that collapses one or more edges, as shown in Tab. 3.2. With the lower bounds constant at $-1 \leq \eta_i$, the transformation from cartesian to collapsed coordinates is given by the respective collapsed coordinate's upper bounds.

While true in one dimension, using the $P_p^{1,1}$ Jacobi polynomials in multiple dimensions does not necessarily yield an orthogonal tensorial expansion basis. Instead, the multi-dimensional basis is constructed from a set of different Jacobi polynomials, referred to as *principle functions* ψ_p^a , ψ_{pq}^b and ψ_{pqr}^c . A more detailed discussion of these functions is given in [123]. Accordingly, the three-dimensional, tensorial, modified expansion bases for different element types are composed as:

$$\text{Hexahedron: } \phi_{pqr}(\xi_1, \xi_2, \xi_3) = \psi_p^a(\xi_1) \psi_q^a(\xi_2) \psi_r^a(\xi_3)$$

$$\text{Prism: } \phi_{pqr}(\xi_1, \xi_2, \xi_3) = \psi_p^a(\eta_1) \psi_q^a(\xi_2) \psi_{pr}^b(\xi_3)$$

$$\text{Pyramid: } \phi_{pqr}(\xi_1, \xi_2, \xi_3) = \psi_p^a(\eta_1) \psi_q^a(\eta_2) \psi_{pqr}^c(\xi_3)$$

$$\text{Tetrahedron: } \phi_{pqr}(\xi_1, \xi_2, \xi_3) = \psi_p^a(\eta_1) \psi_{pq}^b(\eta_2) \psi_{pqr}^c(\eta_3).$$

Due to the transformation to collapsed coordinates, using principal functions of the same degree for all three directions leads to an excessive resolution near the collapsed edges. Consequently, the numerical efficiency is restored by gradually decreasing the number of modes closer to a collapsed edge [123, 62]. To this end, for each, three-dimensional mode, the degrees of the principal functions are limited based on the element type and location within the element as [62]:

$$\text{Hexahedron: } 0 \leq p, q, r \wedge p \leq P_1 \wedge q \leq P_2 \wedge r \leq P_3$$

$$\text{Prism: } 0 \leq p, q, r \wedge p \leq P_1 \wedge q \leq P_2 \wedge p + r \leq P_3 \wedge P_1 \leq P_3$$

$$\text{Pyramid: } 0 \leq p, q, r \wedge p \leq P_1 \wedge q \leq P_2 \wedge p + q + r \leq P_3 \wedge P_1, P_2 \leq P_3$$

$$\text{Tetrahedron: } 0 \leq p, q, r \wedge p \leq P_1 \wedge p + q \leq P_2 \wedge p + q + r \leq P_3 \wedge P_1 \leq P_2 \leq P_3.$$

3.1.3 Integration

By virtue of the p -extension, the spatial discretization can be chosen arbitrarily. In the spectral/hp element method, this also holds for the implementation of the integration and differentiation operators. Integration is achieved by using Gaussian Quadrature, which approximates an integral over a domain from individual values at distinct locations. These values can be evaluated from the expansion in any point of the element, allowing for a programmatic implementation of the Gaussian quadrature at arbitrary order. As consequence of the weak formulation (3.6), only the integral form of a PDE is required, so that each term of the PDE only needs to be evaluated at the quadrature points of the integration. This is exploited in the implementation of the differentiation operator, which is based on a representation in terms of Lagrange polynomials through the quadrature points. The advantage of this differentiation in physical space is that no transformation into modal space is required.

Integration in 1D

Any smooth, one-dimensional polynomial $q(x_1)$ of order P is representable in terms of Lagrange polynomials ℓ_i through Q nodes ξ_{1i} :

$$q(\xi_1) \approx \sum_{i=0}^{Q-1} q(\xi_{1i}) \ell_i(\xi_1). \quad (3.21)$$

The integral over a standard element can now be approximated from a finite summation:

$$\int_{\Omega_{st}} q(\xi_1) d\xi_1 \approx \sum_{i=0}^{Q-1} w_i q(\xi_{1i}), \quad (3.22)$$

using the *quadrature weights*:

$$w_i = \int_{\Omega_{st}} \ell_i(\xi_1) d\xi_1. \quad (3.23)$$

The above integral is referred to as Legendre integration and is exact for all polynomials $q(\xi_1)$ of order $P \leq Q - 1$. However, by using a specific distribution of nodes ξ_{1i} , this limit can be extended to facilitate accurate integration of higher order polynomials. This insight is fundamental to the *Gauss quadrature*, which computes the node locations, referred to as *quadrature points*, from the zeros of a Jacobi polynomial [62]. There are three types of Gauss quadratures. The original

Gauss quadrature uses only points interior to the interval $-1 < \xi_i < 1$, the Gauss-Radau quadrature includes one point on the interval edge and the Gauss-Lobatto quadrature includes both edge points, $\xi_1 = \pm 1$. For instance, the Gauss-Lobatto-Legendre quadrature exactly integrates a polynomial $q(\xi_1)$ of order P using at least $Q_{\min} \geq \frac{P+3}{2}$ quadrature points.

While sufficient for a single polynomial, integration of products of polynomials requires a larger number of quadrature points, as the multiplication increases the order to $2P$. With insufficient quadrature points, the expansion can not account for the small length scale features of the physical representation and aliasing errors occur, causing to the simulation to eventually become unstable. This is of particular importance for acoustics simulations, which typically involve governing equations that lack a stabilizing diffusion term.

Integration in 3D

The approximation (3.22) is trivially extended to multiple dimensions by a nested summation:

$$\int_{\Omega_{\text{st}}} q(\xi_1, \xi_2, \xi_3) d\xi_1 d\xi_2 d\xi_3 \approx \sum_{i=0}^{Q_1-1} \sum_{j=0}^{Q_2-1} \sum_{k=0}^{Q_3-1} w_i w_j w_k q(\xi_{1i}, \xi_{2j}, \xi_{3k}). \quad (3.24)$$

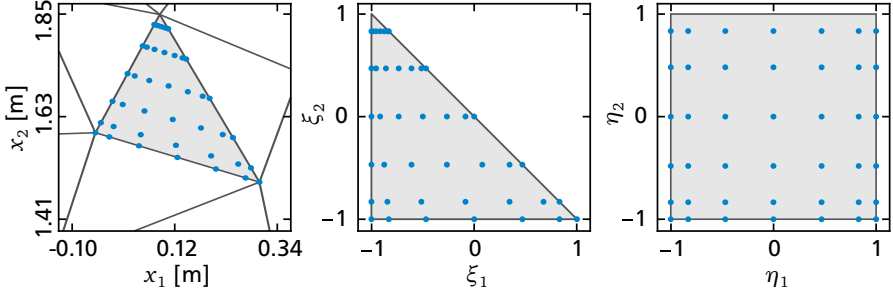
For quadrilateral and hexahedral elements, this expression is already sufficient. In other element types, the integration has to be performed in the previously introduced collapsed coordinate system (η_1, η_2, η_3) :

$$\int_{\Omega_{\text{st}}} q(\xi_1, \xi_2, \xi_3) d\xi_1 d\xi_2 d\xi_3 = \iiint_{-1}^1 q(\eta_1, \eta_2, \eta_3) \mathbf{J}_\eta d\eta_1 d\eta_2 d\eta_3, \quad (3.25)$$

where the transformation gives rise to a jacobian

$$\mathbf{J}_\eta = \frac{\partial(\xi_1, \xi_2, \xi_3)}{\partial(\eta_1, \eta_2, \eta_3)}. \quad (3.26)$$

For most element types, the jacobian is rather simple and can be accounted for by using appropriate Gauss-Jacobi integration weights, which introduce an additional term in the integral (3.22). This term recovers the jacobian \mathbf{J}_η for the given element type. The resulting integration methods are accordingly referred to as Gauss-Jacobi, Gauss-Radau-Jacobi and Gauss-Lobatto-Jacobi. An exemplary point distribution using this technique is shown in Fig. 3.2 for a triangle element.



(a) Element Ω_e in global coordinates. (b) Element Ω_{st} in local coordinates. (c) Element Ω_{st} in collapsed coordinates.

Figure 3.2: Representation of a triangular element in (a) global coordinates (x_1, x_2) , (b) local coordinates (ξ_1, ξ_2) and (c) in collapsed coordinates (η_1, η_2) . Quadrature points in blue. $Q = 7$ points with Gauss-Lobatto-Jacobi ($\alpha = \beta = 0$) distribution in ξ_1 -direction and $Q = 6$ Gauss-Radau-Jacobi ($\alpha = 1, \beta = 0$) distributed points in ξ_2 -direction.

Just like the transformation from standard to collapsed coordinates, the transformation from an arbitrary element Ω_e to the standard element Ω_{st} introduces a second jacobian:

$$\int_{\Omega_e} q(x_1, x_2, x_3) dx_1 dx_2 dx_3 = \int_{\Omega_{st}} q(\xi_1, \xi_2, \xi_3) |J_\xi| d\xi_1 d\xi_2 d\xi_3, \quad (3.27)$$

where:

$$|J_\xi| = \left| \frac{\partial x_i}{\partial \xi_j} \right|. \quad (3.28)$$

However, this quantity is too complex to be treated implicitly by using an appropriate point distribution and must be computed from the parametric mapping (3.12).

3.1.4 Differentiation

The spectral discretization of the p -extension allows for differentiation in modal space and in physical space. With the latter approach, a polynomial q that is to be differentiated is only required in physical space. This vastly simplifies the evaluation of complex flux functions or source terms and makes a prior transformation to modal space expendable.

As previously established, a smooth, one-dimensional polynomial $q(x_1)$ of order P is exactly representable in terms of Lagrange polynomials ℓ_p of P -th order:

$$q(\xi_1) \approx \sum_{p=0}^P q(\xi_{1p}) \ell_p(\xi_1). \quad (3.29)$$

Just like the integrals, the differentials are approximated as summation

$$\frac{\partial q}{\partial \xi_1}(\xi_1) \approx \sum_{p=0}^P q(\xi_{1p}) \frac{\partial \ell_p}{\partial \xi_1}(\xi_1). \quad (3.30)$$

For the Gaussian quadrature, which is applied to all terms of the PDE, only values at the quadrature points ξ_{1i} are required. It is therefore sufficient to evaluate the above summation at ξ_{1i} only:

$$\frac{\partial q}{\partial \xi_1}(\xi_{1i}) = \sum_{p=0}^P q(\xi_{1p}) \left. \frac{\partial \ell_p(\xi_1)}{\partial \xi_1} \right|_{\xi_{1i}}. \quad (3.31)$$

Again, this is trivially extended to three dimensions by a nested summation at the quadrature points $(\xi_{1i}, \xi_{2j}, \xi_{3k})$:

$$\frac{\partial q}{\partial \xi_1}(\xi_{1i}, \xi_{2j}, \xi_{3k}) = \sum_{p=0}^{P_1} \sum_{q=0}^{P_2} \sum_{r=0}^{P_3} q(\xi_{1p}, \xi_{2q}, \xi_{3r}) \left. \frac{\partial \ell_p(\xi_1)}{\partial \xi_1} \right|_{\xi_{1i}} \ell_q(\xi_{2j}) \ell_r(\xi_{3k}). \quad (3.32)$$

By definition (3.14), each Lagrange polynomial is unity at its node and zero at all other nodes, i.e. $\ell_q(\xi_{2j}) = \delta_{qj}$ and $\ell_r(\xi_{3k}) = \delta_{rk}$. Substitution in (3.32) gives:

$$\frac{\partial q}{\partial \xi_1}(\xi_{1i}, \xi_{2j}, \xi_{3k}) = \sum_{p=0}^{P_1} q(\xi_{1p}, \xi_{2j}, \xi_{3k}) \left. \frac{\partial \ell_p(\xi_1)}{\partial \xi_1} \right|_{\xi_{1i}}. \quad (3.33)$$

The derivatives in the other directions, $\partial/\partial \xi_2$ and $\partial/\partial \xi_3$ are defined accordingly.

In collapsed coordinates, the derivative in standard coordinates is given by the chain rule:

$$\frac{\partial}{\partial \xi_1} = \frac{\partial \eta_1}{\partial \xi_1} \frac{\partial}{\partial \eta_1} + \frac{\partial \eta_2}{\partial \xi_1} \frac{\partial}{\partial \eta_2} + \frac{\partial \eta_3}{\partial \xi_1} \frac{\partial}{\partial \eta_3}, \quad (3.34)$$

and the differential operator takes the form:

$$\frac{\partial q}{\partial \eta_1}(\eta_{1i}, \eta_{2j}, \eta_{3k}) = \sum_{p=0}^{P_1} q(\eta_{1p}, \eta_{2j}, \eta_{3k}) \left. \frac{\partial \ell_p(\eta_1)}{\partial \eta_1} \right|_{\eta_{1i}}. \quad (3.35)$$

With the above expression, the derivative of a polynomial q is computed by multiplication with the derivative of the Lagrange polynomials at the quadrature points with regard to the collapsed coordinates. The latter are problem-independent and, just like the quadrature weights w_i , can be tabulated or precomputed at runtime. The derivatives $\partial\eta/\partial\xi$ are treated in the same way. The derivatives of the parametric mapping, which arise from the transformation to an arbitrary element Ω_e :

$$\frac{\partial}{\partial x_1} = \frac{\partial \xi_1}{\partial x_1} \frac{\partial}{\partial \xi_1} + \frac{\partial \xi_2}{\partial x_1} \frac{\partial}{\partial \xi_2} + \frac{\partial \xi_3}{\partial x_1} \frac{\partial}{\partial \xi_3}, \quad (3.36)$$

must be computed at run-time from Eq. (3.12), just like the jacobian J_ξ of the integration operator.

3.1.5 Forward- and Backward Transform

With the spectral/hp element method, each field q can be represented in terms of the expansion coefficients \check{q}_p^e or in terms of physical values at a sufficient number of quadrature points $q(\xi_{1i}, \xi_{2j}, \xi_{3k})$. Both representations are useful for different operations, e.g. the fluxes are easily evaluated, differentiated and integrated at the quadrature points in physical space, while the inversion of the elemental mass matrix is more efficient in modal space. The process of determining the expansion coefficients \check{q} for a given function $q(\mathbf{x})$ is commonly referred to as *forward transformation*. Accordingly, the term *backward transformation* denotes the inverse operation, where the function is retrieved by simply evaluating the expansion (3.13).

The forward transform inside the standard element can be formalized as:

$$\sum_{pqr}^{P_{123}} \phi_{pqr} \check{q}_{pqr}^e = q(\xi) + R(q), \quad (3.37)$$

where the function q can not be fully represented by the expansion basis, leading to a residual $R(q)$. In accordance with the spectral/hp element method, the residual is required to vanish in the weak form of the forward transform:

$$\begin{aligned} \left(\phi_{stu}, \sum_{pqr}^{P_{123}} \phi_{pqr} \check{q}_{pqr}^e \right)_{\Omega_e} &\stackrel{!}{=} (\phi_{stu}, q(\xi))_{\Omega_e} \\ \Leftrightarrow \sum_{pqr}^{P_{123}} (\phi_{stu}, \phi_{pqr})_{\Omega_e} \check{q}_{pqr}^e &\stackrel{!}{=} (\phi_{stu}, q(\xi))_{\Omega_e} \end{aligned} \quad (3.38)$$

for every weighting function ϕ_{stu} with $s, t, u \in \{0, \dots, P_{1,2,3}\}$. The integrals in the inner products are computed from discrete values using the Gauss quadrature. For the right hand side, this gives:

$$(\phi_{stu}, q(\xi))_{\Omega_e} \approx \sum_{ijk}^{Q_{123}-1} w_{ijk} \phi_{stu}(\xi_{ijk}) q(\xi_{ijk}) |J_{ijk}|. \quad (3.39)$$

This integration is only exact if $q(\xi)$ lies within the polynomial space of the expansion, which usually is not the case. The error related to this integration decreases for smoother functions q and a higher numbers of quadrature points Q . In order to not dominate the transform, the error must be of less or equal order as the approximation error $R(q)$ [62]. Using the orderings

$$\begin{aligned} n(pqr) &= r + q(P_2 + 1) + p(P_2 + 1)(P_3 + 1) \\ m(ijk) &= i + jQ_1 + kQ_1Q_2, \end{aligned} \quad (3.40)$$

the right hand side of the forward transform can be written as first order tensor with $P_1P_2P_3$ elements:

$$K^e q^e = w_{ijk} \phi_{stu}(\xi_{ijk}) q(\xi_{ijk}) |J_{ijk}| \quad (3.41)$$

where

$$K_{n(stu)m(ijk)}^e = w_{ijk} \phi_{stu}(\xi_{ijk}) |J_{ijk}| \quad (3.42)$$

$$q_{m(ijk)}^e = q(\xi_{ijk}). \quad (3.43)$$

The left hand side is treated similarly and reordered to yield

$$M^e \check{q}^e = \sum_{pqr}^{P_{123}} \sum_{ijk}^{Q_{123}-1} w_{ijk} \phi_{stu}(\xi_{ijk}) \phi_{pqr}(\xi_{ijk}) |J_{ijk}| \check{q}_{pqr}^e \quad (3.44)$$

with $s, t, u \in \{0, \dots, P_{1,2,3}\}$. In matrix form, this gives the elemental mass matrix $M^e = (\phi_{stu}, \phi_{pqr})_{\Omega_e}$ and the coefficient vector \check{q}^e ,

$$M_{n(stu)n(pqr)}^e = \sum_{ijk}^{Q_{123}-1} w_{ijk} \phi_{stu}(\xi_{ijk}) \phi_{pqr}(\xi_{ijk}) |J_{ijk}| \quad (3.45)$$

$$\check{q}_{n(pqr)}^e = \check{q}_{pqr}^e. \quad (3.46)$$

Using Gaussian quadrature, the forward transform (3.38) reads in matrix form :

$$\begin{aligned} \mathbf{M}^e \tilde{\mathbf{q}}^e &= \mathbf{K}^e \mathbf{q}^e \\ \Leftrightarrow \tilde{\mathbf{q}}^e &= (\mathbf{M}^e)^{-1} \mathbf{K}^e \mathbf{q}^e . \end{aligned} \quad (3.47)$$

Unlike the backward transform, the forward transform requires the inversion of the mass matrix \mathbf{M}^e , which entails significant computational cost.

When using a continuous Galerkin projection, continuity between each element is enforced. Consequently, the above operation cannot be performed on each element independently, but instead of the elemental mass matrix \mathbf{M}^e a global matrix \mathbf{M} must be inverted. \mathbf{M} is constructed from all elemental mass matrices by imposing equal values at the edge quadrature points of adjacent elements. This process also yields the global equivalents of the elemental vectors \mathbf{q}^e , $\tilde{\mathbf{q}}^e$ and matrix \mathbf{K}^e . The global mass matrix is symmetrical, but only partially banded and of rank N_{DOF} , making its inversion considerably more computationally expensive than for a discontinuous projection.

Using the reordering, the backward transformation (3.13) can similarly be written as matrix operation:

$$\mathbf{q}^e = \mathbf{B}^e \tilde{\mathbf{q}}^e \quad (3.48)$$

with the basis matrix

$$\mathbf{B}_{m(ijk)n(pqr)}^e = \phi_{pqr}(\xi_{ijk}) . \quad (3.49)$$

Its global equivalent \mathbf{B} is constructed consistently with the global mass matrix \mathbf{M} .

3.2 Discontinuous Galerkin Formulation

The spectral/hp element method described in section 3.1 qualifies for the spatial discretization of arbitrary partial differential equations while being independent of the projection and the element coupling. It is commonly used in conjunction with continuous and discontinuous projections. Throughout this work, a continuous projection is used for the intermediate expansion in chapter 5, while a discontinuous projection is applied to all fields of the APE system. The latter technique permits discontinuities at the element interfaces, where inter-element coupling is accomplished via the introduction of a numerical flux through the element faces. The element-wise treatment has the advantage, that each element can be considered separately, which is the key to its relatively straightforward implementation and stability.

Revisiting the generic advection-type equation (3.1) inside a single element Ω_e

$$\frac{\partial q}{\partial t} + \nabla \cdot \mathbf{F}(q) = 0, \quad (3.50)$$

its weak form (3.6) is given as:

$$\int_{\Omega_e} \phi_{pqr} \frac{\partial q^\delta}{\partial t} + \int_{\Omega_e} \phi_{pqr} \nabla \cdot \mathbf{F}(q^\delta) d\Omega_e = 0 \quad (3.51)$$

with $p, q, r \in \{0, \dots, P_{1,2,3}\}$. Application of Gauss' theorem yields:

$$\int_{\Omega_e} \phi_{pqr} \frac{\partial q^\delta}{\partial t} d\Omega_e + \int_{\partial\Omega_e} \phi_{pqr} \mathbf{F}(q^\delta) \cdot \mathbf{n} d(\partial\Omega_e) - \int_{\Omega_e} \nabla \phi_{pqr} \cdot \mathbf{F}(q^\delta) d\Omega_e = 0. \quad (3.52)$$

By introducing a short notation for the integral of face-normal fluxes

$$\langle \mathbf{a}, \mathbf{b} \rangle_{\partial\Omega} = \int_{\Omega} \mathbf{a} \mathbf{b} \cdot \mathbf{n} d(\partial\Omega), \quad (3.53)$$

this simplifies to a formulation, which represents the foundation of the discontinuous Galerkin method:

$$\left(\phi_{pqr}, \frac{\partial q^\delta}{\partial t} \right)_{\Omega_e} + \langle \phi_{pqr}, \mathbf{F}(q^\delta) \rangle_{\partial\Omega_e} - (\nabla \phi_{pqr}, \mathbf{F}(q^\delta))_{\Omega_e} = 0. \quad (3.54)$$

In the above equation, the advection term was split into the fluxes across element faces and an inner-elemental contribution. While the latter can be computed using the differentiation and integration operators, the inter-element fluxes must be computed with a separate numerical technique. Accordingly, they are referred to as numerical fluxes $\mathbf{F}^R(q_L, q_R) = -\mathbf{F}^R(q_R, q_L)$, where q_L and q_R denote the internal and the external state, as shown in Fig. 3.3.

$$\left(\phi_{pqr}, \frac{\partial q^\delta}{\partial t} \right)_{\Omega_e} + \langle \phi_{pqr}, \mathbf{F}^R(q_L, q_R) \rangle_{\partial\Omega_e} - (\nabla \phi_{pqr}, \mathbf{F}(q^\delta))_{\Omega_e} = 0. \quad (3.55)$$

Using the reordering (3.40) and the matrix notation introduced in section 3.1.5, the advection equation is discretized as:

$$\frac{\partial \check{\mathbf{q}}^e}{\partial t} = (\mathbf{M}^e)^{-1} (\mathbf{b}^e - \mathbf{c}^e), \quad (3.56)$$

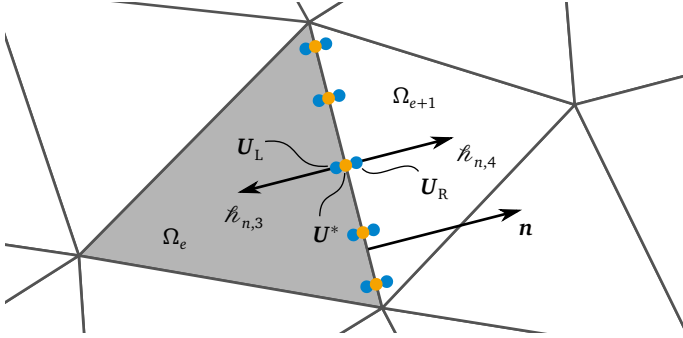


Figure 3.3: Direction and location of the relevant variables at the element interface for the APE under subsonic conditions for the element Ω_e (grey) and Ω_{e+1} . Left U_L and right hand side U_R states in blue, intermediate state U^* in yellow. All three states are located in the same points in space but are shown next to each other by way of illustration.

where the vector of internal \mathbf{b}^e and numerical fluxes \mathbf{c}^e are given as:

$$\mathbf{b}_{n(pqr)}^e = (\nabla \phi_{pqr}, \mathbf{F}(q^\delta))_{\Omega_e} \quad (3.57)$$

$$\mathbf{c}_{n(pqr)}^e = \langle \phi_{pqr}, \mathbf{F}^R(q_L, q_R) \rangle_{\partial \Omega_e} . \quad (3.58)$$

In this equation, the left hand side is given in terms of the expansion coefficients \tilde{q}^e , while the right hand side is computed exclusively from physical values q^e . Left-multiplication of the basis matrix \mathbf{B}^e yields an equivalent advection equation in physical values:

$$\frac{\partial \mathbf{q}^e}{\partial t} = \mathbf{B}^e (\mathbf{M}^e)^{-1} (\mathbf{b}^e - \mathbf{c}^e) \quad (3.59)$$

Since the integrals in the above equation are treated as described in section 3.1.3, only the fluxes at the quadrature points are required. The numerical fluxes must be computed at the element edges, but are undefined at the face edges, where more than two elements intersect and the face-normals are ambiguous. Accordingly, the numerical fluxes \mathbf{c}^e are evaluated at dedicated one/two-dimensional Gauss-Jacobi quadrature points on the face/edge, which exclude the edge points, as shown in Fig. 3.3. The gradient for the internal fluxes \mathbf{b}^e is evaluated as laid out in section 3.1.4.

The computation of the numerical fluxes \mathbf{c}^e poses a Riemann problem, to which a simple solution is only available for very few cases, where the diagonalized form

can be established. Examples of such governing equations are the scalar advection problem and the plane wave propagation described in section 2.4.3. When this diagonalization is not possible, the Riemann problem has to be solved iteratively or by approximation. Iterative Riemann solvers typically increase the computational cost substantially, which explains the large variety of approximate Riemann solvers available today [134]. Two solvers of the latter category are applied to the three-dimensional APE-equations (2.88) in the following.

3.2.1 Lax-Friedrichs and Local Lax-Friedrichs Flux

The simplest stable, first order Riemann solver is the Lax-Friedrichs scheme [134]:

$$\mathbf{F}^R(\mathbf{U}_L, \mathbf{U}_R) = \frac{1}{2} [\mathbf{F}(\mathbf{U}_L) + \mathbf{F}(\mathbf{U}_R)] - \frac{\Delta t}{2\Delta x} (\mathbf{U}_R - \mathbf{U}_L). \quad (3.60)$$

The scheme is stable for Courant numbers between 0 and 1 and of first order accuracy. The first term represents the naive averaging of the left and right hand side state fluxes, $\mathbf{F}(\mathbf{U}_L)$ and $\mathbf{F}(\mathbf{U}_R)$, respectively. Taken by itself, this would be unconditionally unstable and only works due to the second term, which introduces additional diffusion that stabilizes the scheme at the cost of accuracy.

Instead of adding the same level of diffusion throughout the entire domain, the *Local Lax-Friedrichs method* (LLF) [80, p. 233] uses a locally determined value $\|\mathbf{\Lambda}_n\|_{\max}$:

$$\mathbf{F}^R(\mathbf{U}_L, \mathbf{U}_R) = \frac{1}{2} [\mathbf{F}(\mathbf{U}_L) + \mathbf{F}(\mathbf{U}_R)] - \frac{1}{2} \|\mathbf{\Lambda}_n\|_{\max} (\mathbf{U}_R - \mathbf{U}_L), \quad (3.61)$$

where $\|\mathbf{\Lambda}_n\|_{\max}$ is the maximum absolute eigenvalue of the interface-normal projection of the governing equations, similar to Eq. (2.91). Due to the discontinuous projection, the base flow fields differ between the left- and right hand sides. This is unproblematic for the computation of the fluxes, since for $\mathbf{F}(\mathbf{U}_L)$, the left state values are used and $\mathbf{F}(\mathbf{U}_R)$ is computed using the right hand side values. For $\|\mathbf{\Lambda}_n\|_{\max}$, however, a value that applies to the left and right side simultaneously must be found. As discussed above, the scheme becomes unstable for insufficient artificial diffusion. Excessive values, however, do not cause stability problems. Therefore, the maximum eigenvalue of both sides is a choice that ensures stability:

$$\|\mathbf{\Lambda}_n\|_{\max} = \max \left(\max \left(\left| \bar{u}_n + \sqrt{c^2} \right|, \left| \bar{u}_n - \sqrt{c^2} \right| \right)_L, \max \left(\left| \bar{u}_n + \sqrt{c^2} \right|, \left| \bar{u}_n - \sqrt{c^2} \right| \right)_R \right). \quad (3.62)$$

3.2.2 First Order Upwind Flux

For three-dimensional problems with non-uniform flow fields, no common eigenvector for all three jacobians exists. However, if the flow gradients are assumed to be negligible, the linearization $\partial \mathbf{F}_i / \partial x_i = \mathbf{J}_i \partial \mathbf{U} / \partial x_i$, used to obtain Eq. (2.90) is acceptable. Similar to section 2.4.3, the problem is simplified as a plane wave traveling perpendicularly to the element interface. For Euler and Navier-Stokes equations, this approach is commonly referred to as *Local One-Dimensional Inviscid* (LODI), since only the flux in one dimension is considered [133, 37]. With the LODI simplification, the diagonalized form of the homogeneous APE-1/4 equations, Eq. (2.91) reads:

$$\frac{\partial \mathbf{H}_n}{\partial t} + \mathbf{\Lambda}_n \frac{\partial \mathbf{H}_n}{\partial x_n} = 0 \quad (3.63)$$

with

$$\mathbf{H}_n = \begin{bmatrix} \mathcal{h}_{n,1} \\ \mathcal{h}_{n,2} \\ \mathcal{h}_{n,3} \\ \mathcal{h}_{n,4} \end{bmatrix}, \quad \mathbf{\Lambda}_n = \begin{bmatrix} 0 & 0 & 0 & 0 \\ 0 & 0 & 0 & 0 \\ 0 & 0 & \bar{u}_n - \sqrt{c^2} & 0 \\ 0 & 0 & 0 & \bar{u}_n + \sqrt{c^2} \end{bmatrix}.$$

For supersonic conditions, both acoustic waves travel in flow direction whereas for subsonic conditions, one wave propagates into the opposite direction. By virtue of the diagonalization, the Riemann problem can be solved by a simple upwind approach, where the intermediate state \mathbf{U}^* is computed from the positive and negative characteristics for the left- and right hand side states, respectively. Since the eigenvalues for the vorticity characteristics are zero, they do not propagate into interface normal direction at all, so the mean value is used:

$$\mathbf{F}^R(\mathbf{U}_L, \mathbf{U}_R) = \mathbf{J}_n \mathbf{U}^* = \mathbf{J}_n \mathbf{L}_n \mathbf{H}_n^* \quad (3.64)$$

with

$$\mathbf{H}_n^* = \begin{bmatrix} 1/2 (\mathcal{h}_{n,1,L} + \mathcal{h}_{n,1,R}) \\ 1/2 (\mathcal{h}_{n,2,L} + \mathcal{h}_{n,2,R}) \\ \begin{cases} \mathcal{h}_{n,3,L} & \text{if } \lambda_3 > 0 \\ \mathcal{h}_{n,3,R} & \text{otherwise} \end{cases} \\ \begin{cases} \mathcal{h}_{n,4,L} & \text{if } \lambda_4 > 0 \\ \mathcal{h}_{n,4,R} & \text{otherwise} \end{cases} \end{bmatrix}. \quad (3.65)$$

Direct Flux Formulation

For the upwind flux formulation (3.64), the flux jacobians J_n and eigenvector matrices L_n are required. Similar to the eigenvalue matrix Λ_n in the Lax-Friedrichs flux, these quantities are ambiguous at the element interfaces, in case a discontinuous Galerkin projection is applied to the base flow fields. Using average or maximum values would be detrimental to the stability of the solver, so a direct flux formulation is introduced, which computes the fluxes from the characteristics, without using an intermediate state. To this end, the flux jacobian is split into a positive and a negative part:

$$J_n = J_n^+ + J_n^-, \quad (3.66)$$

where

$$J_n^+ = L_n \Lambda_n^+ L_n^{-1}, \quad J_n^- = L_n \Lambda_n^- L_n^{-1} \quad (3.67)$$

and

$$\Lambda_n^+ = \begin{bmatrix} \max(\lambda_1, 0) & & & \\ & \ddots & & \\ & & \max(\lambda_j, 0) & \\ & & & \ddots \end{bmatrix}, \quad \Lambda_n^- = \begin{bmatrix} \min(\lambda_1, 0) & & & \\ & \ddots & & \\ & & \min(\lambda_j, 0) & \\ & & & \ddots \end{bmatrix}. \quad (3.68)$$

The fluxes are computed using the positive and negative jacobians, evaluated at the left and right hand side, respectively:

$$F^R(\mathbf{U}_L, \mathbf{U}_R) = [J_n^+ \mathbf{U}]_L + [J_n^- \mathbf{U}]_R. \quad (3.69)$$

The jacobian matrices can easily become rather complex and even for the rather simple APE-1/4 operator, involve several mathematical operations. Moreover, they must be computed at every interface quadrature point, for every time level. Consequently, their evaluation requires significantly more computational time than the local Lax-Friedrichs flux. It is however, still considerably more economical than an iterative Riemann solver.

3.3 Boundary Conditions

In the spectral/hp element method, boundary conditions can be implemented either by prescribing the boundary solution itself (strong BCs) or by modifying the state from which the numerical flux is calculated (weak BCs). While simpler to implement, the strong BC approach can cause severe stability restrictions and deteriorate the numerical accuracy [91]. For these reasons, all boundary conditions are implemented as weak-Riemann, where the boundary state is computed by solving a Riemann problem between the element interior and an exterior state, the ghost state. The exterior values are denoted with G and similar to the previous section 3.2, the interior values are denoted with L (cf. Fig. 3.4).

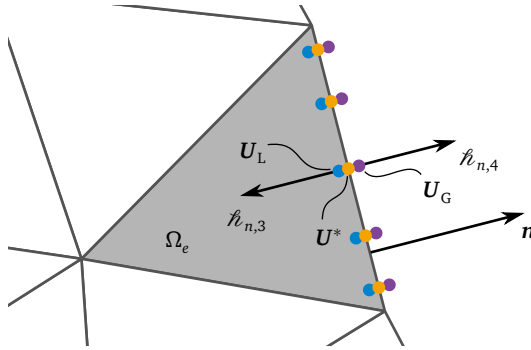


Figure 3.4: Direction and location of the relevant variables at the boundary for the APE under subsonic conditions for the element Ω_e (grey). Left hand side U_L state in blue, ghost U_G state in purple and intermediate state U^* in yellow. All three states are located in the same points in space but are shown next to each other by way of illustration.

The two fundamental boundary types for CAA are full reflection and full absorption of incident waves, i.e. *rigid wall* and *far-field* boundary conditions. The reflection of incident waves is quantified by the reflection coefficient:

$$\mathcal{R} = -\frac{h_{n,4}}{h_{n,3}}, \quad (3.70)$$

which denotes the ratio of the outgoing and the incoming acoustic characteristic.

3.3.1 Rigid Wall Boundary

The slip-wall condition imposes zero wall-normal velocities, while not affecting the wall-parallel components:

$$\mathbf{u}_L^a \cdot \mathbf{n} \stackrel{!}{=} 0. \quad (3.71)$$

This is either achieved by setting the normal velocity to zero (strong BC) or by negating it (weak BC). Since in the current implementation, the weak BC approach is pursued, the ghost state is set to:

$$\mathbf{u}_G^a = \mathbf{u}_L^a - 2(\mathbf{u}_L^a \cdot \mathbf{n})\mathbf{n}. \quad (3.72)$$

The resulting Riemann problem leads to the characteristic variables:

$$\mathbf{H}_n^* = \begin{bmatrix} \hbar_{n,1} \\ \hbar_{n,2} \\ -\hbar_{n,4} - \frac{\tilde{u}_1(\tilde{u}_2 u_2^a + \tilde{u}_3 u_3^a)}{c^2 - \tilde{u}_1^2} \\ \hbar_{n,4} \end{bmatrix}_L. \quad (3.73)$$

In subsonic flows and for one dimension, this gives $\hbar_{n,3}^* = -\hbar_{n,4}^*$ and consequently a reflection coefficient of $\mathcal{R} = 1$, indicating that the incident characteristic is fully reflected. This does not hold in multiple dimensions (i.e. $\mathcal{R} \neq 1$), since the non-normal components are not reflected.

This is accomplished by the no-slip wall condition, which is obtained by imposing zero wall velocity perturbations $\mathbf{u}_L^a \stackrel{!}{=} 0$ via:

$$\mathbf{u}_G^a = -\mathbf{u}_L^a. \quad (3.74)$$

The corresponding characteristic variables then follow as:

$$\mathbf{H}_n^* = \begin{bmatrix} 0 \\ 0 \\ -\hbar_{n,4} \\ \hbar_{n,4} \end{bmatrix}_L, \quad (3.75)$$

which yields $\mathcal{R} = 1$, even when $u_2^a \neq 0$ or $u_3^a \neq 0$.

3.3.2 Farfield Boundary

At farfield boundaries, all incoming characteristics must vanish. Implemented as weak-Riemann boundary conditions, this is accomplished by computing a ghost state from the outwards moving characteristic of the left-hand side state, while setting the incoming right hand side characteristics to zero [132]. Similar to the upwind flux solver, the LODI approach is used, where the acoustic field is considered to be one-dimensional at the face:

$$\mathbf{U}_G = \mathbf{L}_n \mathbf{H}_n^* \quad (3.76)$$

with

$$\mathbf{H}_n^* = \begin{bmatrix} \hat{h}_{n,1} \\ \hat{h}_{n,2} \\ \begin{cases} \hat{h}_{n,3} & \text{if } \lambda_3 > 0 \\ 0 & \text{otherwise} \end{cases} \\ \begin{cases} \hat{h}_{n,4} & \text{if } \lambda_4 > 0 \\ 0 & \text{otherwise} \end{cases} \end{bmatrix}_L . \quad (3.77)$$

For subsonic conditions, this gives $\hat{h}_{n,3}^* = 0$ ($\lambda_3 < 0$) and therefore a reflection coefficient of $\mathcal{R} = \infty$.

While this method should produce no incoming characteristics in one dimension, the underlying LODI approach gives non-zero incoming characteristics in multiple dimensions [37]. Moreover, numerical errors can generate additional waves at the boundary. For aeroacoustic applications, these spurious waves are hardly damped due to the absence of a diffusive term. In long-time simulations, this may spoil the simulation results or even lead to divergence [5]. Besides more advanced farfield boundary conditions [108, 130, 5], a simple yet efficient solution to this problem is the introduction of a *sponge layer*, i.e. an artificial source term that dampens the fields close to the boundary:

$$\mathbf{W}_{\text{sponge}} = C_{\text{sp}}(\mathbf{x}) \mathbf{U} \quad \text{with } C_{\text{sp}}(\mathbf{x}) < 0 . \quad (3.78)$$

3.4 Temporal Discretization

Using the approximation of integrals and gradients in sections 3.1.3 and 3.1.4, respectively, as well as the numerical fluxes defined in sections 3.2.1 and 3.2.2, the inhomogeneous advection equation (3.59) with the source term \mathbf{W}^e can be discretized as¹:

$$\frac{\partial \mathbf{q}}{\partial t} = \mathbb{G}(\mathbf{q}), \quad (3.79)$$

with the right hand side

$$\mathbb{G}(\mathbf{q}) := \mathbf{B}(\mathbf{M})^{-1}(\mathbf{b} - \mathbf{c}) + \mathbf{W}. \quad (3.80)$$

The remaining temporal derivative on the left hand side must be approximated. In order to minimize the dispersion and diffusion errors, a high order method is used for the temporal discretization as well. Consequently, the explicit, *fourth order Runge-Kutta* scheme (RK4) [116] is employed:

$$\left. \frac{\partial \mathbf{q}}{\partial t} \right|^{n+1} \approx \frac{1}{6}\boldsymbol{\theta}_1 + \frac{1}{3}\boldsymbol{\theta}_2 + \frac{1}{3}\boldsymbol{\theta}_3 + \frac{1}{6}\boldsymbol{\theta}_4, \quad (3.81)$$

where the four time stage values are successively computed as:

$$\begin{aligned} \boldsymbol{\theta}_1 &= \mathbb{G}(\mathbf{q}^n) \\ \boldsymbol{\theta}_2 &= \mathbb{G}\left(\mathbf{q}^n + \frac{1}{2}\boldsymbol{\theta}_1\Delta t\right) \\ \boldsymbol{\theta}_3 &= \mathbb{G}\left(\mathbf{q}^n + \frac{1}{2}\boldsymbol{\theta}_2\Delta t\right) \\ \boldsymbol{\theta}_4 &= \mathbb{G}\left(\mathbf{q}^n + \boldsymbol{\theta}_3\Delta t\right). \end{aligned} \quad (3.82)$$

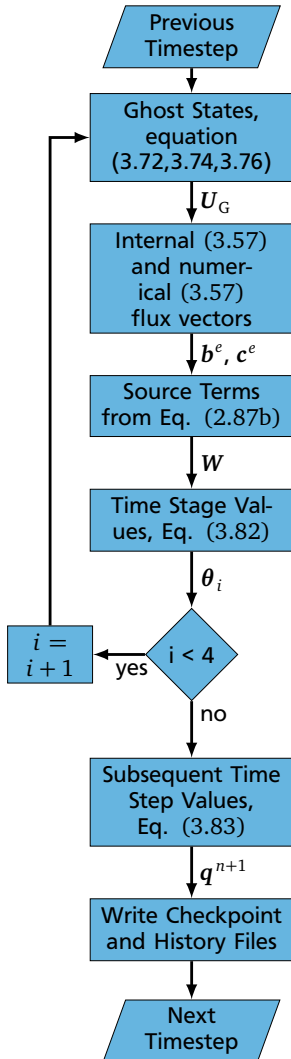
Once all time stage values are available, the subsequent time step field \mathbf{q}^{n+1} is explicitly computed as:

$$\mathbf{q}^{n+1} = \mathbf{q}^n + \Delta t \left(\frac{1}{6}\boldsymbol{\theta}_1 + \frac{1}{3}\boldsymbol{\theta}_2 + \frac{1}{3}\boldsymbol{\theta}_3 + \frac{1}{6}\boldsymbol{\theta}_4 \right). \quad (3.83)$$

The RK4 scheme computes the subsequent time level $n + 1$ from only the current one n , while using four time stages, at which the right hand side $\mathbb{G}(\mathbf{q})$ is evaluated.

¹ Since the temporal discretization is applicable to the continuous and discontinuous Galerkin methods, the superscript \square^e was dropped for the sake of brevity.

3.5 Solution Algorithm



The full algorithm used for solving the APE system is depicted in Fig. 3.5 for a single time step. At the beginning of the time step, the ghost states U_G^a are computed at the boundaries according to Eqs. (3.72, 3.74, 3.76). In a next step, the internal flux vector b^e is assembled by evaluation of the fluxes $F(q^\delta)$ and numerical integration with regard to the gradient of the expansion basis, Eq. (3.57). Similarly, the Riemann problem is solved at the element interfaces to obtain the vector of numerical fluxes c^e , Eq. (3.58). Both fluxes and the source terms W are combined to yield the right hand side of the advection equation (3.80) and the first time stage value θ_i . Subsequently, the previous steps are repeated with the intermediate field (3.82) instead of the current time step field q^n until the four time stage values of the Runge-Kutta scheme are available, i.e. $i = 4$. Finally, the four time stage values θ_i are combined as given by (3.83) to yield the subsequent time step fields q^{n+1} , which are eventually written to a restart or history file for post-processing

Figure 3.5: Flow Diagram of the CAA Solution Algorithm for a single time step.

3.6 Verification

For the developed acoustics solver, it is essential to implement the right governing equations and to solve these equations properly [116]. Therein, the assessment with regard to the former requirement is the subject of the *validation*, whereas the latter is addressed by the *verification*. Depending on the scope of a tool, the validation can involve simulations of a wide range of test cases, which then must be compared to analytical solutions, experimental results or reference simulations of higher accuracy. Due to the complexity of most modeled phenomena, analytical reference data is not available in most cases, and experiments and reference simulations can be erroneous as well. The results obtained in the context of a validation therefore require thorough interpretation and evaluation.

First steps towards the validation of the developed tool are taken in chapters 6 and 7, by means of a simple and more challenging setup, respectively. Moreover, the solver is already being used by the scientific community, where it was successfully validated and applied to a jet noise problem [94]. The verification of an implementation is much more distinct, since both, the governing equations and their solution obtained from the solver, are available. The difference between the computed solution and a corresponding exact solution can therefore be quantified. This is the aim of the current section, where initially, the discretization error is examined in order to ascertain the correct implementation of the APE system. Subsequently, this error is quantified and investigated in more detail for different discretization parameters. Finally, the practical implications of these findings are illustrated by comparing the computed and analytical solution to a simple test case.

3.6.1 Method of Manufactured Solution

The correct implementation of the APE system (2.88) is verified by means of the *Method of Manufactured Solution* (MMS) [115]. The core concept of MMS is to manufacture an analytic solution \mathbf{U}_{MS} and insert it into the governing equations. The solution is designed to not fully satisfy the equations and hence gives rise to a source term \mathbf{W}_{MS} , which can be derived analytically. When this source term is applied to a simulation using the actual implementation, it should yield the manufactured solution \mathbf{U}_{MS} . Due to the numerical errors, there will, however, be a deviation between \mathbf{U}_{MS} and the obtained solution \mathbf{U} . This error is composed of the discretization and solution errors only. Neglecting the small solution error, the discretization error follows as:

$$\mathcal{E} = \|\mathbf{U}_{\text{MS}} - \mathbf{U}\|. \quad (3.84)$$

For the discontinuous Galerkin method, the error follows a power law, causing it to decay with increased spatial resolution [35]:

$$\mathcal{E} \propto h^{P_{\text{conv}}}, \quad (3.85)$$

where h is the mesh spacing and P_{conv} the convergence order of the scheme. In the DG method, the latter is identical to the polynomial order, i.e. $P_{\text{conv}} = P$. The discretization error of a correct implementation should follow relation (3.85). Any deviation from Eq. (3.85) means that \mathcal{E} contains an additional error, e.g. due to programming or conceptual mistakes [115].

The advantage of this method is that the manufactured solution can be designed to test individual terms of the governing equations only, since the physical meaning of the manufactured solution is insignificant. Conversely, \mathbf{U}_{MS} can be chosen to exercise every term, including the boundary conditions and temporal derivatives. Hereby, the MMS requires only very few test cases, even for an extensive verification.

Two rectangular and two hexahedral domains are considered in the following, with analytical solutions and base flow fields designed to exercise every term of the APE operator. All boundaries are treated with the slip-wall condition. The wall-normal acoustic velocity perturbation $u_{n,\text{MS}}^a$ is hence required to vanish.

2D

In two dimensions, the devised manufactured solution reads:

$$\mathbf{U}_{\text{MS}}(\mathbf{x}, t) = \begin{bmatrix} p^a \\ u_1^a \\ u_2^a \end{bmatrix} = \begin{bmatrix} \sin(4\pi(x_1^2 + x_2^2)) \\ \frac{1}{c_0 \varrho_0} (-x_1^2 + 1) \sin(4\pi(x_1^2 + x_2^2)) \\ \frac{1}{c_0 \varrho_0} (-x_2^2 + 1) \cos(4\pi(x_1^2 + x_2^2)) \end{bmatrix} \quad (3.86)$$

with the base flow quantities

$$\begin{bmatrix} \bar{\varrho} \\ \bar{p} \\ \tilde{u}_1 \\ \tilde{u}_2 \end{bmatrix} = \begin{bmatrix} \varrho_0 \left(0.3 \sin \left(3\pi \left(\left(x_1 + \frac{1}{2} \right)^2 + \left(x_2 + \frac{1}{2} \right)^2 \right) \right) + 1 \right) \\ p_0 \left(0.3 \sin \left(3\pi \left(\left(x_1 - \frac{1}{2} \right)^2 + \left(x_2 - \frac{1}{2} \right)^2 \right) \right) + 1 \right) \\ 10 \sin \left(2\pi \left((x_1 - 1)^2 + (x_2 - 1)^2 \right) \right) \\ 20 \sin \left(2\pi \left((x_1 + 1)^2 + (x_2 - 1)^2 \right) \right) \end{bmatrix} \quad (3.87)$$

and the reference values

$$\varrho_0 = 1.204, \quad p_0 = 1\text{E}5, \quad \gamma = 1.4, \quad c_0 = \sqrt{\gamma \frac{p_0}{\varrho_0}}. \quad (3.88)$$

Since neither value has any physical meaning and only the spatial discretization shall be tested, all quantities are dimensionless and constant in time. The components of the velocity perturbations \mathbf{u}^a , depicted in Fig. 3.6, vanish at their respective normal walls due to the chosen boundary conditions. Substitution of the above definitions into the left hand side of the APE system (2.88) yields the analytical expression of the MMS source term \mathbf{W}_{MS} . Due to its verbosity, \mathbf{W}_{MS} is, however, not listed.

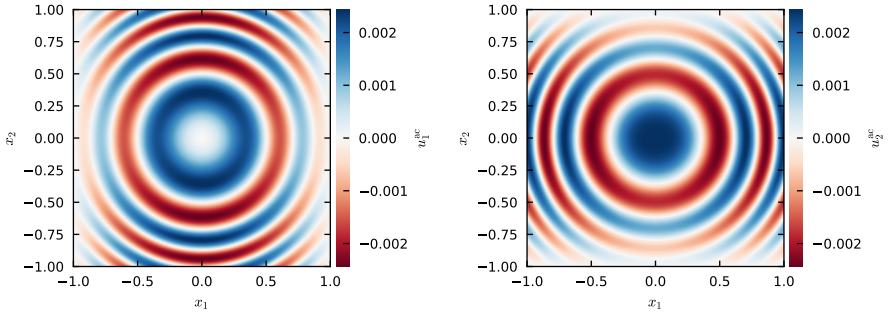
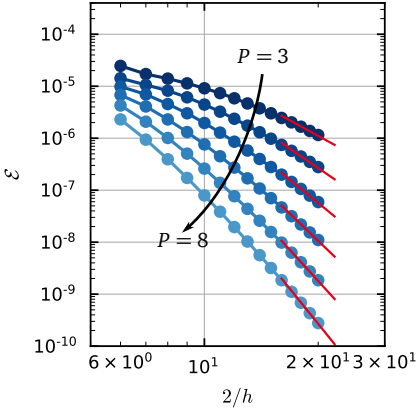


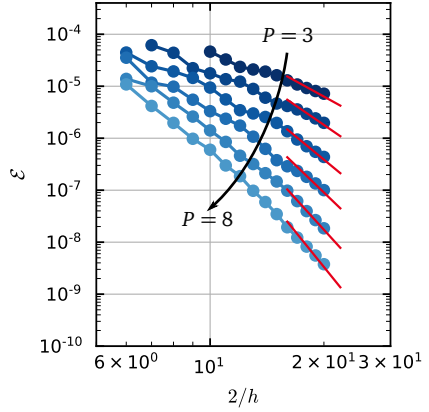
Figure 3.6: Velocity perturbations of the two-dimensional MMS.

The discretization error \mathcal{E} is given for quadrilateral and triangular elements in Fig. 3.7, for different mesh spacings h and polynomial orders P . For sufficiently fine resolutions, the errors should form straight lines with the slope P , due to the logarithmic scaling. In the present study, the error \mathcal{E} is only evaluated at the quadrature points. Due to their dependence on h and P however, neither their number nor their locations are constant, which causes the errors in Fig. 3.7 to fluctuate slightly. The fluctuations decrease for higher resolutions and orders, due to the higher number of quadrature points and the more accurate evaluation of the error.

The observed and theoretical convergence orders concur very well for the quadrilateral elements in Fig. 3.7a. With triangular elements, the simulation is not as stable for lower resolutions and exhibits larger errors, likely due to the necessary transformation from local to collapsed coordinates [62]. Nevertheless, the theoretical and observed convergence orders show good agreement for smaller mesh spacings, similar to the quadrilateral case. This demonstrates, that the discretization scheme, the APE and the boundary conditions were correctly implemented in two dimensions.



(a) Quadrilateral elements



(b) Triangular elements

Figure 3.7: L_2 errors for the 2D manufactured solution with wall boundary conditions and spatially varying base fields for different polynomial orders P and mesh spacings h . Lighter shades indicate higher orders. Theoretical slopes in red.

3D

In order to ascertain the correct implementation in three dimensions, the two-dimensional manufactured solution was extended accordingly:

$$U_{\text{MS}}(\mathbf{x}, t) = \begin{bmatrix} p^a \\ u_1^a \\ u_2^a \\ u_3^a \end{bmatrix} = \begin{bmatrix} \sin(4\pi(x_1^2 + x_2^2 + x_3^2)) \\ \frac{1}{c_0 \varrho_0} (-x_1^2 + 1) \sin(4\pi(x_1^2 + x_2^2 + x_3^2)) \\ \frac{1}{c_0 \varrho_0} (-x_2^2 + 1) \cos(4\pi(x_1^2 + x_2^2 + x_3^2)) \\ \frac{1}{c_0 \varrho_0} (-x_3^2 + 1) \cos(4\pi(x_1^2 + x_2^2 + x_3^2)) \end{bmatrix}, \quad (3.89)$$

with the base flow fields:

$$\begin{bmatrix} \bar{\varrho} \\ \bar{p} \\ \tilde{u}_1 \\ \tilde{u}_2 \\ \tilde{u}_3 \end{bmatrix} = \begin{bmatrix} \varrho_0 \left(0.3 \sin\left(3\pi\left(\left(x_1 + \frac{1}{2}\right)^2 + \left(x_2 + \frac{1}{2}\right)^2 + \left(x_3 + \frac{1}{2}\right)^2\right)\right) + 1 \right) \\ p_0 \left(0.3 \sin\left(3\pi\left(\left(x_1 - \frac{1}{2}\right)^2 + \left(x_2 - \frac{1}{2}\right)^2 + \left(x_3 - \frac{1}{2}\right)^2\right)\right) + 1 \right) \\ 10 \sin\left(2\pi\left(\left(x_1 - 1\right)^2 + \left(x_2 - 1\right)^2 + \left(x_3 - 1\right)^2\right)\right) \\ 20 \sin\left(2\pi\left(\left(x_1 + 1\right)^2 + \left(x_2 - 1\right)^2 + \left(x_3 - 1\right)^2\right)\right) \\ 15 \sin\left(2\pi\left(\left(x_1 + 1\right)^2 + \left(x_2 - 1\right)^2 + \left(x_3 + 1\right)^2\right)\right) \end{bmatrix} \quad (3.90)$$

and identical reference values.

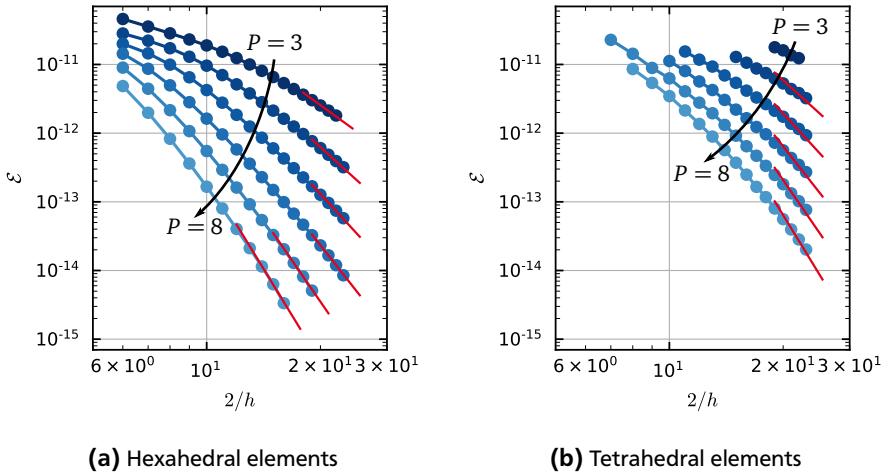


Figure 3.8: L_2 errors for the 3D manufactured solution with wall boundary conditions and spatially varying base fields for different polynomial orders P and mesh spacings h . Lighter shades indicate higher orders. Theoretical slopes in red.

The resulting discretization errors are depicted in Fig. 3.8 for hexahedral and tetrahedral elements. A similar behavior as in the two-dimensional case is observable for both element types. In particular with the hexahedral elements, the observed and theoretical convergence orders are in good agreement. Compared to the triangular elements, even higher resolutions and polynomial orders are required to facilitate a stable simulation using tetrahedra, due to the two additional collapsed edges. However, for sufficiently small h , power law convergence according to Eq. (3.85) is reached as well.

It was therefore demonstrated that for the four considered element types, the acoustics solver correctly implements the APE. Moreover, its convergence error \mathcal{E} adheres to the power law (3.85), indicating, that the discretization error is the only significant error source, as expected.

3.6.2 Dispersion and Diffusion Errors

The discretization error can be classified into dispersion and diffusion error, which shall be assessed by comparison to a spatial eigensolution analysis [90] for both Riemann solvers. To this end, the solution to the one-dimensional APE is assumed to be composed of wave-like components of the form

$$p^a(x, t) = \hat{p}^a e^{i(kx - \omega t)}, \quad (3.91)$$

with the complex pressure amplitudes \hat{p}^a , the wave number k and the angular frequency ω . For wave propagation, the dispersion relation

$$k = \frac{\omega}{c} \quad (3.92)$$

relates the angular frequency ω of each mode to a wave number k and vice versa. Ideally, this relation is constant and all wave components are transported at the exact speed of sound. Due to the numerical discretization, this is, however, not the case and each mode of the numerical solution behaves as if related to a complex, modified wave number $k^* = k_R^* + k_I^*$ that deviates from the real, exact wave number k . Using the dispersion relation, the discretized representation of the wave-like component is given as:

$$p^a(x, t) = \hat{p}^a e^{-k_I^* x} e^{i(k_R^* x - \omega t)}. \quad (3.93)$$

Since the first exponent is real and negative, the imaginary part k_I^* of the modified wave number attenuates the amplitude of the wave component, acting as numerical diffusion. The real part k_R^* alters the phase of the wave component and hence manifests as numerical dispersion. Consequently, the two parts quantify the *diffusion error* and the *dispersion error*. For CAA, the latter is of particular importance, since it determines the frequency domain error. Moreover, it governs the evolution of spurious modes, which are barely damped in CAA due to the lack of (large) viscous terms and can spoil the results or lead to instabilities for long integration times [90].

Both errors depend on the wave number or frequency and increase with growing frequencies or wave numbers. For a given numerical scheme, their temporal evolution can be quantified by means of a temporal eigensolution analysis, while the spatial analysis is more appropriate for wave propagation in flows with in- and outflow conditions [90]. Consequently, the discretization errors of the current implementation can be quantified by evaluating its actual dispersion and diffusion errors in a numerical experiment.

To this end, a one-dimensional channel with a length of $l = 10$ m, a speed of sound of $c = 340$ m/s and a baseflow velocity of $u = 1/2c$ is considered. At the $x = 0$ m boundary, an incoming harmonic wave with $f = \frac{kc}{2\pi}$ is imposed, which leaves the domain through a far field boundary condition at $x = 10$ m. The domain is discretized by 20 equidistant elements of $h = 0.5$ m and an expansion basis of order $1 \leq P \leq 5$. Since the spatial discretization error is to be explored, a fourth order Runge-Kutta scheme with a rather small step size of $\Delta t = 0.2E-6$ s was employed.

The modified wave number is then found by considering a wave component at two distinct locations, x_1 and $x_2 = x_1 + \Delta x$:

$$\begin{aligned} p_1^a(x_1, t) &= p_2^a(x_2, t) \\ \Leftrightarrow \frac{\hat{p}_1^a}{\hat{p}_2^a} &= \frac{e^{i(k^*(x_1 + \Delta x) - \omega t)}}{e^{i(k^*x_1 - \omega t)}} \\ \Leftrightarrow k^* &= \frac{i}{\Delta x} \ln\left(\frac{\hat{p}_1^a}{\hat{p}_2^a}\right). \end{aligned} \quad (3.94)$$

With $\Delta x = 1.25$ m, the real and complex modified wave numbers can be computed from the Fourier coefficient that corresponds to the prescribed frequency f :

$$\Rightarrow k_R^* = \Re\left\{\frac{i}{\Delta x} \ln\left(\frac{\hat{p}_1^a}{\hat{p}_2^a}\right)\right\} \quad \text{and} \quad k_I^* = \Im\left\{\frac{i}{\Delta x} \ln\left(\frac{\hat{p}_1^a}{\hat{p}_2^a}\right)\right\}. \quad (3.95)$$

The normalized components of k^* are depicted in Fig. 3.9 for both Riemann solvers and different polynomial orders. All values were normalized with the length measure of one degree of freedom in the hp setting, $h/(P + 1)$, so that the values on the abscissa mark the wave number per N_{DOF} . This illustrates, how both errors can either be decreased by using a higher N_{DOF} at constant P , or by using higher polynomial orders at constant N_{DOF} . While for the former option, the computational cost increases linearly, it grows much slower when only P is increased. This difference is the key to why higher order methods can provide superior efficiency for CAA applications, where the discretization error is essential.

The results obtained with the first order upwind solver show perfect agreement with the spatial eigensolution analysis performed by Mengaldo et al. [90]. The analytical study is based on an upwind solver applied to a simple advection problem, using the spectral/hp element method in conjunction with a discontinuous Galerkin projection. Accordingly, the agreement indicates a correct implementation of the discretization scheme and the Riemann solver. The LLF Riemann solver exhibits slightly higher degrees of diffusion and dispersion. This difference is, however, only relevant for larger Mach number ($Ma \gg 0.1$) base flows. For quiescent

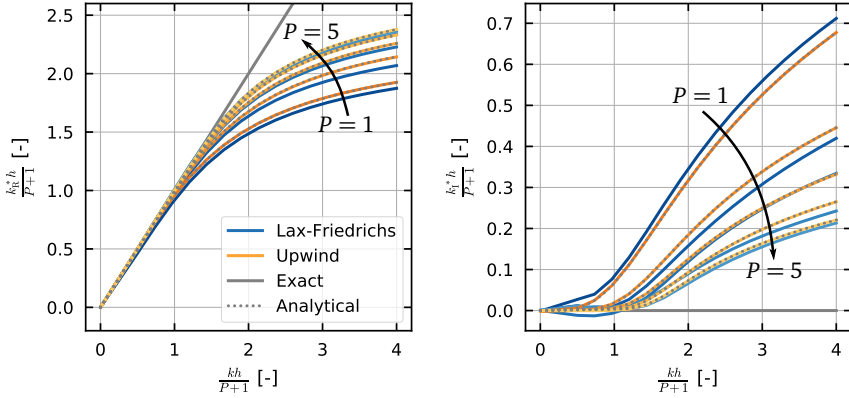


Figure 3.9: Dispersion and diffusion errors obtained with local Lax-Friedrichs and first order upwind Riemann solvers. Analytical data from [90]. Exact values in grey.

($\mathbf{u} = 0$), homogeneous (const. ρ and const. p) media, the LLF and first order upwind solver give identical solutions, resulting in identical diffusion and dispersion behavior (not shown). This suggests that for most combustion noise applications, where typically only low Mach numbers are relevant, the local Lax-Friedrichs solver is sufficient.

3.6.3 Application to a Spinning Vortex Pair

In the two previous sections, the correct behavior of the discretization error, as well as its impact on wave transport were investigated by means of one-dimensional, theoretical test cases. To conclude the verification, an actual acoustic wave propagation problem is now considered. Therefore, the “spinning vortex pair”, which is also subject of the original APE publication [34] and a recurring test case in literature is reproduced.

The setup involves a two-dimensional vortex pair, located r_0 from the center ($\mathbf{x} = 0$) of a quadratic domain with quiescent air. The opposing vortices rotate around the center at an angular frequency of $\omega = \Gamma/4\pi r_0^2$, where Γ denotes the circulation. The rotation period is $T = 8\pi^2 r_0^2/\Gamma$ and the corresponding Mach number is $Ma_r =$

$\Gamma/4\pi r_0 c$. For this setup, Ewert and Schröder [34] give the analytical source terms for the APE-4 as:

$$\dot{\omega}_c = \dot{\omega}_e = \dot{\omega}_{c\&e} = 0 \quad (3.96)$$

$$\dot{\omega}_m = -\frac{\Gamma^2 \mathbf{e}_r(t)}{8\pi^2 r_0^3} \sum_{j=1}^2 (-1)^j \exp\left(-\frac{|\mathbf{x} + (-1)^j \mathbf{r}_0(t)|^2}{2r_0^2}\right), \quad (3.97)$$

with $\mathbf{r}_0 = r_0 \mathbf{e}_r$, $\mathbf{e}_r = [\cos(\vartheta), \sin(\vartheta)]^T$ and $\vartheta = \omega t$.

An analytical solution for the acoustic pressure is available from Müller and Obermeier [97] with:

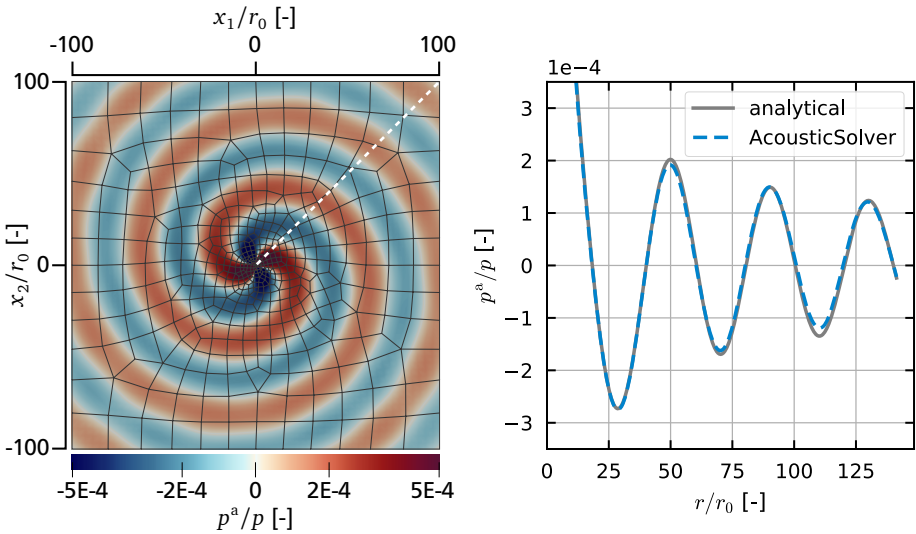
$$p^a(r, \vartheta, t) = \Re \left\{ -i \frac{\varrho \Gamma^4}{64\pi^3 r_0^4 c^2} H_2^{(2)}(kr) e^{i2(\omega t - \vartheta)} \right\}, \quad (3.98)$$

where $H_2^{(2)}$ denotes the Hankel function of the second kind and order two.

The computational domain is rectangular with dimensions $-100 r_0 \leq x_1, x_2 \leq 100 r_0$ and far-field boundary conditions. It is discretized by an unstructured mesh, as depicted in Fig. 3.10a and a fifth order expansion, $P = 5$. The mesh comprises $N_{\text{el}} = 465$ quadrilateral elements and was refined at the center, so that element sizes between $0.3 r_0 \leq h$ and $h \leq 32 r_0$ are reached.

The acoustic pressure distribution for $\Gamma/(cr_0) = 1.0$ and $Ma_r = 0.0795$ at $t = 1$ s is depicted in Fig. 3.10. Therein, the computed solution conforms with the analytical solution, with minor deviations at the first maximum and third minimum. These are in line with the results shown in [34], where similar deviations were observed. These were attributed to a sponge layer around the boundaries, which, however, was not used in the current simulation. Moreover, the obtained solution does not change for higher polynomial orders, smaller mesh spacings, and different element types. Due to the uniform speed of sound and zero base flow velocities, it is also independent of the two implemented Riemann solvers. This suggests that the smaller peak values are not due to the discretization error.

For the original simulation, a fourth order FDM scheme was applied to an orthogonal mesh of $N_{\text{DOF}} = 141 \times 141 = 19881$ nodes. At the boundaries, a sponge layer was attached and spurious waves were removed by a spatial filter. For the current simulation, the discretization amounts to a total number of degrees of freedom of $N_{\text{DOF}} = 16740$ per quantity, which is 84.2% of the N_{DOF} of the original simulation. Moreover, neither filtering, damping or specialized boundary conditions were used, which illustrates the numerical efficiency and stability of the spectral/hp element method.



(a) Numerical mesh (black), sample line (white) and instantaneous acoustic pressure field.

(b) Acoustic pressure along sample line, obtained with the developed solver and analytical solution [97]

Figure 3.10: Normalized acoustic pressure for $\Gamma/(cr_0) = 1.0$ and $Ma_r = 0.0795$ at $t = 1$ s.

4 Numerical Implementation of the Flow Solver

The second part of the mathematical model consists of the chemistry manifold and the low Mach number, Favre-averaged governing equations (2.79). In this work, these governing equations are discretized by a cell-centered finite volume method on unstructured meshes. The method is related to the discontinuous Galerkin formulation of the spectral/hp element method, described in chapter 3, as it is similarly based on a domain decomposition and inter-element fluxes. However, it uses different weighting and trial functions, as well as single-point Gaussian quadrature, limiting the current implementation to second order convergence. A comparison of FVM and DG can be found e.g. in [124]. The finite volume method is widely adopted and covered in literature. Due to its relatively simple formulation, it allows for highly optimized implementations and easy adaption of novel modeling approaches, while providing favorable stability and flexibility with regard to complex geometries [35].

Reactive simulations based on FVM are an established approach for the simulation of laboratory scale and industry scale combustion chambers [43, 58]. Consequently, the Rolls-Royce Deutschland and TU Darmstadt developed, time-implicit, CFD tool PRECISE-UNS¹ [4] is used. The code has been an integral part of the combustor design process and, apart from the added coupling interface, was not modified. It is based on Ferziger and Peric [35], which therefore is also the basis of the current chapter, if not stated otherwise. Consequently, it is adhered to the formulations and termini that are common in the finite volume method. The chapter commences by reviewing the approximation of integrals, differentials and fluxes of the finite volume method. Subsequently, the temporal discretization scheme and the pressure-velocity coupling strategy are introduced, before an overview of the complete solution algorithm is given.

¹ PRECISE-UNS: Predictive System for Real Engine combustors with Improved Submodels and Efficiency - Unstructured

4.1 Finite Volume Method

The generic transport equation of an arbitrary quantity $q(\mathbf{x}, t)$ is given as:

$$\frac{\partial \rho q}{\partial t} + \nabla \cdot \mathbf{F}^C(q) = \nabla \cdot \mathbf{F}^D(q) + \dot{\omega}, \quad (4.1)$$

with the advective and diffusive fluxes:

$$\begin{aligned} \mathbf{F}^C(q) &= \rho \mathbf{u} q \\ \mathbf{F}^D(q) &= \rho \mathcal{D} \nabla q. \end{aligned}$$

Identical to the h -extension of the spectral/hp element method, the finite volume method divides the computational domain Ω into a number of non-overlapping elements Ω_e as specified by Eq. (3.9). In the context of the FVM, these elements are referred to as *cells* or *Control Volumes* (CV). The integral form of Eq. (4.1) in a single control volume Ω_e is accordingly:

$$\int_{\Omega_e} \frac{\partial \rho q}{\partial t} d\Omega_e + \int_{\Omega_e} \nabla \cdot \mathbf{F}^C(q) d\Omega_e = \int_{\Omega_e} \nabla \cdot \mathbf{F}^D(q) d\Omega_e + \int_{\Omega_e} \dot{\omega} d\Omega_e \quad (4.2)$$

Application of Gauss' theorem yields:

$$\int_{\Omega_e} \frac{\partial \rho q}{\partial t} d\Omega_e + \int_{\partial\Omega_e} \mathbf{F}^C(q) \cdot \mathbf{n} d(\partial\Omega_e) = \int_{\partial\Omega_e} \mathbf{F}^D(q) \cdot \mathbf{n} d(\partial\Omega_e) + \int_{\Omega_e} \dot{\omega} d\Omega_e, \quad (4.3)$$

where \mathbf{n} denotes the surface normal of $\partial\Omega_e$. Due to the element-wise constant weighting function, which was implied in Eq. (4.2), the above equation involves only inter-elemental fluxes.

4.1.1 Integration

Each CV surface $\partial\Omega_e$ is again decomposed into non-overlapping faces S_f , so that the flux integrals are decomposed as:

$$\int_{\partial\Omega_e} \mathbf{F}^{C/D}(q) \cdot \mathbf{n} d(\partial\Omega_e) = \sum_f \int_{S_f} \mathbf{F}^{C/D}(q_L, q_R) \cdot \mathbf{n} dS_f. \quad (4.4)$$

The surface integrals in the terms (4.4) are evaluated using two-dimensional Gaussian quadrature with a single quadrature point in the face center \mathbf{x}_f , also referred to as the *midpoint rule* [35]:

$$\int_{S_f} \mathbf{F}^{C/D}(q_L, q_R) \cdot \mathbf{n} \, dS_f \approx \delta S_f \mathbf{F}^{C/D}(q_L, q_R) \cdot \mathbf{n}, \quad (4.5)$$

where δS_f denotes the area of the face S_f . The volume integrals in Eq. (4.3) are similarly approximated from the value at the CV center \mathbf{x}_p using a single point Gaussian quadrature, the three-dimensional midpoint rule:

$$\int_{\Omega_e} \frac{\partial \varrho q}{\partial t} \, d\Omega_e \approx \left. \frac{\partial \varrho q}{\partial t} \right|_p \delta V \quad \text{and} \quad \int_{\Omega_e} \dot{\omega} \, d\Omega_e \approx \dot{\omega}_p \delta V, \quad (4.6)$$

where δV denotes volume of the CV.

4.1.2 Advective and Diffusive Fluxes

The evaluation of the fluxes is identical to the discontinuous Galerkin method with a single face quadrature point and can be achieved by means of numerous flux formulations. For instance, the advective term is approximated based on the face normal velocity u_n using first order upwind flux as

$$\mathbf{F}^C(q_L, q_R) \approx \begin{cases} (\varrho \mathbf{u} q)_P & \text{if } \mathbf{u} \cdot \mathbf{n} > 0 \\ (\varrho \mathbf{u} q)_N & \text{if } \mathbf{u} \cdot \mathbf{n} < 0 \end{cases}, \quad (4.7)$$

similar to section 3.2.2. In the above expression, the left and right hand side states were extrapolated from the cell center values of the current control volume and its adjacent volume as $q_L \approx q_P$ and $q_R \approx q_N$, respectively. Since it is of first order, the upwind flux introduces significant numerical diffusion, which on the one hand, decreases the method's overall accuracy but on the other hand, improves the numerical stability. A second order interpolation is the *Central Differences Scheme* (CDS), where the face values are computed from both cell centers, weighted by their distance:

$$\mathbf{F}^C(q_L, q_R) \approx \alpha (\varrho \mathbf{u} q)_P + (1 - \alpha) (\varrho \mathbf{u} q)_N, \quad (4.8)$$

with

$$\alpha = \frac{\mathbf{n}_f \cdot (\mathbf{x}_f - \mathbf{x}_P)}{\mathbf{n}_f \cdot (\mathbf{x}_f - \mathbf{x}_P) + \mathbf{n}_f \cdot (\mathbf{x}_N - \mathbf{x}_f)}.$$

While it introduces much less diffusion, this interpolation can cause oscillations and numerical instabilities. Due to its symmetry however, CDS is often used for the diffusive fluxes:

$$F^D(q_L, q_R) \approx \alpha (\rho \mathcal{D} \nabla q)_P + (1 - \alpha) (\rho \mathcal{D} \nabla q)_N . \quad (4.9)$$

The interpolation from the CV center to the face in Eq. (4.8) is based on the assumption, that the vector $\mathbf{x}_P - \mathbf{x}_N$ intersects the face f at its center \mathbf{x}_f . This however, does not hold for non-orthogonal meshes, as shown in figure 4.1. Consequently, the CDS interpolations (4.8) and (4.9) yield the values and gradients of $q_{f'}$ instead of q_f . The accuracy of the method is therefore improved by using a

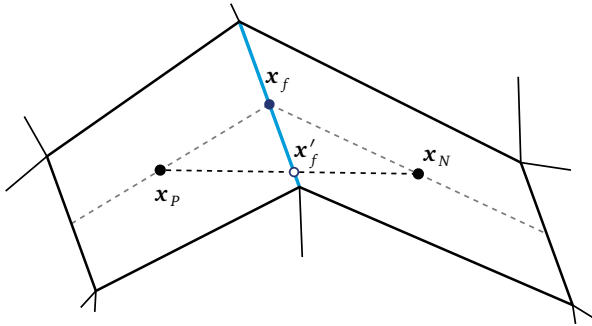


Figure 4.1: CDS Interpolation at the face center.

second order extrapolation:

$$q_L \approx q_P + (\nabla q)_P \cdot (\mathbf{x}_f - \mathbf{x}_P) . \quad (4.10)$$

4.1.3 Differentiation

The gradient at the cell centers is also approximated by the midpoint rule, which after application of Gauss' theorem, yields a surface integral:

$$(\nabla q)_P \approx \frac{1}{\delta V} \int_{\Omega_e} \nabla q \, d\Omega_e \approx \frac{1}{\delta V} \int_{\partial \Omega_e} q \mathbf{i} \cdot \mathbf{n} \, d(\partial \Omega_e) , \quad (4.11)$$

that can be approximated with the midpoint rule, as described in section 4.1.1:

$$\Rightarrow (\nabla q)_P \approx \frac{1}{\delta V} \sum_f q_f \mathbf{i} \cdot \mathbf{n} \, \delta S_f . \quad (4.12)$$

4.2 Temporal Discretization

With the approximated integrals and differentials as well as the advective and the diffusive fluxes, the transport equation (4.1) is fully discretized in space and depends only on the CV center values q_p , a source term $\dot{\omega}$ and number of geometric factors. The latter are hereafter combined into the constant factors A_p and A_C for each control volume P and its neighbor volumes $C \in \{N_1, N_2, \dots\}$, respectively. The discretized transport equation can hence be written as

$$\left. \frac{\partial \varrho q}{\partial t} \right|_P \delta V + A_p q_p + \sum_C A_C q_C = \dot{\omega}_p \quad \text{with } C \in \{N_1, N_2, \dots\}. \quad (4.13)$$

The remaining time derivative is approximated with an implicit, one stage, three level, second order scheme [35]:

$$\left. \frac{\partial q}{\partial t} \right|_P^{n+1} \approx \frac{3q^{n+1} - 4q^n + q^{n-1}}{2\Delta t}. \quad (4.14)$$

Substitution into Eq. (4.13) gives:

$$\left[\frac{3\varrho q^{n+1} - 4\varrho q^n + \varrho q^{n-1}}{2\Delta t} \right]_P \delta V + \left[A_p q_p + \sum_C A_C q_C \right]^{n+1} = \dot{\omega}_p^{n+1}. \quad (4.15)$$

The source term $\dot{\omega}_p^{n+1}$ is not known at the time level t^{n+1} and simply approximated from its last iteration at t^n . The values of ϱq^n and ϱq^{n-1} are known and can be included in $\dot{\omega}_p^n$. The remaining factor $3\delta V \varrho / (2\Delta t)$ is similarly moved into A_p and A_C . Consequently, these factors now also depend on the time step Δt . The final, spatially and temporally discretized generic governing equation (4.1) for the control volume P at the time t^{n+1} is:

$$A_p q_p^{n+1} + \sum_C A_C q_C^{n+1} = \dot{\omega}_p^n. \quad (4.16)$$

Construction and Solution of the Global System

Application of Eq. (4.16) to every control volume yields a coupled system of algebraic equations, which can be written as

$$\mathbf{A} \mathbf{q}^{n+1} = \mathbf{W}^n, \quad (4.17)$$

where \mathbf{q}^{n+1} denotes the solution vector of all q_p^{n+1} at time t^{n+1} , \mathbf{W}^n the source term vector at time t^n and \mathbf{A} a sparse matrix with as many entries per line as

neighbor cells. The solution of Eq. (4.17) is the most computationally expensive step in the solution process and therefore crucial for the overall computational cost of the CFD simulation. Consequently, numerous solution algorithms are available, which accomplish this task with varying efficiency based on the matrix \mathbf{A} . In the present work, a parallel algebraic multi-grid solver is used [101] for all governing equations, that has shown to provide good performance and stability for the scheme described in the previous sections.

4.3 Pressure-Velocity Coupling

With the temporal and spatial discretization schemes described in section 4.1, the low Mach number, Favre averaged flow governing equations (2.79) can be rewritten as a linear equation system (4.17), which contains all unknowns at every cell center. This system can be solved directly to obtain a flow field at the time t^{n+1} . For small computational meshes and few degrees of freedom, this *direct approach* can give sufficient computational efficiency. However, when applied to larger flow problems, this approach soon becomes inefficient and a sequential solution of each governing equation is more adequate. As discussed in section 2.1.6, the system (2.79) is highly coupled, so that no single governing equation can be solved independently. Consequently, their sequential solution is accomplished in an iterative procedure, carried out for each time step $n + 1$. To avoid confusion, the solution steps of the algebraic system (4.17) are referred to as inner iterations, while the term outer iterations refers to the sequential solution of the governing equations.

Starting with an estimated pressure p^* , the discretized momentum equations

$$A_p u_{i,p}^* + \sum_C A_C u_{i,C}^* = W_p^{m-1} - \left. \frac{\delta p^*}{\delta x_i} \right|_p \quad (4.18)$$

yield the preliminary velocities u_i^* . The discretization of the pressure gradient is not relevant at this time and denoted by the placeholder $\delta p / \delta x_i$. In a second step, the pressure velocity corrections p' and u_i' need to be computed to obtain their respective corrected values with:

$$u_i^m = u_i^* + u_i' \quad \text{and} \quad p^m = p^* + p' . \quad (4.19)$$

The corrected mass fluxes \dot{m}_f through face f follow as:

$$\dot{m}_f^m = [\varrho^{m-1} (u_i^* + u_i') \delta S]_f \quad (4.20a)$$

$$\Leftrightarrow \dot{m}_f^m = \underbrace{(\varrho^{m-1} u_i^* \delta S)_f}_{=\dot{m}_f^*} + \underbrace{(\varrho^{m-1} u_i' \delta S)_f}_{=\dot{m}_f'} \quad (4.20b)$$

$$\Rightarrow \dot{m}_f^m = \dot{m}_f^* + \dot{m}_f' . \quad (4.20c)$$

Since the preliminary velocities u_i^* were computed only from the momentum equation, they violate the continuity equation, giving rise to an excess mass flux W_m^* :

$$\left. \frac{\partial \varrho}{\partial t} \right|_P \delta V + \sum_f \dot{m}'_f = W_m^*, \quad (4.21)$$

which has to be compensated by the mass flux corrections \dot{m}'_f :

$$\sum_f \dot{m}'_f + W_m^* = 0. \quad (4.22)$$

Substitution of the discretized continuity equation yields a relation for the velocity corrections

$$\sum_f (\varrho^{m-1} u'_i \delta S)_f = - \sum_f (\varrho^{m-1} u_i^* \delta S)_f - \left. \frac{\partial \varrho}{\partial t} \right|_P \delta V. \quad (4.23)$$

4.3.1 Interpolation of Velocity Corrections

The velocity correction equation (4.23) is defined at the CV faces, whereas the discretized momentum equation (4.18) yields the preliminary velocities at the CV centers. Therefore, the velocity corrections must be interpolated, so that each mass flux correction \dot{m}'_f is expressed via the pressure corrections at the centers of the two adjacent cells, p'_p and p'_N :

$$u'_{i,f} = \langle \tilde{u}'_{i,p} \rangle_{p \rightarrow f} - \left\langle \frac{1}{A_p^{u_i}} \right\rangle_{p \rightarrow f} \left. \frac{\delta p'}{\delta x_i} \right|_f \quad \text{with} \quad \tilde{u}'_{i,p} = \frac{-\sum_C A_C^{u_i} u'_{i,C}}{A_p^{u_i}}, \quad (4.24)$$

where $\langle \rangle_{p \rightarrow f}$ denotes the interpolation from the cell center \mathbf{x}_p to the face \mathbf{x}_f . The neighbor corrections $\langle \tilde{u}'_{i,p} \rangle_{p \rightarrow f}$ contain the cell center values at every cell adjacent to the cell P . Therefore, taking these into account would heavily increase the bandwidth of the matrix corresponding to Eq. (4.23), making its solution excessively computationally expensive.

This is avoided by using the SIMPLE² algorithm, which neglects the neighbor terms. Although this causes the corrected mass fluxes to not fully satisfy the continuity equation, this error decreases with every outer iteration and eventually

² SIMPLE: Semi-Implicit Method for Pressure Linked Equations

reaches the same levels as without this simplification. The additional computational cost introduced by the higher number of required outer iterations outweighs the cost that the reduced sparsity would have brought about. Other algorithms, such as PISO³, improve the computational efficiency by e.g. introducing a second correction step, that computes the neighbor terms explicitly [35].

The second simplification inherent to the interpolation of the velocity corrections is related to non-orthogonal meshes. The interpolation of the pressure gradient $(\delta p'/\delta x_i)_f$ at the face f requires the gradients at the centers of both adjacent cells, which in turn requires the pressures at every neighbor cell. Analogous to the neighbor corrections in Eq. (4.24), this subverts the sparsity of the matrix corresponding to Eq. (4.23). Instead, the non-orthogonality is ignored and the same interpolation is used as for the CDS fluxes (4.9). The error is again decreased with each outer iteration. Similar to the PISO algorithm, an additional non-orthogonality corrector step can be used to speed up the convergence [35].

Since the coefficient $A_p^{u_i}$ has the same value for all directions, Eq. (4.24) can easily be transformed into face-normal direction [35]. Substitution of the transformed and interpolated velocity corrections in Eq. (4.23) yields the discrete equivalent of the pressure equation (2.25), the pressure correction equation:

$$\sum_f \left[-\frac{(\varrho^{m-1} \delta S)_f}{\|\mathbf{x}_{N'} - \mathbf{x}_{P'}\|} \left\langle \frac{1}{A_p^{u_i}} \right\rangle_{p \rightarrow f} [p'_N - p'_P] \right] = -\sum_f (\varrho^{m-1} u_n^* \delta S)_f - \frac{\partial \varrho}{\partial t} \Big|_p^m \delta V. \quad (4.25)$$

³ PISO: Pressure-Implicit with Splitting of Operators

4.4 Solution Algorithm

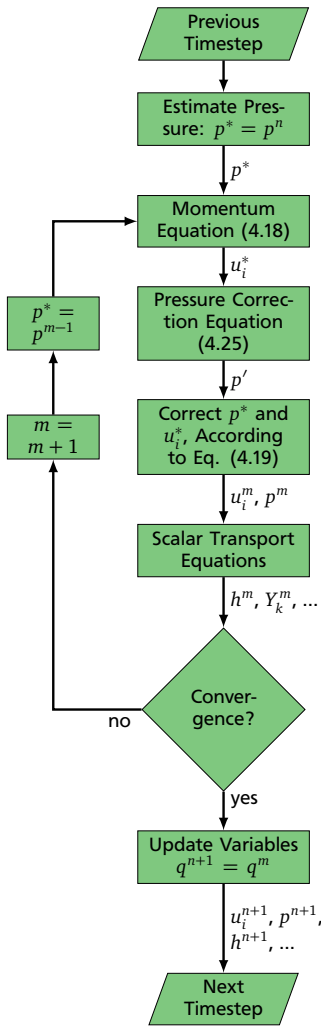


Figure 4.2: Flow diagram of the SIMPLE algorithm with outer iteration counter variable m .

The complete SIMPLE algorithm for the low Mach number, Favre-averaged flow governing equations (2.39) is depicted in Fig. 4.2. At first the pressure p^* is estimated either from the previous time step or outer iteration. Then, the momentum equation (4.18) is solved to obtain the preliminary velocities u_i^* . Using these, the preliminary mass fluxes \dot{m}^* and temporal density variations on the right hand side of the pressure correction equation (4.25) are computed explicitly. Then, Eq. (4.25) is solved for the pressure p' and, using Eqs. (4.24) and (4.19), the corrected pressure p^m and velocities u_i^m are obtained. Subsequently, all other scalar equations for e.g. enthalpy, species or turbulent quantities are solved. In case the convergence criterion, e.g. a mass defect threshold is reached, the algorithm proceeds with the next time step. If not, the momentum equation is solved again, using the current variables and the loop starts over.

The steps defining the algorithm's computational cost are the solution of the momentum and pressure correction equations. As laid out in section 4.2, both are treated with a method that performs iterations itself, the inner iterations. The convergence rate of the algorithm is reduced by the two simplifications made in the interpolation of the velocity corrections. The corresponding neighbor and non-orthogonality corrector loops would solve a similar equation as Eq. (4.25) and return to the correction step, before the convergence check.



5 Implementation of the Coupling Layer

The foundation of the hybrid CAA methods for coinciding computational domains is the acoustic decomposition $q = q^{\text{loMa}} + q^{\text{a}}$, Eq. (2.80). As shown in section 2.4.3, the acoustic quantities propagate with the speed of sound, while the low Mach number components are advected at flow speed. In technical combustion systems, the latter is approximately thirty times smaller than the speed of sound. Consequently, the time scales of the acoustic quantities are significantly smaller than those of the low Mach number components. This discrepancy is exploited by the hybrid CAA methods, where flow and acoustics are treated with distinct solvers. Thereby, the computational cost is reduced by allowing for simpler CAA governing equations and a larger CFD time step.

However, when enclosed configurations are considered, the flow and acoustic fields often differ not only with regard to their time scales, but also their length scales. This difference is particularly significant in combustion noise applications, where low frequency ranges are relevant. Their corresponding wavelengths are at least one magnitude larger than the smallest scales of the CFD¹. Hence, the two simulations differ not only in terms of time scales, but also in length scales considerably, enabling an additional optimization of the computational cost. Therefore, the developed coupling strategy enables the exploitation of different spatial scales in addition to the difference in temporal scales for FVM-DG-based hybrid CAA methods, in order to further improve the computational efficiency.

In the current mathematical model, the APE system (2.88) is coupled with the Favre-averaged, low Mach number flow governing equations (2.79) by the low Mach number velocities $\tilde{\mathbf{u}}$, the density $\bar{\rho}$ and the acoustic source term $\dot{\omega}_{\text{e,loMa}}$ (2.87b). In the opposite direction, the flow governing equations are connected via the acoustic perturbations p^{a} , which serve as input for a feedback model, such as the acoustic pressure gradient (2.92). An overview of the transferred fields and their incorporation into the governing equations of the receiving solvers is given in Fig. 5.1. In order to implement this scheme, the exchanged quantities

¹ Combustion noise typically occurs below 5 kHz [28]. At $c = 341$ m/s, this corresponds to wavelengths larger than $\lambda > 68.2$ mm. The flame thickness is of magnitude ≈ 0.1 mm or ≈ 1 mm with ATF; see section 2.3.3.2.

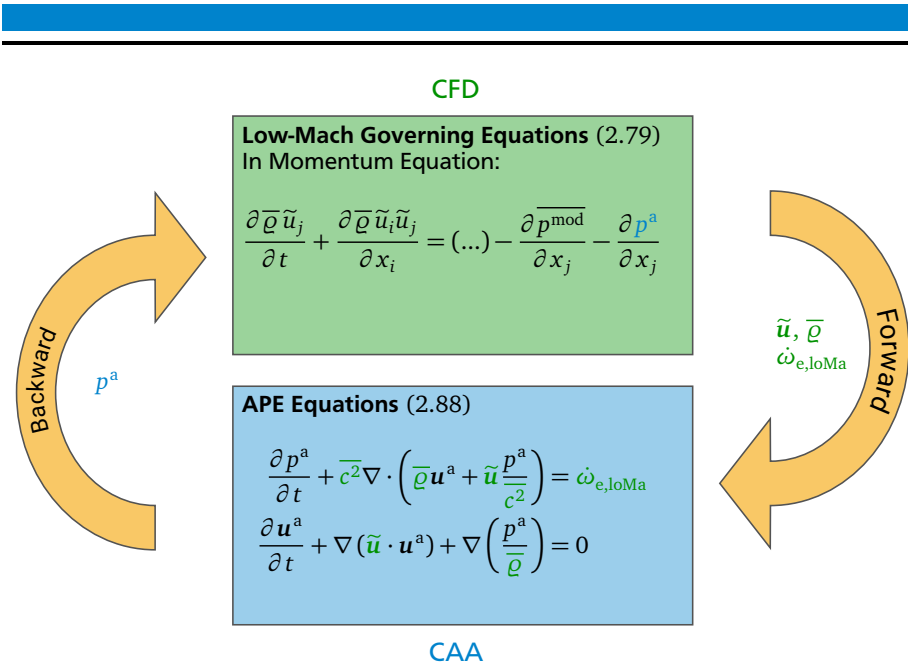


Figure 5.1: Schematic of the bi-directional coupling with exchanged fields during forward and backward coupling steps.

must be made available in each receiving application, using its native mathematical representation, numerical discretization and data format. Consequently, the data exchange comprises four major steps:

1. Preparation of the required fields
2. Data transfer
3. Spatial representation
4. Temporal interpolation

Due to the different time and length scales, as well as the substantial differences between the spatial discretizations, the implementation of the above steps is strongly dependent on whether the fields are transferred from the CFD solver to the CAA solver or vice versa. The two directions are referred to as *forward* (CFD → CAA) and *backward* (CAA → CFD) coupling, respectively. In the following, the four major coupling steps are described in detail, followed by an overview of the final algorithm.

5.1 Preparation of the Required Fields

Not all quantities required by a receiving solver are directly available from the sending application. They must therefore be computed before or after being transmitted, depending on how the number of transferred fields can be minimized and the consistency between the individual quantities can be maintained.

The acoustic source term of the acoustics solver (2.84) involves a temporal derivative, which is best computed by the CFD solver to avoid spurious frequencies. Its simplest form consists only of the low Mach number energy source (2.87b):

$$\dot{\omega}_{e,\text{loMa}} = -\overline{c^2} \frac{\partial \bar{\rho}}{\partial t}. \quad (5.1)$$

In the above expression, the speed of sound $\overline{c^2}$ is not directly accessible due to the averaging and must be approximated:

$$\overline{c^2} = \overline{\gamma R_s T} \approx \bar{\gamma} \bar{R}_s \bar{T}.$$

All three values, $\bar{\gamma}$, \bar{R}_s and \bar{T} are read from the chemistry table and consequently only depend on the progress variable \tilde{C} and the mixture fraction \tilde{Z} , $\overline{Z'^2}$. With the ATF technique, the error associated to this approximation is negligible, since the subgrid parts vanish in a fully resolved flame, i.e. $\bar{q} = q$. In addition to the transferred flow velocities, the density and the source term, the APE operator also involves the instantaneous speed of sound. In order to avoid transferring an additional field, it is computed from the density field $\bar{\rho}$, received from the CFD:

$$\overline{c_{\text{CAA}}^2} \approx \gamma \frac{p^{\text{static}}}{\bar{\rho}}. \quad (5.2)$$

This approximation involves the static pressure p^{static} , which is also inherent to the chemistry table and a constant heat capacity ratio γ . In the CAA, both quantities are prescribed a priori.

5.2 Data Transfer

For the transfer of field data, the coupling layer uses the external CWIPI library² [112], which is part of the OpenPALM coupler [14, 20]. CWIPI is an open source

² CWIPI: Coupling With Interpolation Parallel Interface

software package, which enables coupling of multiple applications by using a decentralized communication pattern based on the MPI standard³ [93]. It has shown to provide excellent performance [29] and has been applied to a wide range of multi-physics problems [70, 69, 73, 77]. Besides support for cell- and vertex centered finite volume discretizations, it features a discretization-independent implementation, which is particularly important for interfacing with the spectral/hp element method discretization of the CAA.

Both solvers are parallelized via domain decomposition, i.e. split their respective computational domains into subdomains which are then handled by instances of the solver. This causes the subdomains of the individual solver instances to differ when transferring data. Moreover, the two solvers may operate on non-congruent computational domains. Hence, field values are not necessarily available at every location, where a receiving solver may request them. Consequently, CWIPI is not only used for transferring the field data over MPI, but also to manage this data transfer and determine whether a quantity requested at a specific location is available. If not, the receiver is notified, so that the missing data can be extrapolated or replaced with a default value, depending on what is most appropriate for this quantity, configuration, location, etc.

5.3 Spatial Representation

For the coupling, the finite volume CFD fields must be represented by means of the spectral/hp element discretization of the CAA and vice versa. While this process poses several difficulties in the forward coupling, it simplifies the backward coupling considerably. When representing the large scale CAA fields in the high-resolution CFD discretization, the CAA field can be directly evaluated at the cell centers of the CFD mesh without special treatment. This is facilitated by the spectral/hp element method, which allows for obtaining exact values of the discrete solution at every point in the computational domain, by simply evaluating the expansion, i.e. performing a backward transform (3.13).

5.3.1 Forward Coupling

For similar length scales, the representation of the flow field within the CAA solver is accomplished by the forward transform (3.38), which evaluates the flow fields at the quadrature points of the expansion. However, the considerably smaller length scales of the CFD field give rise to three major issues during this procedure:

³ MPI: Message Passing Interface

Aliasing Error: A direct evaluation of the short length scale CFD field at the coarser quadrature points ξ_{ijk} introduces spurious lower frequencies.

Non-smooth CFD Fields: The error associated to the forward transform is governed by the smoothness of the transformed field $q(\mathbf{x})$ with regard to the number of quadrature points Q [62]. Hence, the discrepancy between the CFD length scales and the coarser quadrature points of the CAA expansion leads to excessive errors. Among others, this diminishes the conservativeness of the interpolation and causes artifacts in the received fields.

Discontinuous Base Fields: The steep gradients of the CFD fields (e.g. in the flame front) cause strong discontinuities of the base flow quantities $\tilde{\mathbf{u}}, \bar{\rho}$ at the element interface, due to the discontinuous projection. This can deteriorate the stability of the CAA.

To mitigate these issues, a three stage coupling strategy, as sketched in Fig. 5.2, was developed. Its core concept is to introduce an *intermediate expansion*, which uses a finer distribution of quadrature points. Initially, the intermediate expansion (yellow) is constructed with identical expansion functions and polynomial order as the original CAA expansion (blue), i.e. $P_{\text{inter}} = P_{\text{CAA}}$. However, it uses a continuous projection and an increased number of quadrature points $Q_{\text{inter}} > Q_{\text{CAA}}$. Subsequently, the CFD field (cf. Fig. 5.2a) is sampled at the quadrature points ξ_{ijk}^{inter} of the intermediate expansion. The data transfer and detection of out-of domain points is accomplished by the CWIPI library as laid out in the preceding section. Once received, the CAA solver can use information provided by CWIPI to replace values at not located points with default or extrapolated values. The resampled CFD field is shown in Fig. 5.2b.

In the next step, a linear, differential low-pass filter [42] with width $\Delta\lambda$ is applied to the received field q^* by solving a differential equation on the intermediate expansion:

$$q^{**} - \frac{1}{k_c^2} \nabla^2 q^{**} = q^* \quad (5.3)$$

with Neumann boundary condition

$$\frac{\partial q^{**}}{\partial x_i} = 0$$

and the cutoff wavenumber

$$k_c = \frac{2\pi}{\Delta\lambda}. \quad (5.4)$$

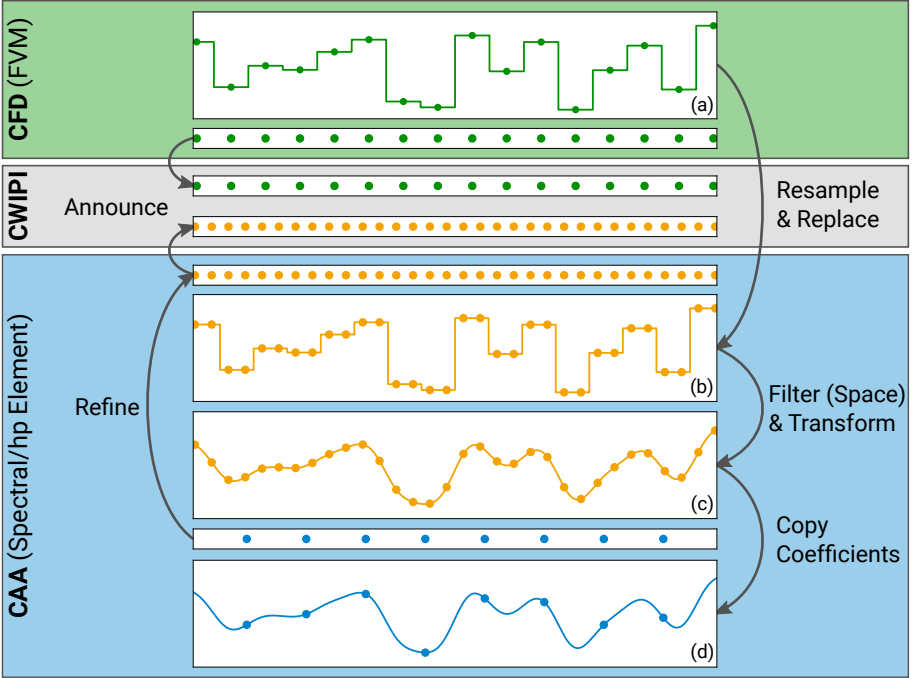


Figure 5.2: Schematic of the three stage coupling strategy. CFD mesh points and fields (a) in green, intermediate expansion quadrature points and fields (b,c) in yellow and CAA expansion quadrature points and fields (d) in blue.

The corresponding elemental weak form is obtained by application of the continuous Galerkin projection:

$$\left(\phi_{stu}, q^{**\delta}\right)_{\Omega_e} - \frac{1}{k_c^2} \left(\phi_{stu}, \nabla^2 q^{**\delta}\right)_{\Omega_e} = \left(\phi_{stu}, q^{*\delta}\right)_{\Omega_e} . \quad (5.5)$$

The right hand side of this equation is computed from the received, discrete node values $q(\xi_{ijk})$ of the intermediate expansion, similar to the right hand side of the forward transform (3.38):

$$\left(\phi_{stu}, q^{**\delta}\right)_{\Omega_e} - \frac{1}{k_c^2} \left(\phi_{stu}, \nabla^2 q^{**\delta}\right)_{\Omega_e} = \left(\phi_{stu}, q^*(\xi_{ijk})\right)_{\Omega_e} . \quad (5.6)$$

Solving this equation yields the spectral representation of the filtered CFD field q^{**} in terms of the expansion coefficients \check{q}^{**} of the intermediate expansion. For

illustration, a filtered, physical field q^{**} is depicted in Fig. 5.2c. Due to the identical expansion functions, the coefficients can be copied into the CAA expansion, where a backward transform yields a smooth physical representation of the CFD fields. The resulting field, shown in Fig. 5.2d, is suitable for computing the RHS of the discretized APE in Eq. (3.80) or as input data for a temporal interpolation.

The three stage coupling strategy avoids spurious frequencies and ensures conservativeness and stability, by mitigating the three major issues identified above. In the following, each of these issues and their mitigation are addressed in more detail.

Aliasing Error

Aliasing errors arise from the right hand side term of the forward transform $(\phi_{stuv}, q^*(\xi))_{\Omega_e}$, when an inadequate quadrature point resolution is used to sample the CFD field [27, 46]. This is mitigated by the denser quadrature point distribution of the intermediate expansion Q_{inter} , which can be freely adjusted without negative implications for the memory consumption and computational efficiency of the solution of the governing equations.

Non-smooth CFD Fields

The second error arises from the left hand side of the forward transform, since the polynomial order of the CAA expansion P_{CAA} does not allow for a sufficient resolution of the CFD field. Therefore, the regular forward transform (3.38) would produce nonphysical, short length scale artifacts [46]. This cannot be mitigated by a higher number of quadrature points of the intermediate expansion, since it is related to the resolution in modal space, which is identical for both expansions. Consequently, the problematic small scale features are removed a priori by application of the differential low-pass filter, Eq. (5.3).

To illustrate its effect, the corresponding differential equation (5.3) can be rewritten as the convolution operation

$$q^{**}(\mathbf{x}) = \int \mathcal{G}(\mathbf{x} - \mathbf{r}) q^*(\mathbf{x}) d\mathbf{r} , \quad (5.7)$$

wherein the Green function [42] of the differential equation (5.3)

$$\mathcal{G}(\mathbf{x}) = \frac{k_c^2}{4\pi} \frac{\exp(-k_c |\mathbf{x}|)}{|\mathbf{x}|} \quad (5.8)$$

acts as smoothing kernel. Its transfer function

$$\mathcal{G}(k) = \frac{1}{1 + k^2/k_c^2} \quad (5.9)$$

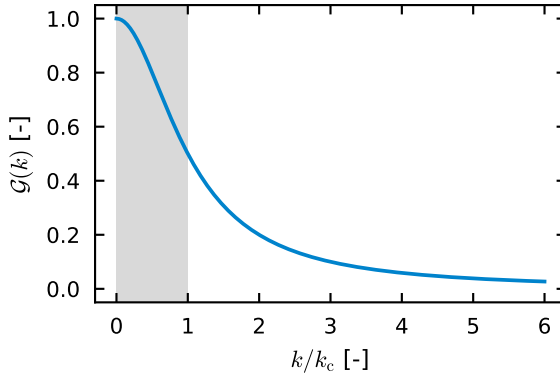


Figure 5.3: Normalized transfer function of the linear differential filter (5.3).

is depicted in Fig. 5.3. Therein, all wave numbers above the cutoff wave number k_c are at least halved. The implementation of the spatial filter as differential equation has several advantages over a direct evaluation of the convolution (5.7), such as a trivial treatment of domain boundaries and small scale ($< \Delta\lambda$) geometry features. For few fields, the implicit treatment is also computationally more efficient. However, the operator is not positive definite due to the negative Laplacian term, and consequently must be treated by a direct solver [3].

Discontinuous Base Fields

The Jacobian-based formulation (2.90), inherent to the Riemann solvers is only defined for the base flow fields being continuous over element interfaces, i.e. $q_L = q_R$. In the CAA expansion, these are represented in a discontinuous Galerkin projection. Accordingly, this assumption only holds for smooth base flow fields, that lie within the polynomial space of the expansion. However, this does not necessarily apply to the steep gradients that occur e.g. in the flame region. This leads to significant discontinuities, which render the internal and numerical fluxes incompatible and therefore deteriorate the stability of the CAA. By performing the forward transform on the intermediate expansion, this issue is circumvented. Its continuous projection enforces continuity and therefore minimizes the inter-elemental discontinuities of the base flow fields in the discontinuous CAA expansion. Thereby, the validity of the Jacobian-based formulation (2.90) is ensured, even for strong gradients.

It is worth mentioning that the (local) Lax-Friedrichs flux, described in section 3.2.1, is not affected by this issue. It does not rely on the characteristic formulation

of the APE-equations, but only involves the left- and right hand side fluxes, as well as the maximum absolute eigenvalue $\|\Lambda_n\|_{\max}$. The latter is estimated from the largest value of both sides of the interface and is therefore sufficient.

5.4 Temporal Interpolation

Forward Coupling

The different time scales of CFD and CAA imply that more than one CAA time step is carried out during a single CFD time step. During forward coupling, this would entail abruptly updating the CAA base flow field after every CFD time step. Such strong temporal variations are, however, not compatible with the APE, which are derived for steady base flows. Consequently, these variations are minimized by a linear interpolation, that blends the recently q^{**n} and Δn CAA steps earlier received fields $q^{**n-\Delta n}$:

$$q^n = \alpha q^{**n} + (1 - \alpha) q^{**n-\Delta n} \quad (5.10)$$

where

$$\alpha = \frac{(\Delta n + 1)\Delta t_{\text{CAA}}}{\Delta t_{\text{CFD}}} \quad \text{and} \quad \Delta n = n - t_{\text{last}}/\Delta t_{\text{CAA}} .$$

As a side effect, the interpolation causes the CAA to lag $1\Delta t_{\text{CFD}}$ behind the CFD, which is unproblematic in a numerical sense, but has to be taken into account when comparing CFD and CAA fields.

Backward Coupling

With the example feedback mechanism (2.92), only the acoustic pressure p^a must be transferred to the CFD solver, which is directly available from the CAA. Due to the higher temporal resolution of the CAA, the acoustic pressure would require low pass filtering in time in order to avoid aliasing. In combustion noise problems, the maximum frequency resolved by the CAA is, however, well below the Nyquist frequency of the CFD $f_{\text{CFD,lim}} = 1/(2\Delta t_{\text{CFD}})$. Moreover, the spatial low pass filtering of the acoustic source terms during the forward coupling acts as a low pass filter in time for compact sources of length scale $L \ll \Delta\lambda$ [138]. Hereby, frequency components above $f = c/\Delta\lambda$ can be prevented from being excited by an appropriate choice of the filter width $\Delta\lambda$. For the applications considered in the current work, the backward coupling hence does not require any additional filtering or interpolation.

5.5 Full Coupling Algorithm

The implemented coupling strategy in the CFD and CAA solvers is sketched in Fig. 5.4 for a single CAA time step. As laid out above, multiple CAA time steps are carried out for each CFD time step. Consequently, the CAA implementation distinguishes between exchange steps and normal steps. In the latter case, when $\Delta n < \Delta t_{\text{CFD}}/\Delta t_{\text{CAA}}$, the solver only performs the temporal interpolation according to Eq. (5.10), using the recently and previously received fields, q^{**n} and $q^{**n-\Delta n}$, respectively. In an exchange step, the acoustic pressure perturbation p^a is first evaluated at the CFD mesh cell centers as defined by the backward transform (3.13). The obtained point values are transmitted using CWIPI, as soon as all previously initialized data transmissions in this direction are completed. While the CAA continues, the CFD solver finishes the transfer and calculates the acoustic source term. Just like the CAA, the CFD waits for eventually unfinished transmissions to complete, before the acoustic source term and the base flow fields are sent to the CAA. In the CAA solver, the received fields $q^*(\xi_{ijk})$ are integrated according to the right hand side of Eq. (5.6). Their filtered representation \check{q}^{**} in the coefficient space of the intermediate expansion is obtained from Eq. (5.3). The corresponding coefficients are then backward transformed (3.13) to yield their physical representation in the discontinuous CAA-expansion $q^{**}(\xi_{ijk})$. With this step, the exchange procedure is completed and the received fields can be interpolated in time. At every CAA time level, the speed of sound is approximated from the blended base flow fields according to Eq. (5.2). At last, both solvers commence with the solution procedures laid out in sections 4.4 and 3.5, increment their time levels and proceed with the next time step.

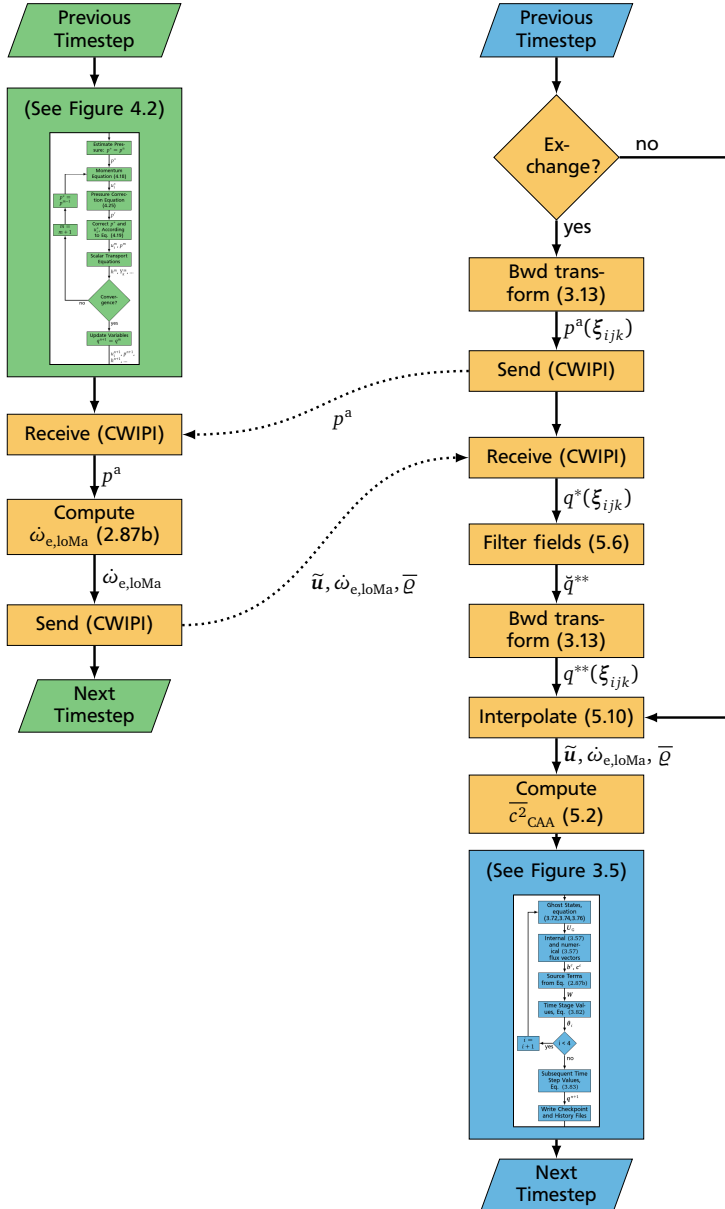


Figure 5.4: Implementation of the coupling algorithm (orange) in the CFD (green) and CAA (blue) solvers.



6 Application to a Half-Dump Combustor

In the present chapter, the developed method is applied to a half-dump combustor in order to assess its general applicability to combustion noise problems and explore different numerical setups. The considered configuration was designed and experimentally investigated by Chakravarthy et al. [21] and features a plenum as well as a rectangular duct with a backward facing step. By virtue of this relatively simple geometry, flow field and acoustic properties, its straightforward numerical treatment alleviates the computational cost of the simulation. This qualifies the configuration to investigate the impact of different CAA and coupling parameters on the predicted combustion noise spectra. Moreover, the low complexity of its flow field and its acoustic properties facilitates a basic validation of the present hybrid CAA approach. To this end, experimental [21] and numerical [68, 66] studies are considered. The focus of this work being the CAA solver and the coupling layer is reflected by the chapter's emphasis on the validation of the acoustic results.

The chapter is structured as follows. After an overview of the considered configuration and the numerical setups of CFD, CAA and coupling, the flow fields obtained from the CFD are briefly reviewed. The chapter commences with a spatial and spectral assessment of the acoustic source term and the acoustic fields. The dominant acoustic modes are investigated and identified by means of a point-wise Fourier transform. Proceeding from the baseline noise spectra, the impact of a variable speed of sound, the number of quadrature points of the intermediate expansion and the coupling's filter width are examined. Moreover, the feasibility of a bi-directional coupling is demonstrated by using an example feedback mechanism. At last, the main findings are summarized and discussed.

6.1 Configuration

A schematic overview of the half-dump combustor geometry is given in Fig. 6.1. Air is introduced at the left hand side through a diverging nozzle and a plenum. From there, it enters the rectangular inlet section of height $d = 30$ mm and width $2d = 60$ mm. The large sectional area jump of this transition acts as acoustically open upstream boundary condition [21]. In the experimental setup, the first part

of the inlet section contains flow-straightening tubes and mesh screens to reduce flow non-uniformities caused by the sudden contraction. These features are not needed and consequently absent in the simulations. The inlet section ends with the backward facing step of height $d = 30$ mm.

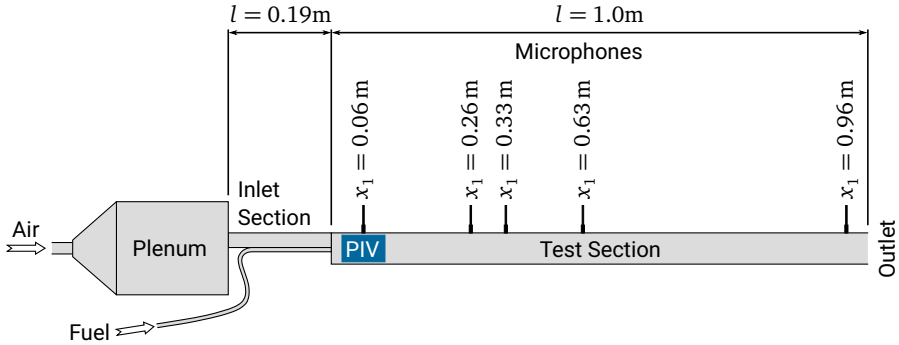


Figure 6.1: Schematic overview of the half-dump combustor geometry with microphone locations and the PIV window (blue) between $0.02 \text{ m} \leq x_1 \leq 0.1 \text{ m}$.

Through a rectangular (4×4 mm) channel, located 1 mm below the step in the center plane of the geometry, methane is introduced and ignited by the hot gases of the recirculation zone, downstream of the step. It thereby stabilizes the flame and caters for mixing of fuel and oxidizer. Five wall mounted transducers, located at the top wall were used in the experiment to perform high frequency pressure measurements. Their axial positions are marked in Fig. 6.1. The test section is terminated by a simple outlet, which again acts as acoustically open boundary condition due to the sectional area jump.

Chakravarthy et al. [21] investigated a wide range of operating points with varying mass flows and different geometries. Two of these operating points were numerically studied in [68], a thermoacoustic stable and an unstable one. For this work, only the unstable operating point, with the parameters listed in Tab. 6.1, is considered. Similar to [68], the mass fluxes were set to match the experimental boundary conditions.

Table 6.1: Unstable operating point of the generic combustor in the current simulation.

Air mass flow \dot{m}_{air}	23.78 g/s
Air inlet velocity $\ \mathbf{u}_{\text{air}}\ $	10.83 m/s
Air inlet turbulent kinetic energy k_{air}	100 m ² /s ²
Fuel mass flow \dot{m}_{fuel}	0.084 g/s
Fuel inlet velocity $\ \mathbf{u}_{\text{fuel}}\ $	8 m/s
Fuel inlet turbulent kinetic energy k_{fuel}	50 m ² /s ²
Static pressure p^{static}	101 325 Pa
Inlet temperature T_{in}	294 K

6.2 Numerical Setup

CFD

Non-conforming domains were used for the CFD and CAA simulation, as depicted in Fig. 6.2. To reduce the computational cost, only the first 700 mm of the test section are included in the CFD simulation. This part covers the region where the reaction are included and therefore noise emission predominantly occurs. The CFD domain does not include the upstream plenum. Instead, the inlet section was extended to achieve a uniform flow with fully developed turbulence at the step. Due to this modification, the flow-straightening tubes and mesh screens used in the experiment can be neglected from the simulation.

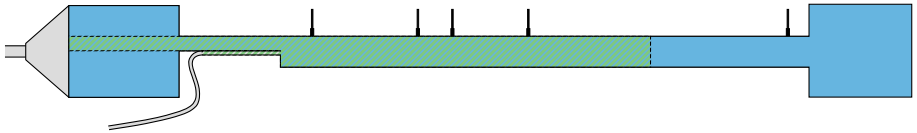


Figure 6.2: CAA (blue) and CFD (green) domains.

For the CFD, a block-structured mesh of 2.9 million hexahedra is used. It is refined around the exit of the fuel inlet, as shown in Fig. 6.3a. All walls are treated as adiabatic with a no-slip boundary condition. Only at the bottom wall

of the inlet section, the near-wall flow field is resolved by the mesh. To obtain the appropriate turbulence levels at the step, the inlet velocities of the air and fuel inlets are modulated as proposed in [65]. The corresponding values for \mathcal{R}_{air} and $\mathcal{R}_{\text{fuel}}$ are given in Tab. 6.1.

The subgrid stress tensor $\tau_{ij}^{\text{sgs},u}$ is modeled according to the Germano procedure, described in section 2.2.2.2 and the combustion is accounted for by the FGM technique. To incorporate chemistry-turbulence interaction, a presumed PDF approach is used, comprising a β -PDF for the mixture fraction and a δ -PDF for the progress variable Y_{CO_2} . The chemistry table is discretized by 25 nodes for mixture fraction and progress variable and 15 nodes for the variance of the mixture fraction. All simulations were run at a time step size of $\Delta t_{\text{CFD}} = 3\text{E}-6\text{ s}$.

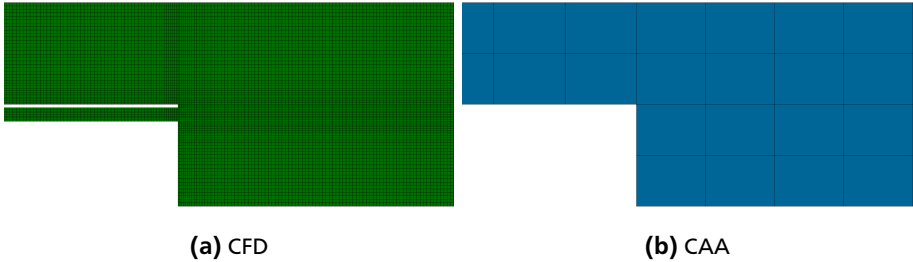


Figure 6.3: Detail of the CFD and CAA meshes in the vicinity of the step.

CAA

As shown in Fig. 6.2, the CAA domain includes the upstream plenum, the test and inlet section and an additional downstream plenum, which accounts for the sectional jump at the outlet. The fuel inlet channel is omitted from the CAA domain, since it is not relevant in the investigated frequency range due to its small dimensions. By virtue of this simplification, the combustor can be discretized by a regular mesh with hexahedra of $h = 20\text{ mm}$ maximum edge length, as shown in Fig. 6.4. Distorted hexahedral elements are only necessary in the up- and downstream plenums, where the largest edge length is below $h = 30\text{ mm}$. In total, the CAA mesh consists of 1850 elements with fourth order polynomials ($P = 4$). With this setup, the expansion is able to maintain an error below 1% for wavelengths down to [95]:

$$\lambda_{\text{min}} > \frac{2 \pi h}{|kh|_{1\%}} = 20.39\text{ mm}, \quad (6.1)$$

where $|kh|_{1\%}(P = 4) = 6.164$ [95]. With $c \approx 340$ m/s upstream of the flame, this translates to frequencies up to $f_{\max} = 11.12$ kHz in the largest elements of the plenums and $f_{\max} = 16.68$ kHz inside the combustor.

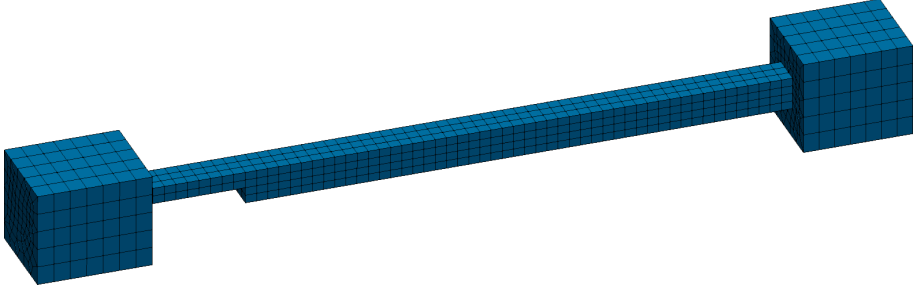


Figure 6.4: CAA mesh.

All walls are modeled as rigid slip walls, according to Eq. (3.72). To avoid transversal eigenmodes, a sponge layer, Eq. (3.78) with a damping coefficient

$$C_{\text{sp}} = -5000 \exp\left(-180E3 \frac{1}{\text{m}^2} r^2\right), \quad (6.2)$$

based on the wall distance r is applied to the walls in the inlet section. The given coefficient distribution reaches $C_{\text{sp}} = -5000$ at the walls, -55.55 at $r = 5$ mm and is less than $1E-14$ at the center line. Non-reflecting farfield boundary conditions are applied at the outward facing plenum walls, without sponge layers being necessary. The very low base flow velocities justify the use of the local Lax-Friedrichs Riemann solver. The fourth order Runge-Kutta scheme is used to account for the temporal discretization with a time step size of $\Delta t_{\text{CAA}} = 1/10 \Delta t_{\text{CFD}} = 3E-7$ s.

Coupling

The instantaneous base flow quantities $\tilde{\mathbf{u}}$, $\bar{\rho}$ and $\dot{\omega}_{e,\text{lowMa}}$ are transferred from the CFD to the CAA at every single CFD and every tenth CAA time step. In section 6.7, where bi-directional coupling is used, the acoustic pressure perturbation p^a is transferred into the opposite direction. In the CAA, the speed of sound is estimated from the instantaneous density and the static pressure, using the relation (5.2). As evident from Fig. 6.3, the mesh spacing and therefore the resolvable length scales of the CFD and CAA are vastly different. To avoid aliasing errors, the intermediate expansion is consequently set to use $Q_{\text{inter}} = Q_{\text{CAA}} + 5 = 10$ quadrature points per direction. A filter width of $\Delta\lambda = 20$ mm is chosen, similar to the wavelength resolution of the CAA expansion, to minimize the filtering while ensuring smooth base

flow fields. This filter width corresponds to a cutoff frequency of 17 kHz upstream ($c \approx 340$ m/s) and 46 kHz downstream of the flame ($c \approx 920$ m/s).

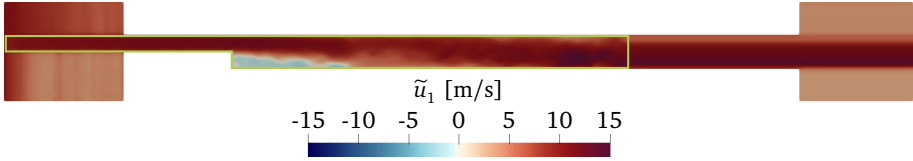


Figure 6.5: Filtered and extrapolated representation of baseflow velocity \tilde{u}_1 within the CAA. Overlapping part of CFD domain highlighted in green. Slice through the $x_3 = 0$ plane.

Due to the non-conforming computational domains, the base flow fields $\tilde{\mathbf{u}}$ and $\bar{\rho}$ are only available from the CAA domain subset that coincides with the CFD, indicated by the green frame in Fig. 6.5. In the remaining parts of the CAA domain, the axial velocity \tilde{u}_1 and the density $\bar{\rho}$ are extrapolated from the nearest available location. The remaining velocities \tilde{u}_2, \tilde{u}_3 and the acoustic source term $\omega_{e,lowMa}$ are set to zero accordingly.

6.3 Flow Fields

The temporal mean axial velocity field $\langle \tilde{u}_1 \rangle$ of the CFD is depicted in Fig. 6.6a. With the employed color scheme, the blue region behind the step marks the recirculation zone. Its smooth boundaries indicate the fluctuating, unstable nature of the flow. As apparent from the mean temperature field in Fig. 6.6b, the recirculated hot gases ignite the mixture in the shear layer, which through thermal expansion, accelerates the flow.

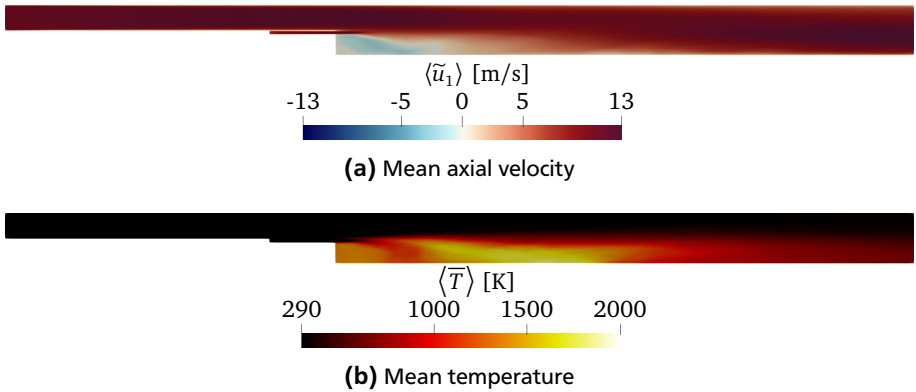


Figure 6.6: Mean axial velocity and temperature fields. Slice through the $x_3 = 0$ plane.

Experimental data is only available in the PIV window depicted in Fig. 6.1 between $x_1 = 20$ mm and $x_1 = 100$ mm. Consequently, the velocity profiles in Fig 6.7 are limited to this region. The agreement of the bulk inlet velocities indicates a sufficiently accurate estimation of the air mass flow. The same assessment applies to the fuel inlet velocity, which similarly conforms with the experiment. However, the widening of the fuel jet is less pronounced in the simulation than in the experiment. This may be caused by insufficient fuel inlet perturbation levels, an increased mixing in the experiment or an insufficient spatial resolution of the PIV. Nevertheless, even the small recirculation velocity is matched very well. The most significant deviations are the slightly higher bulk velocities at $x_1 \geq 60$ mm, the overestimated velocities near the top wall and the lower center line velocities below $x_1 \leq 60$ mm. The overestimation of the bulk velocities is due to the adiabatic walls, which neglect the effect of cooling and therefore the corresponding deceleration of the flow [68]. This also effects the decreased experimental velocities near the upper wall.

The higher center line velocities between $x_1 = 40$ mm and $x_1 = 60$ mm suggest, that the CFD predicts higher temperatures in this region than in the experiment.

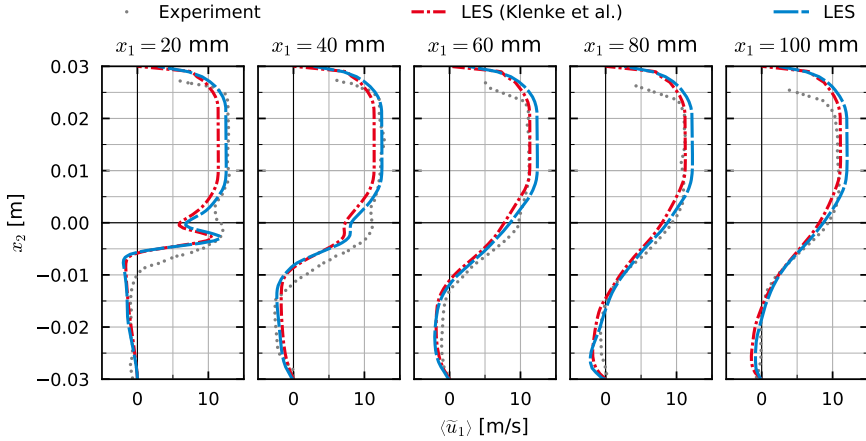


Figure 6.7: Mean velocity profiles at different locations, obtained from PIV measurements, from the simulation published by Klenke et al. [67] and from the current LES-CAA.

6.4 Noise Sources

In Fig. 6.8a, the spatial distribution of the instantaneous acoustic source term $\dot{\omega}_{e,lowMa}$ is shown as it is computed by the CFD. Since it is based on the temporal density change, the noise sources are concentrated around the flame front in the shear layer, where density fluctuations are the largest. Regions of positive and negative source term values alternate, while their magnitude reaches a maximum behind the recirculation zone. Further downstream, the values quickly decrease and eventually tend towards zero at the end of the domain. The filtered and re-sampled CAA representation of the acoustic source term is shown below in Fig. 6.8b. Smaller structures, which were clearly distinguishable in the CFD field are now replaced with large, smooth structures due to the spatial low pass filter of $\Delta\lambda = 20$ mm. For the same reason, the peak values are decreased by about one magnitude, so that the integral source term is preserved.

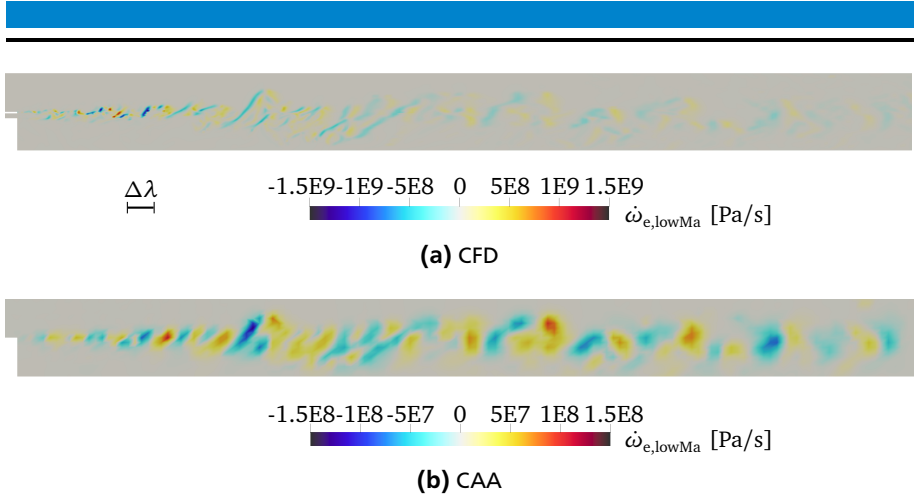


Figure 6.8: Instantaneous acoustic source term as represented in CFD and CAA using different scales. Slice through the $x_3 = 0$ plane.

To quantify the spectral distribution of the acoustic source term, the spectrum of the integral density fluctuation,

$$\Upsilon(f) = \mathcal{F} \left\{ \int_{\Omega} \frac{\partial \bar{\rho}}{\partial t} d\Omega \right\} \quad (6.3)$$

is considered, where \mathcal{F} denotes the discrete Fourier Transform. The volume integral in the above equation can be reduced to the surface integral

$$\Upsilon(f) = \mathcal{F} \left\{ \int_{S_{\text{out}}} (\bar{\rho} \tilde{\mathbf{u}} \cdot \mathbf{n})_{\text{out}} dS_{\text{out}} + \int_{S_{\text{in}}} (\bar{\rho} \tilde{\mathbf{u}} \cdot \mathbf{n})_{\text{in}} dS_{\text{in}} \right\}, \quad (6.4)$$

over the in- and outlets. This expression is mathematically equivalent, but can be evaluated more efficiently. It is worth mentioning that the integral density fluctuation differs from the noise source $\dot{\omega}_{e,\text{lowMa}} = -c^2 \frac{\partial \bar{\rho}}{\partial t}$, because it neglects phase shifts and fluctuations of the speed of sound. Nevertheless, it was shown by Ullrich et al. [136], that Υ holds sufficient information to reconstruct the noise spectra and hence qualifies as global measure for the source term spectra.

The resulting spectral distribution of the integral acoustic source term is given in Fig. 6.9. Its most notable feature is the absence of any individual peaks. This broadband character is typical for combustion noise and in line with the literature [28]. It follows from the broadband noise sources, that possible noise minima

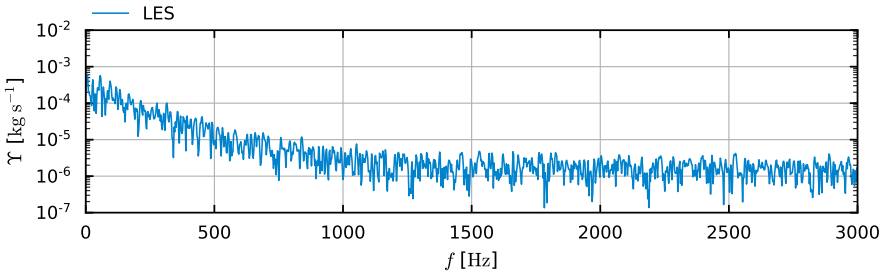


Figure 6.9: Spectrum of the integral acoustic source term $\Upsilon(f)$.

and maxima observed at individual frequencies are the exclusive consequence of acoustic amplification and damping. Moreover, the source term amplitudes show a decrease by two magnitudes from 100 Hz to 1000 Hz. This suggests that for this configuration, no relevant combustion noise is to be expected in the frequency range above 1 kHz. This observation also corresponds with previous studies of this setup [68, 67].

6.5 Acoustic Fields

An exemplary, instantaneous acoustic pressure field, obtained from the CAA is shown in Fig. 6.10. Individual sound waves are only visible in the downstream section of the duct and the attached plenum. In the vicinity of the step, where the majority of the acoustic excitation takes place, numerous reflected waves are superimposed and therefore not distinguishable. Moreover, areas of higher temperatures, downstream of the flame front are characterized by higher amplitudes due to the acoustic impedance of the medium. The lowest amplitudes are located in the plenums, as result of the sectional area jump.

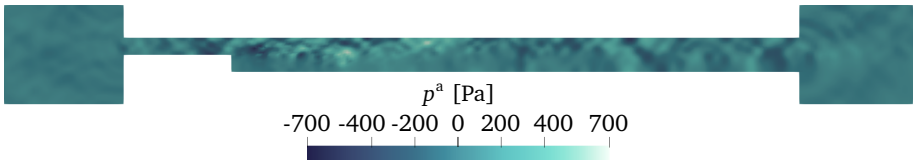


Figure 6.10: Instantaneous acoustic pressure field. Slice through the $x_3 = 0$ plane.

The acoustic pressure was recorded at the microphone positions of the experimental setup over the simulation time of $t = 0.298$ s, treated with a Hamming window and Fourier transformed. Together with the experimental data, the obtained noise spectra are shown in Fig. 6.11. Due to the large wave lengths in the considered frequency range, eventually excited acoustic modes span over the entire domain and are therefore detected at every microphone location. Consequently, the difference between the spectra at the individual microphone locations is minimal in both, the experiment and the simulation. In the experimental spectrum, a wide frequency peak can be observed at $f \approx 140$ Hz, which was similarly recovered by the simulation regarding its shape and peak frequency. However, the amplitudes of the simulation were expected to be significantly smaller than in the experiment, since the current operating point is characterized by thermoacoustic instabilities which cannot be captured with the employed uni-directional coupling.

Notwithstanding, the correspondence of peak frequencies and shape improves into axial direction, where the peaks frequencies slightly shift towards lower values. However, a small frequency offset of $\Delta f \approx 10$ Hz can still be observed, which is likely due to the increased temperature levels in the simulation, caused by the neglected heat flux through the walls. Besides the $f \approx 140$ Hz peak, the simulation yields an additional peak at $f \approx 320$ Hz, possibly due to neglected damping terms of the APE. To shed more light on the origin of this frequency peak, the acoustic modes associated to each frequency peak are identified in the following. To this end, the acoustic pressure field is Fourier transformed to obtain the complex amplitudes at every quadrature point for each frequency

$$\hat{p}^a(\mathbf{x}, f) = \mathcal{F}\{p^a(\mathbf{x}, t)\} . \quad (6.5)$$

From this data, the phase shift φ_{\max} that gives the largest real amplitude is determined for each peak frequency f_{peak} . The corresponding, normalized pressure amplitude distribution is then computed as:

$$K_{p^a}(\mathbf{x}) = \frac{\Re\{\hat{p}^a(\mathbf{x}, f_{\text{peak}}) e^{i\varphi_{\max}}\}}{\left\|\Re\{\hat{p}^a(\mathbf{x}, f_{\text{peak}}) e^{i\varphi_{\max}}\}\right\|_{\infty}} \quad (6.6)$$

and depicted for two peak frequencies in Fig. 6.12.

The visualization of the individual modes in Fig. 6.12 suggests that the $f \approx 140$ Hz peak is associated to the $\lambda/2$ eigenmode of the full combustor domain ($l = 1.19$ m). Similarly, Fig. 6.12b implies a correlation between the observed $f \approx 320$ Hz peak and the λ eigenmode. It is worth mentioning that from the point wise Fourier transform, these two eigenmodes were not found exclusively for the depicted frequencies, but for a range of frequencies. This is caused by the transient

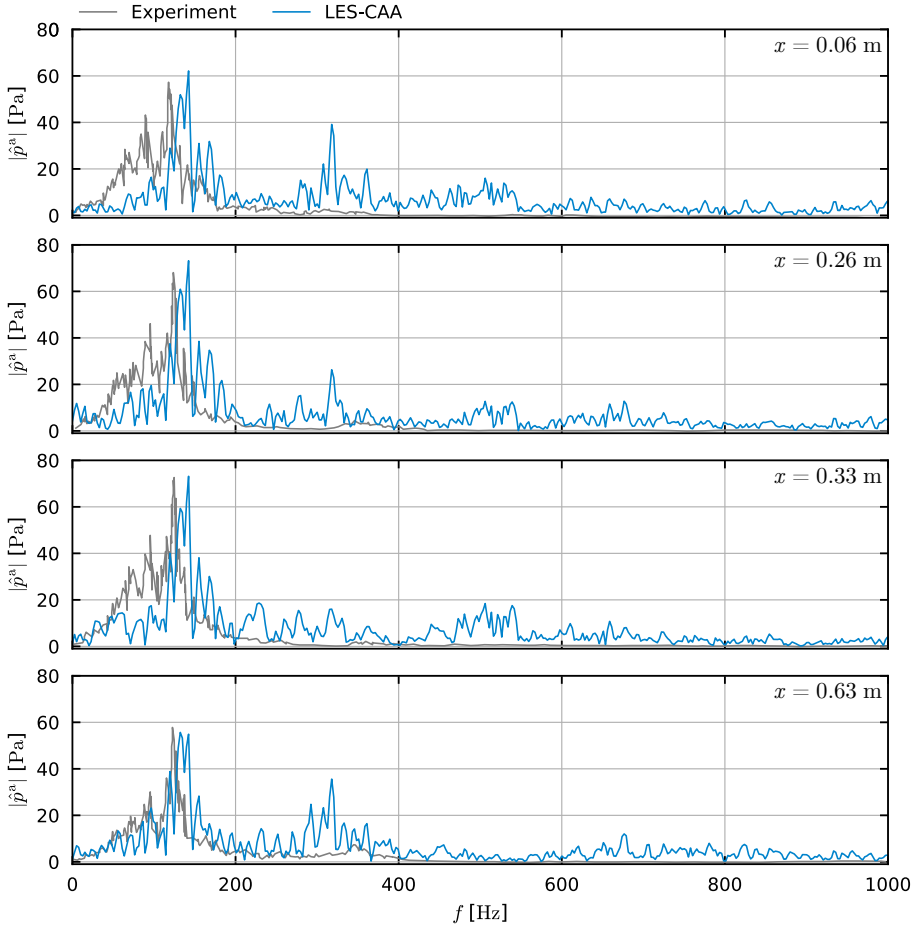


Figure 6.11: Noise Spectra at different microphone locations obtained from the experiments and the current simulation.

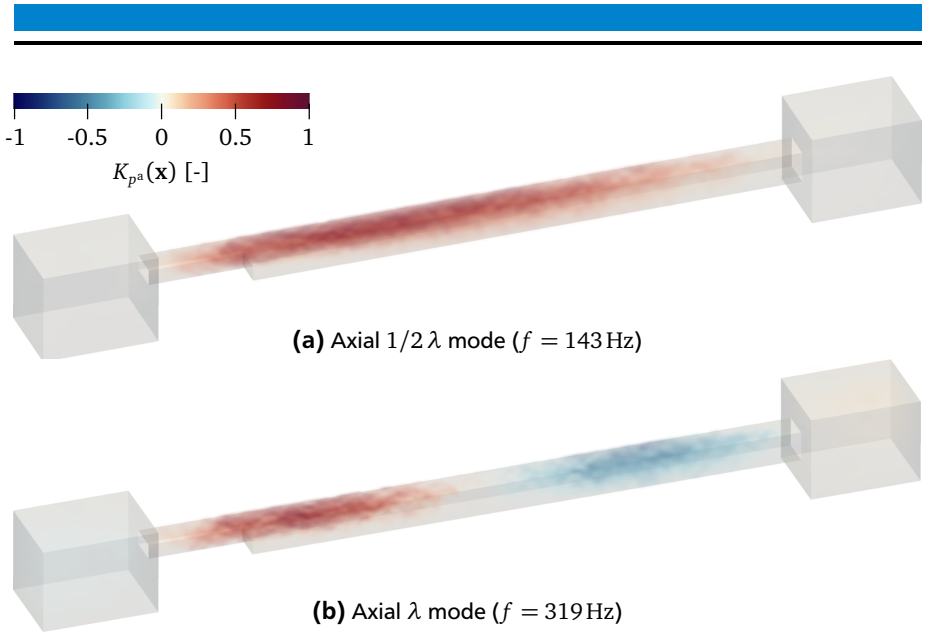


Figure 6.12: Normalized acoustic pressure amplitude $K_{pa}(\mathbf{x})$ at the phase that corresponds to the largest amplitudes for two eigenmodes.

movement of the flame and the continuous oscillation of the speed of sound which, goes along with this. The wide shape of the frequency peaks in the noise spectra depicted in Fig. 6.11 is consequently attributed to this transient behavior.

In addition to the experimental measurements, reference data from a hybrid CAA simulation by Klenke [66] is available. Similar to the current method, the respective simulation relied on the PRECISE-UNS CFD solver, used an identical CFD mesh and similar combustion modeling, turbulence modeling and inlet conditions. As evident from the corresponding axial mean velocities, depicted in Fig. 6.7, the resulting CFD fields are very similar to the current simulation. Deviations between the acoustic fields are hence almost exclusively due to differences in the coupling layer and the CAA. In [66], the Linearized Euler Equations based PIANO acoustics solver was used. The code is developed by the German Aerospace Center DLR, employs the finite differences method and is designed to solve external aeroacoustic problems. It therefore does not account for complex geometries or varying base flow fields. Hence, a constant base flow density $\bar{\rho}(\mathbf{x}, t) = \text{const.}$, pressure $\bar{p}(\mathbf{x}, t) = \text{const.}$ and velocities $\bar{\mathbf{u}}(\mathbf{x}, t) = \langle \tilde{\mathbf{u}} \rangle(\mathbf{x})$ were prescribed. Unlike

the current simulation, the CAA had to be stabilized by spatial filtering and artificial damping spots [67].

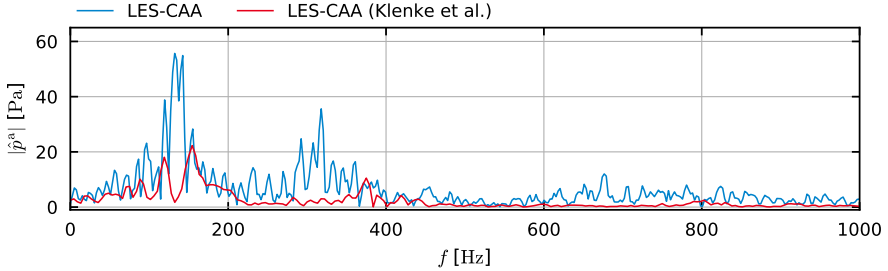


Figure 6.13: Noise Spectra at $x_1 = 0.63$ m obtained from the experiments, the current simulation and from the simulation published by Klenke et al. [67].

The corresponding acoustic pressure spectra are depicted in Fig. 6.13. The FDM based simulation exhibits a lower frequency resolution due to a shorter simulation time, but similar to the current simulation, predicts two major frequency peaks. The first peak frequency of 140 Hz is in agreement with the current simulation and likely related to the $1/2\lambda$ mode, while the 320 Hz peak of the λ mode is shifted by $\Delta f \approx 55$ Hz towards higher frequencies. The peak amplitudes are reduced by a factor of at least 50 %, possibly due to the employed artificial damping. Moreover, the LEE include an extra term, which takes additional damping effects, e.g. by density gradients into account, that also may cause the generally lower amplitudes. Nevertheless, they still predict the excitation of the λ mode. Its attenuation must consequently be caused by a different effect, that is not accounted for by either of the two hybrid CAA methods, such as non-linear acoustic effects.

6.6 Sampling Resolution and Filter Width

To further explore the effect of the filter width $\Delta\lambda$ and the number of quadrature points of the intermediate expansion Q_{inter} , both parameters were varied towards presumably greater errors. An increased filter width applied to the base flow fields $\tilde{\mathbf{u}}$ and $\bar{\rho}$, results in smoother velocity and density gradients, but has no significant impact on the noise spectra, as evident from Fig. 6.14. Only at the 140 Hz peak, a small frequency shift towards higher values can be observed, which increases with the filter width. This is caused by a slight temperature increase in the relevant path of the corresponding acoustic mode in the upper half of the channel. The

smoother gradients of $\tilde{\mathbf{u}}$ and $\bar{\rho}$ however, do not impact the acoustic properties of the combustor.

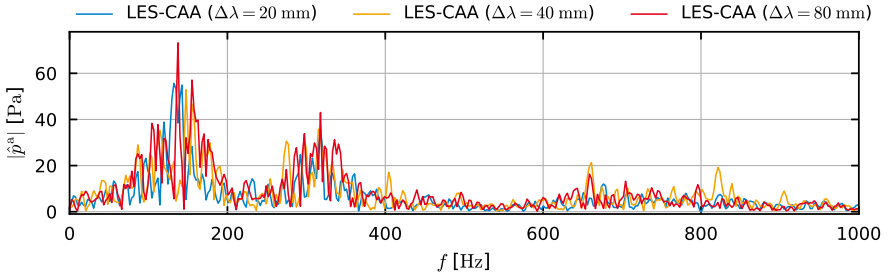


Figure 6.14: Noise Spectra at $x_1 = 0.63$ m obtained from the LES-CAA at different filter widths for $\tilde{\mathbf{u}}$ and $\bar{\rho}$.

A decreased CFD field sampling resolution has more severe effects on the noise spectra, as seen from Fig. 6.15. Over the entire frequency range, the decrease of Q_{int} causes increased noise levels, due to aliasing effects of the acoustic source term. Consequently, this noise is amplified at the eigenfrequencies, leading to significantly larger amplitudes.

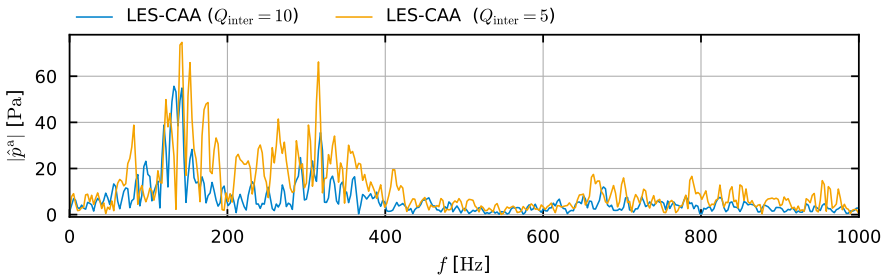


Figure 6.15: Noise Spectra at $x_1 = 0.63$ m obtained from the LES-CAA with and without oversampling.

6.7 Acoustic Feedback

All previous results were obtained with uni-directional coupling from CFD to CAA, so that the effect of the acoustics onto the combustion was not considered. As laid out in section 2.4.4, the modeling of the acoustic feedback mechanisms is beyond the scope of the current work. Notwithstanding, the feasibility of the bi-directional coupling shall be demonstrated by means of the example feedback formulation (2.92) as proposed by Klenke et al. [67]. To this end, the instantaneous acoustic pressure field p^a is transferred from the CAA to the CFD and introduced into the momentum equation via an acoustic pressure gradient.

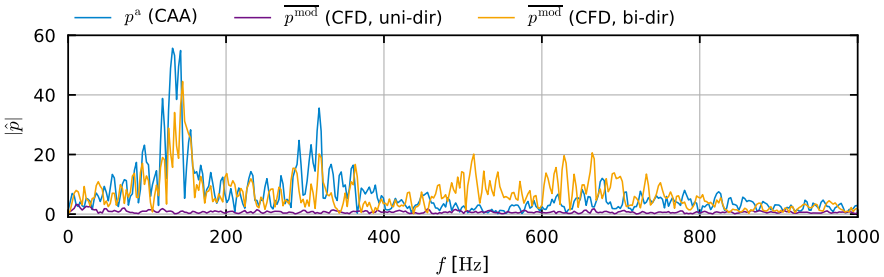


Figure 6.16: Spectra of acoustic pressure p^a from CAA and modified hydrodynamic pressure p^{mod} from CFD, using uni-directional coupling and bi-directional coupling at $x_1 = 0.63$ m.

As evident from Fig. 6.16, the hydrodynamic pressure fluctuations in the CFD are minuscule with uni-directional coupling. However, with bi-directional coupling, the fluctuations of the acoustic pressure are clearly distinguishable in the hydrodynamic pressure spectrum. In this case, both peaks are visible in the CFD, with negligible frequency offset and slightly smaller amplitudes, demonstrating the capability of the coupling layer. Besides the pressure fluctuations, the feedback formulations only has a negligible effect on the velocities and the combustion, leading to identical flow fields and noise spectra.

6.8 Summary

The developed hybrid CAA method was applied to a simple half-dump combustor in order to assess its general applicability to enclosed configurations and combustion noise problems in particular. To this end, a single operating point was considered,

that has also been covered in two similar numerical studies [68, 67]. A comparison of the obtained flow fields showed good agreement between the two simulation results and the experiment. The only significant deviation was a higher temperature level downstream of the flame due to an adiabatic treatment of the walls in the simulations. A review of the spatial distribution of the acoustic source term showed that the major noise sources are of very short length scale and located at the flame front. This scale discrepancy was successfully bridged by the coupling layer, so that a very coarse CAA discretization could be employed. In frequency domain, the acoustic source term was found to span a broad frequency range without significant peaks, but to decrease by two magnitudes below 1 kHz.

The resulting noise spectra exhibit two major frequency peaks at $f \approx 140\text{Hz}$ and $f \approx 320\text{Hz}$. Based on a point-wise Fourier Transform, the acoustic modes associated to the observed frequency peaks were identified as the $\lambda/2$ and the λ eigenmodes of the combustor. The first peak was also observed in the experiment and conforms with the simulation results in terms of peak frequency and shape. The prediction of a second peak is consistent with a previous study [67], which employed the LEE equations and a FDM discretization, hinting that it may be related to simplifications in both acoustic governing equations. Regarding the parameters of the coupling layer, its filter width was found to have negligible impact on the noise spectra, while a coarser quadrature point distribution of the intermediate expansion resulted in increased noise levels. Finally, the feasibility of the backward coupling was demonstrated by means of a bi-directional coupled simulation, where the frequency peaks of the acoustic pressure were successfully recovered in the hydrodynamic pressure of the CFD.



7 Application to a Swirl Stabilized Burner

The key feature of the developed hybrid CAA method over existing approaches is its applicability to complex, enclosed geometries with non-uniform temperatures and transient base flow fields. In this chapter, this capability will be used to investigate the thermoacoustic properties of a swirl stabilized burner. Parts of this study have been published in [74]. The considered configuration features the CESAM-HP¹ test rig, which was designed by EM2C laboratory of CNRS Paris [89], to investigate combustion noise and thermoacoustic instabilities. It comprises a swirler, a premixing duct, a combustion chamber and a convergent-divergent nozzle. In terms of complexity, it thereby marks an intermediate step between the previously explored, simple half-dump combustor and industry scale combustion systems. Notwithstanding, it exhibits most phenomena relevant to combustion noise, such as pressurized operating conditions, a swirl stabilized, premixed flame with an inclination towards instabilities and an outlet nozzle that facilitates indirect combustion noise.

Due to its complex, three-dimensional geometrical features, the current burner is beyond the capabilities of most conventional, block structured CAA tools, making it a suitable subject for the assessment of the current spectral/hp element based approach. For the considered configuration, a wealth of reference data is available from experiments and different simulation approaches with varying degree of abstraction. In addition to an experimental study by EM2C [89], the setup was subject to investigations involving a high fidelity compressible LES [54], a hybrid approach that comprises RANS CFD and frequency domain CAA simulations [136] and a linear network model [135].

The results obtained with the frequency-domain, hybrid CAA method are of particular interest, as it is conceptually closest to the present work. It was developed by TU-Munich [45] and is based on solving the acoustic governing equations on a stationary mean flow field. Accordingly, the design cannot account for thermoacoustic instabilities and the acoustic source term has to be modeled [49]. The procedure was recently improved by computing the noise sources from the integral spectra of the density fluctuations $\partial \rho / \partial t$, obtained from a reactive, low Mach number LES

¹ CESAMP-HP: (French) Combustion Étagée Swirlée Acoustiquement Matrisée-High Pressure

simulation [136]. Consequently, the most prominent differences are related to the CAA solver, which uses the LNSE or Helmholtz equations instead of the APE, operates in frequency domain and relies on constant RANS or time averaged LES base flow fields.

For the investigated CESAM-HP test rig, the spectra obtained with this improved frequency domain LES-CAA method showed excellent agreement with the experimental data [135]. The underlying low Mach number LES was conducted using the identical CFD solver, numerical mesh, simulation parameters and checkpoint file, as in the current work. In the following, the LES results from [136] are referred to as *original LES*, while for the present LES, the term *current LES* is used. Due to the promising results, the assumptions inherent to the choice of boundary conditions in the current work are identical to those of the frequency domain simulation. Because of the similarity of its concept, boundary conditions and underlying LES simulation, the frequency domain LES-CAA simulation serves as primary reference for the assessment of the current method. Comparisons based on this approach eliminate most influences of the CFD, such as the turbulence and combustion modeling, or the mesh resolutions. Therefore, they allow focusing on the coupling method and the CAA solver, which are the main subjects of this work.

The chapter begins with an overview of the CESAM-HP test rig and the two investigated operating points, together with the numerical setups for CFD, CAA and coupling layer. As no detailed description of the flow fields is available in literature, this topic is covered more extensively. Following a qualitative and quantitative overview of the acoustic source term, the dominant acoustic modes of the configuration are identified, using multiple sampling locations and a point-wise Fourier transform. Based on these findings, the obtained noise spectra are assessed for both operating points. Finally, the impact of different coupling parameters and the numerical cost of the coupling layer are explored, before a summary of the chapter's main findings is given.

7.1 Configuration

The configuration investigated in the following is based on the CESAM-HP test rig. A full description of its design, as well as the full geometry are given in [89]. The computational domain inherent to this study is depicted in Fig. 7.1. The test bench consists of a premixing duct with swirler, a pressurized chamber and a choked, convergent-divergent nozzle. The swirler is fed by two inlets at equal mass flow rates with the same, lean propane/air mixture. It is connected to the premixing duct by two eccentric ducts that induce the flow with a swirl, that stabilizes the flame. Further upstream, the premixing duct is closed by a piston with a perforated

screen and a center jet. Both, the screen and the jet can be fed individually with air, to further aid the stability of the flame. As laid out in the following section, the feeding lines, the plenum upstream of the perforated screen and the part of the nozzle downstream of the shock have negligible impact on the results and are therefore omitted.

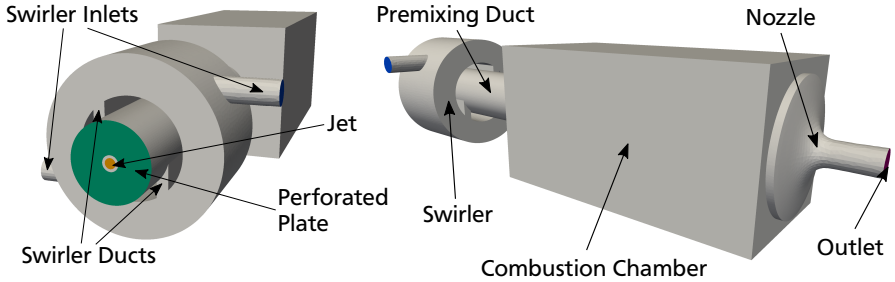


Figure 7.1: Considered geometry of the CESAM-HP test rig.

The two operating points listed in Tab. 7.1 are considered in this work. They only differ in the ratio of jet and swirler air mass flows. None of them features mass flows through the perforated plate, as the corresponding operating points exhibit severe instabilities.

Table 7.1: Investigated operating points of the CESAM-HP test rig.

	OP-16-2	OP-13-5
Swirler air mass flow [g/s]	16	13
Jet air mass flow [g/s]	2	5
Swirler fuel mass flow [g/s]	0.98	
Mean static pressure [Pa]	201664	
Total temperature inlet [K]	313	
Global equivalence ratio [–]	0.85	
Simulation time [s]	0.238	0.122

7.2 Numerical Setup

CFD

For both operating points, the same numerical setup is used. Bulk velocity profiles and a constant temperature are prescribed at the swirler and jet inlets. The deactivated perforated screen and the walls are specified by adiabatic no-slip wall boundary conditions. The subgrid stress tensor $\tau_{ij}^{sgs,u}$ is modeled according to the Germano procedure, described in section 2.2.2.2. With the combustion being accounted for by the FGM model, the ATF technique, laid out in section 2.3.3.2, facilitates sufficient flame resolution. In the chemistry table, 25 nodes were used to discretize the progress variable Y_{CO_2} for 100 mixture fractions, resulting in a total table size of 2500 points.

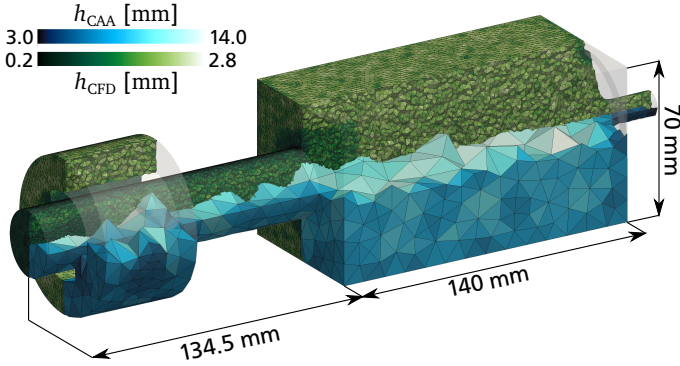


Figure 7.2: Regular tetrahedron equivalent edge length $h = \sqrt[3]{12/\sqrt{2}V}$ for CAA (blue) and CFD (green) meshes.

The domain is discretized by the unstructured mesh depicted in Fig. 7.2. It comprises 1.4 Million tetrahedra and is locally refined at curved edges, the chamber inlet, the jet region and in the front section of the combustion chamber, where the flame is to be expected. In the flame region, a cell size of 1.5 mm is not exceeded. The mesh is not refined near the walls, hence the near-wall flow fields are not resolved by the simulation. The ratio of resolved to total turbulent kinetic energy, depicted in Fig. 7.3, can give insight into the meshes ability to sufficiently resolve the turbulent scales. Therein, the subgrid part of the turbulent kinetic energy, k_{sgs} is estimated after [88, 141]:

$$k_{sgs} = 2C_i \Delta h_{filt}^2 \left\| \langle S_{ij} \rangle \right\|^2, \quad (7.1)$$

where $C_i = 0.202$ and $\Delta h_{\text{filt}} \approx \sqrt[3]{12/\sqrt{2}V}$. According to the Pope criterion [110], at least 80% of the turbulent kinetic energy should be resolved by the simulation. This is achieved in most parts of the domain. The only exception are the swirlers, where the turbulence is not yet fully developed and therefore both, k_{sgs} and k_{res} are close to zero.

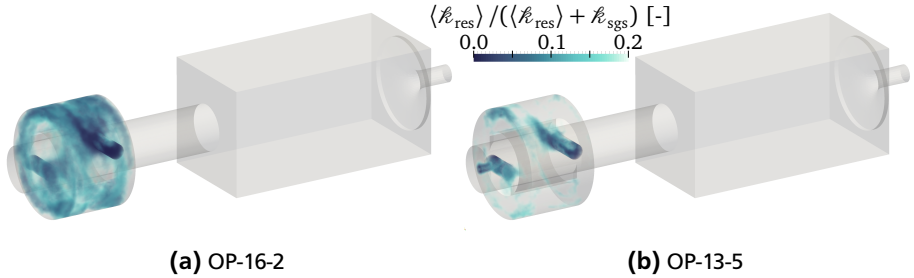


Figure 7.3: Instantaneous ratio of resolved to total turbulent kinetic energy for OP-13-5 and OP-16-2.

Like the pope criterion for the turbulence, the thickening factor \mathcal{F} , depicted in Fig. 7.4, can give insight into amount of modeling inherent to the combustion. In most parts of the domain and at most time steps, the factor is well below 10 and only rarely reaches higher values, suggesting that the flame is sufficiently resolved.

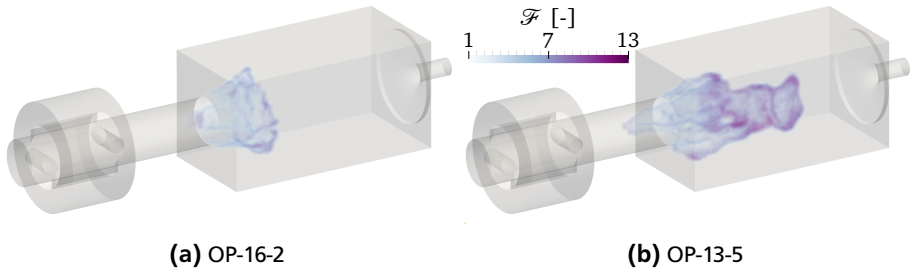


Figure 7.4: Instantaneous Thickening Factor for OP-13-5 and OP-16-2.

The setup exhibits an inclination towards flashback in the experiment [89] as well as in high fidelity LES simulations [54, 75]. These flashbacks occur periodically and only contribute to frequencies well below the considered frequency range. Due to their large time scales, the flashbacks would bring about excessive simulation times required to gather meaningful statistics. Hence, a limiter function was

introduced in the efficiency function \mathcal{E} of the ATF technique, that prevents the flame from propagating into the premixing duct. Thereby, it significantly reduces the computational cost to a practical extent. The flashbacks occur at both operating points, but are of much shorter duration for OP-13-5, allowing the limiter to be disabled. Both simulations were run at a time step size of $\Delta t_{\text{CFD}} = 2.5\text{E}-6$ s, which yields mean Courant numbers below 1.41 in the nozzle, below 0.61 in the jet and less than 0.25 in the remaining duct, swirlers and chamber.

CAA

The CAA is based on the identical computational domain as the CFD and the mesh depicted in Fig. 7.2. It is composed of 6870 tetrahedra of $h_{\text{min}} = 4.5$ mm to $h_{\text{max}} = 14$ mm edge length with a 4th order expansion ($P = 4$). The time step size of $\Delta t_{\text{CAA}} = 2.5\text{E}-8$ s is significantly smaller than in the CFD due to discrepancy of the acoustic time scales.

The shortest resolvable wavelength is estimated as described by Moura et al. [95], using Eq. (6.1), $|kh|_{1\%} = 6.164$ ($P = 4$) and the edge length h_{max} of the largest elements:

$$\lambda_{\text{min}} > \frac{2\pi h_{\text{max}}}{|kh|_{1\%}} = 14.27 \text{ mm}.$$

With a speed of sound of $c = 341$ m/s upstream of the flame, this translates to resolvable frequencies up to 23.90 kHz. Given that for the CESAM-HP test rig, combustion noise is expected to occur below 4 kHz, this means that for the description of the acoustic waves, the CAA resolution is substantially higher than necessary. This discrepancy originates from the relatively small features of the combustor geometry, that are resolved by the computational mesh.

All walls are treated as rigid with Eq. (3.72), the swirler inlets and the nozzle outlet are modeled as non-reflecting boundaries as in Eq. (3.76). While this choice is obvious for the choked nozzle, the feeding line's reflection coefficient is different from zero [89], but was found to have negligible impact on the acoustic behavior of the system in the relevant frequency range [89, 136]. A similar simplification was made for the perforated screen, which can be treated as rigid wall due to its low porosity of 0.05 [136].

Coupling Layer

With a CAA time step size of $\Delta t_{\text{CAA}} = 2.5\text{E}-8$ s and a CFD time step size of $\Delta t_{\text{CFD}} = 2.5\text{E}-6$ s, the base flow fields are exchanged every 100 CAA steps. Similar to section 6.7, the example feedback mechanism had negligible impact for this configuration, so that only results obtained with uni-directional coupling are presented in this chapter. At this, the acoustic source term $\dot{\omega}_{e,\text{IoMa}}$, the instantaneous velocities $\tilde{\mathbf{u}}$,

the density $\bar{\rho}$ and the modified pressure $\overline{p^{\text{mod}}}$ are transferred from the CFD to the CAA. To minimize information loss, the filter width is set to $\Delta\lambda = 12\text{mm}$, slightly below the smallest resolvable wavelength. At $c \approx 341\text{m/s}$, this limits the maximal source term frequencies to 28.42kHz . Due to the relatively fine CAA mesh, the number of quadrature points of the intermediate expansion is identical to the CAA expansion, i.e. $Q_{\text{int}} = Q_{\text{CAA}} = 5$. This is enabled by the ATF technique employed in the CFD, which increases the smallest length scales of the relevant fields beyond the CFD mesh size and therefore the CAA resolution. Since the nozzle is choked and thereby, Mach numbers above 0.3 are reached, the low Mach number formulation of the CFD yields nonphysical base flow field values in this region. This has shown to corrupt the stability of the APE. Hence, for all locations downstream of $\mathbf{x}_{\text{ref}} = [0.135, 0, 0]^T\text{m}$, the acoustic source term is set to zero and all other all received quantities are extrapolated from \mathbf{x}_{ref} in the CAA.

7.3 Flow Fields

Both operating points exhibit very different flow features regarding the behavior of the vortex inside the premixing duct. These bring about specific stability issues, most notably the configuration's inclination towards flashbacks, which was also observed in the experiment and in the compressible high fidelity LES simulations [75, 54].

7.3.1 Operating Point OP-16-2

The mean axial velocity field, shown in Fig. 7.5a is largely dominated by the axial inlet jet and the vortex breakdown in the combustion chamber. The latter is not tied to the center line and therefore performs a tumbling motion around the x_1 -axis. This phenomenon is commonly referred to as *Precessing Vortex Core* (PVC) [18]. This additional rotation is also evident from the axial velocity spectrum in Fig. 7.6. In addition to the $f \approx 318\text{Hz}$ (2000 rad/s) peak, caused by the swirl of the vortex, an additional peak at $f \approx 170\text{Hz}$ (1068 rad/s) can be observed due to the precessing movement of the vortex core.

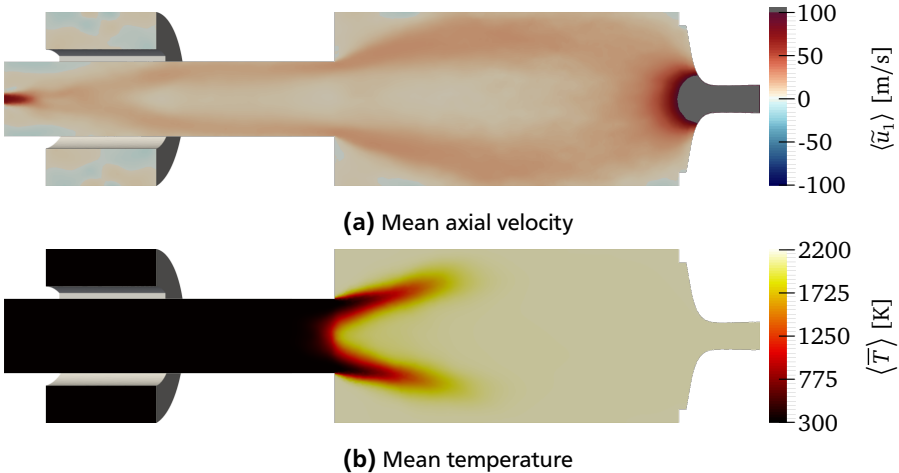


Figure 7.5: Mean axial velocity and temperature fields for OP-16-2 obtained from current LES (slice through the $x_3 = 0$ plane).

In Fig. 7.5a, the axial velocity reaches more than $\tilde{u}_1 = 700\text{ m/s}$ downstream of the combustion chamber and therefore Mach numbers above $Ma = 0.3$. This

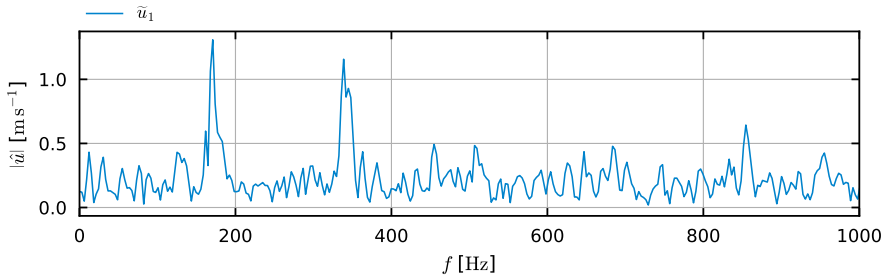


Figure 7.6: Axial velocity spectrum at $\mathbf{x} = [0.01, 0.015, 0]^T$ m for OP-16-2.

violates the low Mach number assumption inherent to the flow governing equations and hence causes the simulation to deliver nonphysical results in this region, but was shown to no effect on the flow field upstream of the nozzle.

The mean temperature field in Fig. 7.5b gives an impression of the flame location. Moreover, the steep gradient indicates very small variations of the flame location. This is caused by an observed higher stability, which is due to the efficiency function limiter described in section 7.2, that prevents the flame from moving upstream of the chamber inlet. It is worth mentioning, that without this artificial constraint, OP-16-2 is likely to be less stable than OP-13-5. In addition to the flame location, the temperature field gives an impression of the mean distribution of the speed of sound. Hence, it determines the flow feature most relevant for the acoustic properties of the configuration.

7.3.2 Operating Point OP-13-5

In contrast to OP-16-2, the mean flow fields of OP-13-5, shown in Fig. 7.7 exhibit a significant asymmetry. This circumstance is due to a large time scale phenomenon, which cannot be captured in a LES simulation at reasonable computational cost. Due to its lack of rotation, the axial jet causes the vortex to split into two branches, located off-center, as shown in Fig. 7.8b. Eventually, one of these branches moves farther away from the center and causes a stronger deflection of the outflow from the corresponding swirler duct. This disturbance imposes an adverse pressure gradient inside the duct, promoting a flow detachment that leads to an imbalance of the duct mass fluxes. Due to the imbalance, the vortex branch is pushed even farther off-center, which further sustains the duct's flow detachment and increases the mass flux imbalance. The result is a circular causality, that causes one of the vortex

branches to lock on to a swirler duct, stopping the precessing movement of the vortex. A prerequisite of this phenomenon is a sufficiently strong jet that facilitates the vortex branching to occur as far downstream as the location of the swirler ducts. As evident from Figs. 7.5a and 7.8a, this condition is not met for OP-16-2, where the jet is resolved further upstream. A similarly asymmetrical flow field was observed in [136].

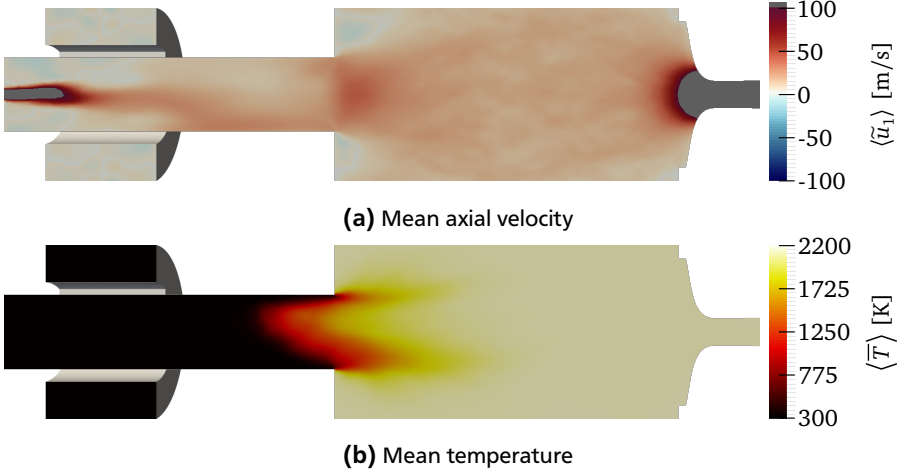


Figure 7.7: Mean axial velocity and temperature fields for OP-13-5 obtained from current LES (slice through the $x_3 = 0$ plane).

Due to the asymmetry of the velocity fields, the mean temperature field, given in Fig. 7.7b is asymmetrical as well. The high temperature region reaches far upstream into the premixing duct, resulting in an earlier acceleration of the flow due to thermal expansion. As a result, the mean axial velocities do not exhibit a recirculation zone on the centerline and are generally higher. Compared to OP-16-2, the temperature gradients in the flame region are much smoother, caused by frequent flashbacks and the resulting strong flame variations. The two extremes, in which the shape and location of the flame varies, are evident from the instantaneous CO mass fraction for two time steps of the same simulation, given in Fig. 7.9. The immense difference between these two attests the unstable character of the configuration, which is subject of a related study [75]. Notwithstanding, the flame immediately retreats into the combustion chamber after every flashback and can therefore be simulated without artificially limiting its location.

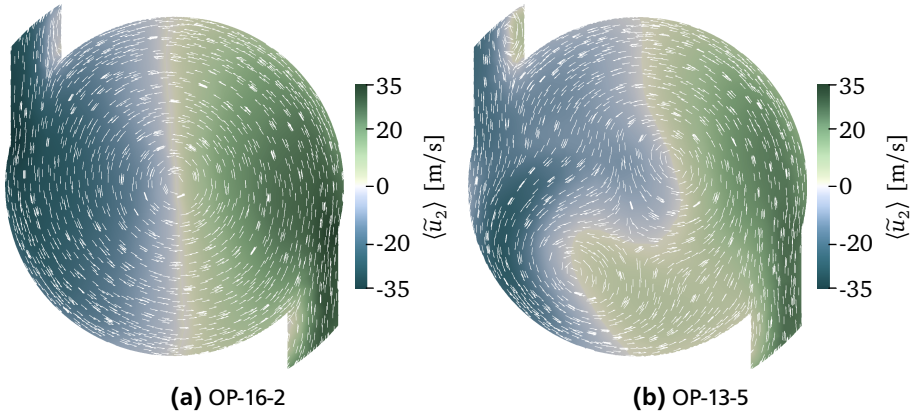


Figure 7.8: Mean vertical velocity $\langle \tilde{u}_2 \rangle$ and directions of the planar mean velocity projection $\langle \tilde{u}_2 \rangle \mathbf{e}_2 + \langle \tilde{u}_3 \rangle \mathbf{e}_3$ inside premixing duct and swirler ducts. Slice through the symmetry plane of the swirler ($x_1 = -95$ mm). Recirculation in the upper channel of OP-13-5 (b).

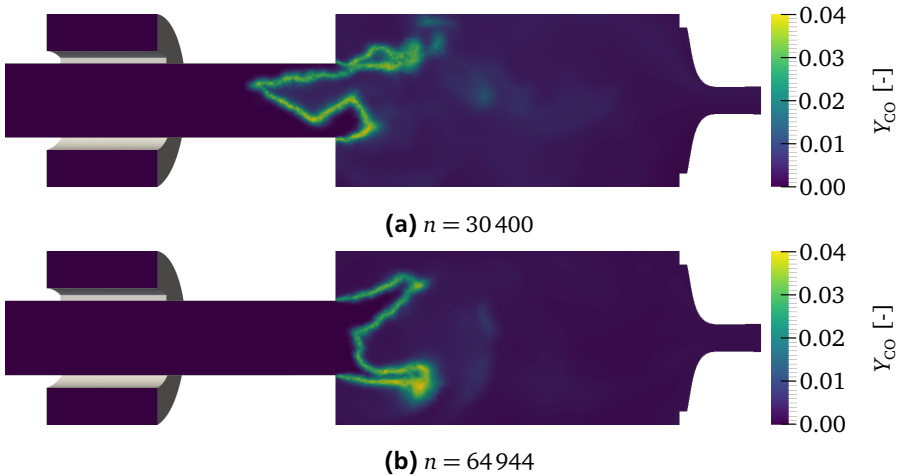


Figure 7.9: Instantaneous CO mass fractions for OP-13-5, 34544 time steps (86.36 ms) apart.

7.4 Noise sources

The instantaneous noise source distribution in terms of absolute, logarithmic values is depicted in Fig. 7.10. In the CFD fields (Fig. 7.10a), the flame location is recognizable from the large source term values. In the nozzle region, no increased noise sources can be observed, suggesting that indirect noise is insignificant for the considered operating points. This observation is in line with high fidelity, compressible LES simulations [54]. In the CAA representation, smaller structures of the CFD field in the shear layer and the jet are removed by the spatial filter of width $\Delta\lambda$.

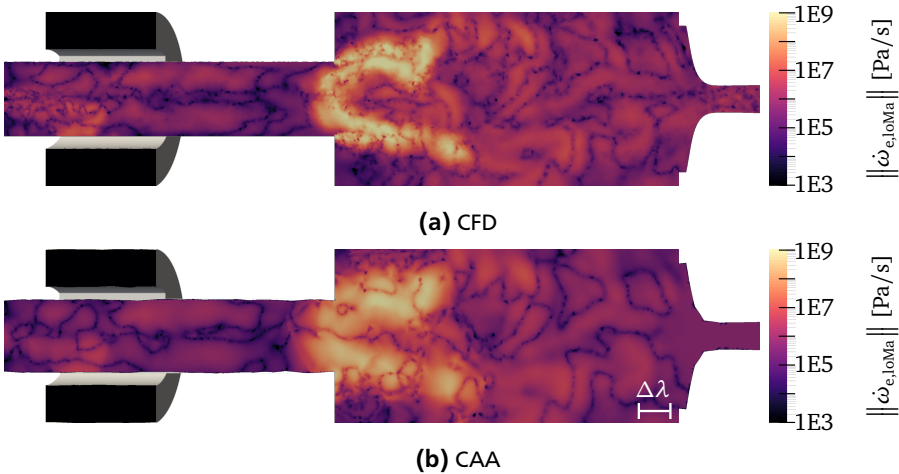


Figure 7.10: Instantaneous noise source field for OP-16-2 at $t_{\text{CFD}} = 0.045 \text{ s}$ (a) and $t_{\text{CAA}} = 0.045 \text{ s} + 2.5\text{E}-6 \text{ s}$ (b). Filter width $\Delta\lambda = 12 \text{ mm}$. Slice through the $x_3 = 0$ plane.

The spectra of the integral acoustic source term, given in Fig. 7.11, are computed from Eq. (6.4), analogously to the ones in chapter 6. Again, no significant peaks can be observed and the amplitudes decrease with the frequency until reaching a constant level between $f = 1 \text{ kHz}$ and 2 kHz . Qualitatively, both spectra are in good agreement with the original simulations. However, the source spectra for OP-13-5 exhibit increased amplitudes compared to the original LES. This deviation may be caused by large time scale effects subjected to statistical variations that cannot be sufficiently captured during the simulation time.

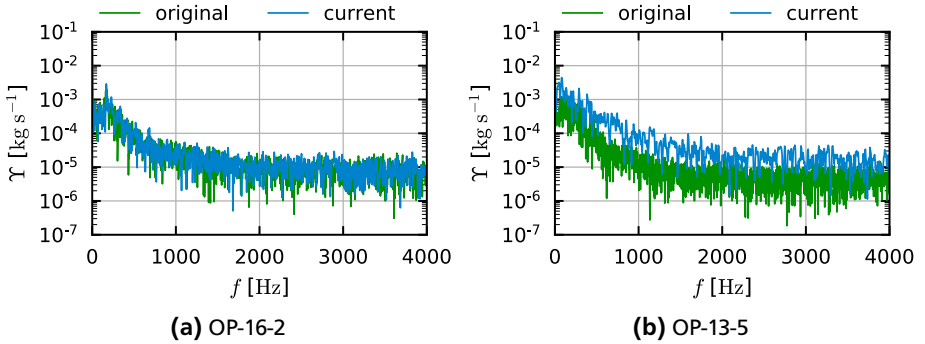


Figure 7.11: Noise sources spectra for OP-16-2 and OP-13-5. Original LES values from [136].

7.5 Acoustic Fields

In the following, the acoustic properties of the CESAM-HP test rig will be explored, by first providing an analysis of the relevant acoustic modes. Subsequently, the results are compared with experimental and frequency domain hybrid CAA results for both operating points. Consistent with [136, 135], all noise spectra are given in terms of the sound pressure level

$$L_p = 20 \log_{10} \left(\frac{|\mathcal{F}\{p^a\}|}{2E-5 \text{ Pa}} \right) \text{ dB} . \quad (7.2)$$

7.5.1 Acoustic Modes

For OP-16-2, the noise spectra obtained at different locations along the x_1 -axis as marked in Fig. 7.12 are depicted in Fig. 7.13. In the considered frequency range, the spectra at different radial locations show negligible variations and are therefore omitted. However, strong variations between the respective axial locations can be observed due to the complexity of the geometry. Seven major frequency peaks at $f \approx 170 \text{ Hz}$, 318 Hz , 540 Hz , 1500 Hz , 2000 Hz , 2900 Hz and 3500 Hz are identified. The two peaks at 318 Hz and 170 Hz are not caused by acoustic phenomena, but instead by the rotation of the vortex core and its precessing motion, respectively. The 1500 Hz peak is only visible in the premixing duct, the 2000 Hz peak is very weak in the combustion chamber and the peak at 3500 Hz is absent from the spectra at the third sampling location.

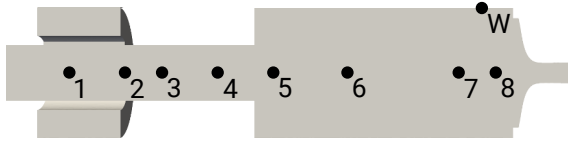


Figure 7.12: Sampling locations for the different spectra.

To identify the modes associated to these peaks, a point-wise Fourier transform with 1427 snapshots and a sampling rate of $f_s = 8$ kHz was performed. The resulting normalized acoustic pressure amplitudes are given for each peak frequency in Fig. 7.14 in terms of Eq. (6.6). The swirler and the corresponding ducts are omitted from the visualization, since they do not contribute to the relevant frequency range.

As evident from Fig. 7.14a, the 540 Hz peak is related to the axial $\lambda/2$ mode of the full geometry. It is consequently detected at every sample location in Fig. 7.13. The frequency domain simulations with the Helmholtz solver found a similar peak at 390 Hz, which was attributed to the same mode [135]. The 1500 Hz peak is associated to a spinning λ mode, as shown in Fig. 7.14b. Considering it is only detected upstream of the combustion chamber, the mode is likely located in the premixing duct. The peak at 2000 Hz is significantly more distinct in the upstream spectra, but absent at $x_1 = -0.07$ m and $x_1 = 0.01$ m, hinting at a $3/4 \lambda$ mode of the duct with pressure nodes at the respective axial positions. This assessment is corroborated by the acoustic pressure distribution in Fig. 7.14c and the f -domain Helmholtz solver simulations [135]. The frequency domain simulations [136] and the mode shape in Fig. 7.14d consistently associate the 2900 Hz peak with the $\lambda/2$ -mode of the combustion chamber. Moreover, the pressure amplitude distribution suggests the excitation of an additional λ mode in the duct with significantly larger amplitudes due to the higher impedance upstream of the flame. As indicated by the mode structure in Fig. 7.14e, the 3500 Hz peak is related to the $5/4 \lambda$ mode of the premixing duct. This observation is in line with the frequency domain simulations [136] and the individual spectra in Fig. 7.13. Therein, no 3500 Hz peak is detected at the corresponding pressure nodes at $x_1 = -0.10$ m and $x_1 = -0.05$ m.

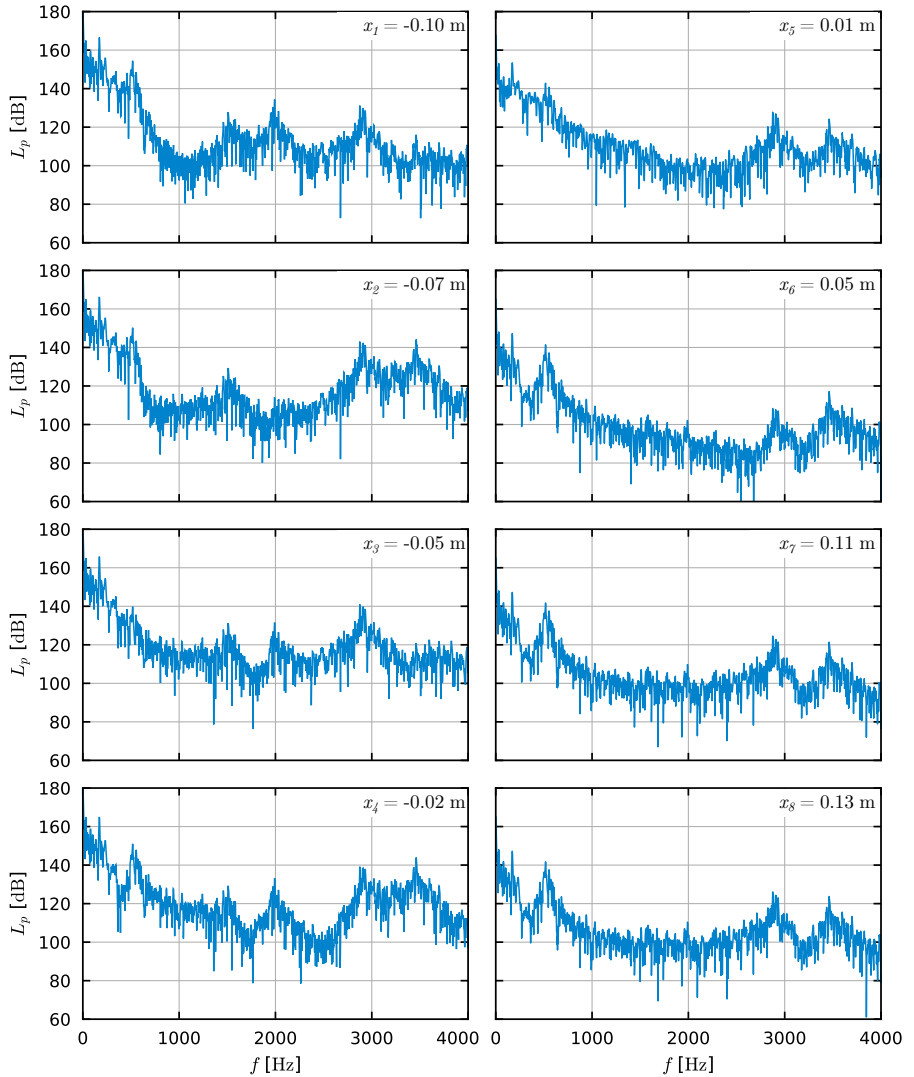


Figure 7.13: Noise spectra obtained from LES-CAA for OP-16-2 at different axial locations on the center line ($x_2 = x_3 = 0$) inside the premixing duct ($x_1 < 0$) and the combustion chamber ($0 < x_1$).

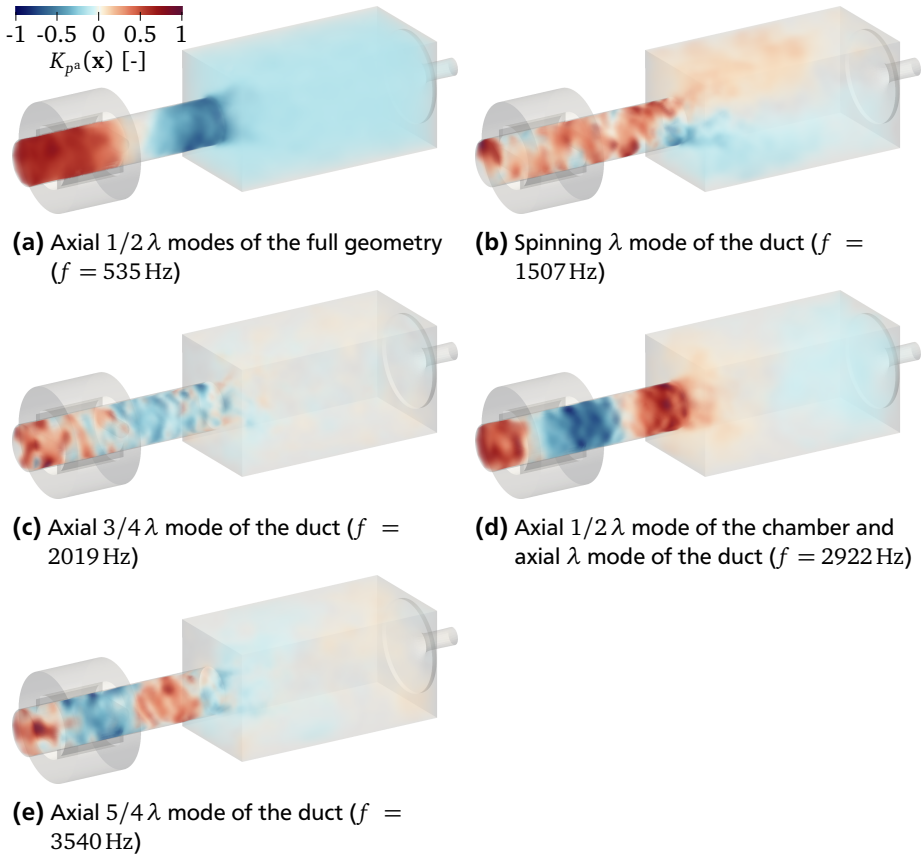


Figure 7.14: Normalized acoustic pressure amplitudes $K_{pa}(\mathbf{x})$ at the phase that corresponds to the largest amplitudes for a single frequency component. Swirler and swirler ducts omitted.

7.5.2 OP-16-2

Since no experimental data is available at the axial locations of Fig. 7.13, the experimental [89] and frequency-domain [136] spectra are compared at the top/bottom wall ($\mathbf{x} = [0.1225, 0.035, 0.0]^T \text{m}$). In Fig. 7.12, this location is indicated by a "W". The corresponding sound pressure levels for OP-16-2 are given in Fig. 7.15. For this operating point, no f -domain Helmholtz data is available. However, the corresponding spectrum in Fig 7.16 should be qualitatively similar for this operating point, since the Helmholtz equations do not take the base flow velocities into account.

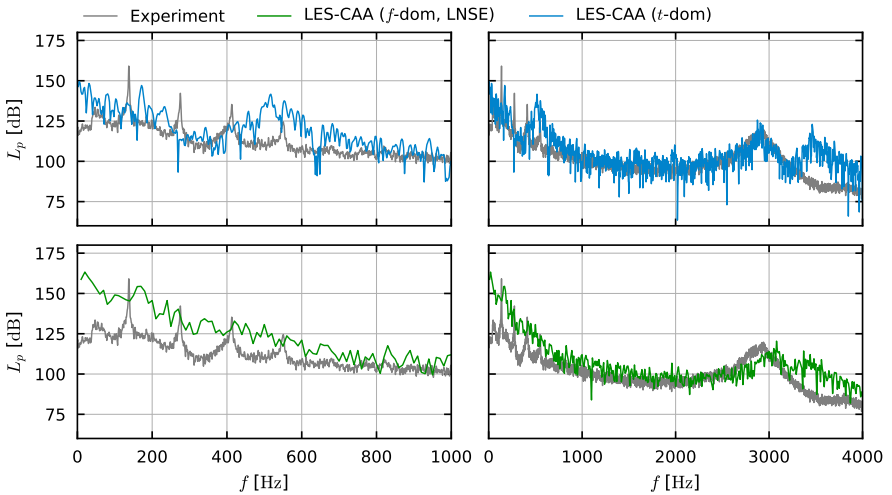


Figure 7.15: Noise spectra obtained from experimental pressure measurements [89] (Experiment), frequency domain LES-CAA with LNSE governing equations [136] (f -dom, LNSE), and the presented time domain LES-CAA (t -dom) for OP-16-2.

With regard to the overall amplitudes and the major peak frequency at 2900 Hz, very good agreement with the experimental and the LNSE f -domain simulations was achieved. In particular, the eigenfrequency peak at $f \approx 2900 \text{ Hz}$ of the $\lambda/2$ eigenmode of the combustion chamber is reproduced with minimal frequency shift and similar amplitudes. Compared to the experimental data, the LNSE f -domain simulation results exhibit a slight shift towards higher frequencies. This is not present in a different simulation based on a compressible RANS mean flow field

with lower temperature levels [136]. Four additional spectral peaks below 750 Hz were observed in the experiments, that are associated to thermoacoustic instabilities and hence cannot be reproduced with the uni-directional coupling.

Of the five dominant modes identified in the preceding subsection, only the $\lambda/2$ -mode at 2900 Hz is instigated in the experiment. In the LNSE-based f -domain spectra, the 3500 Hz peak can be observed in addition. Furthermore, the Helmholtz-based f -domain simulation (cf. Fig. 7.16) predicts maxima at $f \approx 390$ Hz and 2000 Hz, leaving the 1500 Hz-peak the only one which was predicted solely with the current method. In contrast to the LNSE, the employed APE and the Helmholtz equation both neglect damping through base flow gradients. This suggests that in the experiment and the LNSE solution, the growth of the $\lambda/2$ mode (540 Hz) that spans the flame, is limited by the corresponding steep density and base flow gradients. Similarly, the $3/4\lambda$ mode (2000 Hz) is not perceivable at the microphone or sampling locations, located inside the combustion chamber and hence behind the flame. The frequency peak at 1500 Hz was associated to the λ mode of the premixing duct and is thus absent from the experimental and LNSE spectra for the same reason. The mode was also not recovered by the Helmholtz based simulation, which indicates an excitation by transient effects. While the 3500 Hz peak is also present in both f -domain simulations and two compressible, high resolution LES simulations [54], it is not observed in the experimental spectra at the given location. A different microphone inside the swirler however, does show this peak [89], suggesting that it is present in the experiment as well, but damped in the chamber. Unlike the 540 Hz, 1500 Hz and 2000 Hz peaks, the 3500 Hz maximum is also recovered by the frequency domain solver, which suggest that in the experiment, the corresponding mode is attenuated due to a different mechanism.

7.5.3 OP-13-5

The noise spectra obtained for OP-13-5 were taken at the same location as for OP-16 and are given in Fig. 7.16. For this operating point no combustion instabilities were observed in the experiment. Again, the overall trend and the frequency of the 2900 Hz peak are in very good agreement with the reference solution and the measurements. However, the amplitudes tend to be overestimated in the higher frequency domain above 500 Hz. This is attributed to the increased source term levels of the CFD (cf. Fig. 7.11b), which for higher frequencies, exhibit larger amplitudes than in the original LES used for the f -domain simulations. Consequently, the resulting noise amplitudes must be elevated as well.

Again, additional peaks at $f \approx 540$ Hz, 1500 Hz, 2000 Hz and 3500 Hz are observed, which are associated to the same modes as in OP-16-2. Notable differences

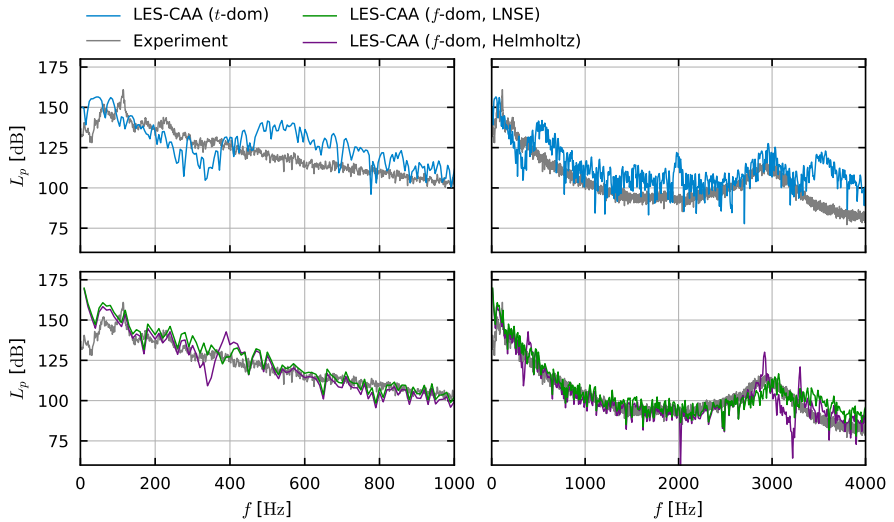


Figure 7.16: Noise spectra obtained from experimental pressure measurements [89] (Experiment), frequency domain LES-CAA with LNSE governing equations [136] (f -dom, LNSE), frequency domain LES-CAA with Helmholtz governing equations [135] (f -dom, Helmholtz), and the presented time domain LES-CAA (t -dom) for OP-13-5.

are an increased peak at $f \approx 2000$ Hz and lower amplitudes at $f \approx 1500$ Hz. Since for OP-13-5, no efficiency function limiter was used, the flame is able to propagate upstream of the chamber inlet. The noise sources are hence located closer to the $3/4 \lambda$ mode (2000 Hz), resulting in a stronger excitation. A similar behavior can be observed at 3500 Hz, where the peak is also much more distinct than in OP-16-2. The axial $\lambda/2$ mode, which was associated to the 540 Hz peak in OP-16-2, spans the entire domain, including the flame and the chamber inlet. Due to the stronger flame movement at OP-13-5, the distribution of the speed of sound within this mode is subject to much stronger fluctuations than in OP-16-2. Hence, the associated frequency fluctuates much stronger as well, leading to a widened frequency peak.

7.6 Sampling Resolution and Filter Width

With regard to the rather high spatial resolution of the CAA, the filter width and the order of the intermediate expansion were set to $\Delta\lambda = 12$ mm and $Q_{\text{int}} = 5$, respectively. Both values are near the lower stability limit of the coupling layer and minimize computational overhead (Q_{int}) and loss of information ($\Delta\lambda$). Their validity was consequently assessed by two additional simulations with a higher number of sampling points and a larger filter width. As evident from the corresponding sound pressure spectra in Fig. 7.17, neither modification has an impact on the result of the CAA. This suggests that also with $Q_{\text{int}} = 5$, the aliasing error related to the CFD field sampling is sufficiently low. Moreover, even with $\Delta\lambda = 24$ mm, the spectrum is not altered, indicating that the base flow gradients and the acoustic source term are still sufficiently resolved. At the same time, the CAA has shown to be stable with $\Delta\lambda = 12$ mm, which implies that with this smaller filter width, artifacts in the forward transform are already adequately avoided.

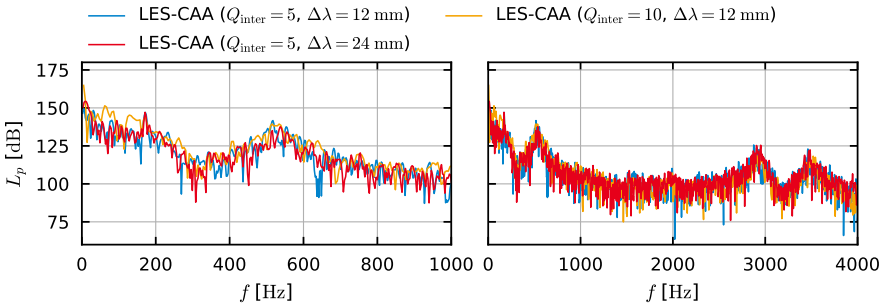


Figure 7.17: Noise spectra for OP-16-2, obtained with the presented hybrid CAA method using different filter widths and sampling resolutions.

7.7 Computational Efficiency

Compared to two standalone simulations, a coupled setup requires additional computational effort. Inevitable overhead is due to the pre- and post processing described in chapter 5 and waiting times related to the data transfers. This is due to fluctuating step times of both solvers, caused by writing to disk, differently conditioned matrices, available computing resources, etc. The overhead is minimized by the MPI-based implementation and a fully asynchronous communication strategy.

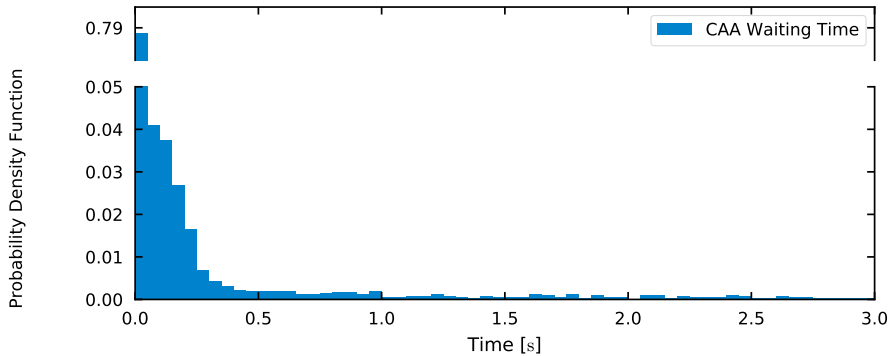


Figure 7.18: Normalized histogram of CAA waiting times for a single run.

For the CESAM-HP test rig, the simulations were run on 144 cores, 72 for the CAA and 72 for the CFD. With this setup, the CFD rarely has to wait for the CAA, yielding a total CFD waiting time below 1%. Since no other coupling related steps are performed by the CFD, this 1% also marks the total CFD overhead. The CAA spent up to 2% of the total computational time on post-processing (extrapolation, filtering, projection, interpolation) the received fields and between 1.5% and 4.5% on waiting for the CFD solver. While the post-processing time is almost constant over the time steps, the probability density function of the CAA waiting times in Fig. 7.18 shows that in over 78% of the exchanges, the CAA had to wait less than 0.05 s. This indicates that even though the CFD has slightly shorter step times, the load is almost perfectly balanced in this setup. Nevertheless, it should be noted that these numbers are highly specific to the considered problem, mesh sizes, cluster architecture, exchange frequency, etc. and can reveal completely different, less favorable statistics for other setups.

7.8 Summary

Two operating points, OP-16-2 with a weak and OP-13-5 with a strong jet, were investigated with the developed hybrid CAA method. At this, the flow field simulations showed a precessing vortex core for OP-16-2 and a stationary, asymmetrical vortex for OP-13-5. Due to the setup's inclination towards flashbacks, the flame location was limited for the more unstable operating point OP-16-2. By using

frequency spectra at different axial locations and a point-wise Fourier transform at the selected frequencies, the eigenmodes of the five obtained frequency peaks were identified. In general, good agreement with experimental and frequency domain data was found in terms of noise spectra for both operating points. Deviations were due to thermoacoustic instabilities of OP-16-2, and recovered frequency peaks that were attenuated in the experimental data. The modes that correspond to the additional peaks were found to be insufficiently attenuated, most likely due to simplifications inherent to the APE or the acoustic source term formulation. It was demonstrated in two additional simulations, that despite the audacious coupling parameters, numerical instabilities are sufficiently avoided, while preserving the relevant base flow gradients and acoustic source term. With the given distribution of computing resources, the presented approach required twice the computational effort of the low Mach number CFD itself, with minimal overhead due to the coupling layer. A direct noise simulation, that yields comparable results would entail smaller time steps and a finer spectral resolution in order to temporally and spatially resolve the acoustics². Even though the computational cost does not necessarily increase linearly with the number of unknowns, it is safe to assume a 10 to 20 times higher requirement in computational time. Consequently, the presented method is about 5 to 10 times more efficient than the direct noise simulation for the considered setup. Moreover, the CAA results indicate that the current method's efficiency could be further improved by using a coarser CAA mesh and a larger time step size.

² For the CESAM-HP test rig, a DNC simulation was conducted by ONERA [54] using the CEDRE solver with an implicit time stepping scheme, second order spatial discretization and an artificial quenching inside the premixing duct, similar to the current CFD. The mesh consisted of 11.1 Million cells, which, at the time step size of $\Delta t = 1\text{E}-6\text{s}$, resulted in the 19.8-fold degrees of freedom of the current low Mach number LES.

8 Conclusions

In this work, a hybrid CAA method was developed, that allows for the robust and efficient simulation of aeroacoustic problems in complex, enclosed domains. It comprises a low Mach number flow solver, an acoustics solver and a coupling layer, which bridges the different numerical schemes and physical scales in order to optimize the numerical efficiency of each solver. At this, the key components are the novel CAA solver and the coupling layer, which hence constitute the focus of this work. For the description of the reacting flow field, an established, FVM based CFD solver was equipped with the coupling interface.

By employing the high order spectral/hp element method in a discontinuous Galerkin formulation, the newly developed CAA solver efficiently accounts for acoustic wave propagation in complex, three-dimensional geometries. Its implementation is focused on stability and flexibility to allow for an easy adaption to industrial applications, such as combustion noise. This is achieved by solving the unconditionally stable Acoustic Perturbation Equations and a using set of Riemann solvers that can operate on variable density base flows. In order to enable bi-directional communication between both solvers, a coupling layer was developed, that allows for continuous data exchange at run time, by passing all data over MPI in a distributed manner. During the CFD-CAA coupling, three major error sources were identified, that arise from the different length scales and discretization methods of the two solvers. Based on this assessment, a three stage coupling scheme was devised, which involves a linear interpolation in time and a spatial, implicit low pass filter, that operates on an intermediate representation of the CFD fields. It is due to this coupling layer, that both solvers can operate at their optimal spatial and temporal resolutions, even when applied to coinciding domains.

The applicability of the hybrid CAA method was investigated by means of two laboratory scale combustors of increasing complexity. The first setup featured a half-dump combustor, that facilitated a basic validation of the CAA solver and the coupling, as well as the exploration of different coupling parameters. The latter showed that, despite the coarse spatial CAA resolution, the short length scale base flow fields were sufficiently represented in terms of the CAA expansion by the devised coupling layer. In the obtained acoustic fields, the behavior of the system's first eigenmode was well reproduced. The instigation of a second eigenmode, that was not observed in the experimental noise spectrum, was in agreement with a

similar hybrid CAA simulation. Finally, the bi-directional coupling was demonstrated by transferring the acoustic pressure fluctuations to the CFD, where they were successfully recovered from the flow fields. Although not an aim of this work, an example feedback mechanism was tested, which had negligible impact on the combustion.

The second configuration was a pressurized burner, operated by a swirl stabilized, premixed flame that is prone to flashbacks. It therefore features most phenomena present in industry scale combustion systems and consequently marks an intermediate step towards such applications. Due to its complex geometry, the combustor is already beyond the capabilities of most available CAA tools. The thermoacoustic properties of two operating points were studied, that are characterized by a precessing and a stable, asymmetrical vortex core, respectively. In the considered frequency range, the prevalent eigenmode observed in the experiments was very well predicted. However, comparison with reference data from an LNSE based hybrid CAA revealed an insufficient damping in the vortex or the flame front for three further modes. This is most likely due to simplifying modeling assumptions inherent to the APE and the chosen source term formulation, which might be too restrictive under certain conditions. Based on the total numbers of degrees of freedom, the developed method was estimated to require less than a fifth of the computational effort of a direct noise simulation for the considered configuration.

With the current implementation of the CAA solver and the coupling layer, a tool for future research in time-domain, hybrid CAA methods is available. In order to ensure the method's applicability to larger, more complex configurations, the coupling layer may require further optimization. For combustion noise simulation, two major issues that should be addressed in the future became apparent. The insufficient attenuation of acoustic modes spanning a swirling flame suggest a further investigation of the APE and the chosen source term formulation. At this, an exploration of alternative acoustic governing equations may be worthwhile as well. For the correct simulation of thermoacoustic instabilities, novel acoustic feedback modeling approaches are required. The current CAA method is designed to aid this development and facilitate the corresponding research. Although it was featured in this work, the developed method is not limited to enclosed or combustion noise related configurations. This was recently demonstrated by another research group, who is already using the current CAA method for jet noise simulations. By providing the implementations of the CAA solver and the coupling layer to the scientific community as an open source code, the author hopes to spark further adaption and novel applications of hybrid CAA methods.

Bibliography

- [1] ACARE. *Strategic Research & Innovation Agenda*. Report. Advisory Council for Aviation Research and Innovation in Europe, 2017.
- [2] M. Ainsworth. “Dispersive and dissipative behaviour of high order discontinuous Galerkin finite element methods”. In: *Journal of Computational Physics* 198.1 (2004), pp. 106–130.
- [3] P. R. Amestoy, I. S. Duff, J.-Y. EExcellent, and J. Koster. “A Fully Asynchronous Multifrontal Solver Using Distributed Dynamic Scheduling”. In: *SIAM Journal on Matrix Analysis and Applications* 23.1 (2001), pp. 15–41.
- [4] M. S. Anand, R. Eggels, M. Staufer, M. Zedda, and J. Zhu. “An advanced unstructured-grid finite-volume design system for gas turbine combustion analysis”. In: *ASME 2013 Gas Turbine India Conference*. GTINDIA2013-3537. ASME, 2013.
- [5] R. Arina, R. Della Ratta Rinaldi, and A. Iob. “A Discontinuous Galerkin Method for Long-Time Simulations in Aeroacoustics”. In: *16th AIAA/CEAS Aeroacoustics Conference*. American Institute of Aeronautics and Astronautics, 2010.
- [6] K. Aschmoneit. “Numerische Beschreibung Technischer Verbrennungssysteme”. Doctoral Thesis. Technische Universität Darmstadt, 2013.
- [7] M. Bauer, J. Dierke, and R. Ewert. “Application of a Discontinuous Galerkin Method to Discretize Acoustic Perturbation Equations”. In: *AIAA Journal* 49.5 (2011), pp. 898–908.
- [8] C. P. A. Blom. “Discontinuous Galerkin Method on Tetrahedral Elements for Aeroacoustics”. Doctoral Thesis. University of Twente, 2003.
- [9] C. Bogey, C. Bailly, and D. Juve. “Computation of flow noise using source terms in linearized Euler’s equations”. In: *AIAA Journal* 40.2 (2002), pp. 235–243.
- [10] A. Bolis, C. D. Cantwell, R. M. Kirby, and S. J. Sherwin. “From h to p efficiently: Optimal implementation strategies for explicit time-dependent problems using the spectral/hp element method”. In: *International Journal for Numerical Methods in Fluids* 75.8 (2014), pp. 591–607.

-
- [11] T. P. Bui. “Theoretical and Numerical Analysis of Broadband Combustion Noise”. Doctoral Thesis. RWTH Aachen, 2008.
- [12] T. P. Bui, M. Meinke, W. Schröder, F. Flemming, A. Sadiki, and J. Janicka. “A Hybrid Method for Combustion Noise Based on LES and APE”. In: *11th AIAA/CEAS Aeroacoustics Conference*. American Institute of Aeronautics and Astronautics, 2005.
- [13] T. P. Bui, W. Schröder, and M. Meinke. “Numerical analysis of the acoustic field of reacting flows via acoustic perturbation equations”. In: *Computers & Fluids* 37.9 (2008), pp. 1157–1169.
- [14] S. Buis, A. Piacentini, and D. Déclat. “PALM: A computational framework for assembling high-performance computing applications”. In: *Concurrency Computation Practice and Experience* 18.2 (2006), pp. 231–245.
- [15] G. Bulat, E. Fedina, C. Fureby, W. Meier, and U. Stopper. “Reacting flow in an industrial gas turbine combustor: LES and experimental analysis”. In: *Proceedings of the Combustion Institute* 35.3 (2015), pp. 3175–3183.
- [16] T. D. Butler and P. J. O’Rourke. “A numerical method for two dimensional unsteady reacting flows”. In: *Symposium (International) on Combustion* 16.1 (1977), pp. 1503–1515.
- [17] S. Candel. “Combustion dynamics and control: Progress and challenges”. In: *Proceedings of the Combustion Institute* 29.1 (2002), pp. 1–28.
- [18] S. Candel, D. Durox, T. Schuller, J.-F. Bourgouin, and J. P. Moeck. “Dynamics of Swirling Flames”. In: *Annual Review of Fluid Mechanics* 46.1 (2014), pp. 147–173.
- [19] C. Cantwell et al. “Nektar++: An open-source spectral/hp element framework”. In: *Computer Physics Communications* 192 (2015), pp. 205–219.
- [20] CERFACS. *OpenPALM Website*. URL: http://www.cerfacs.fr/globc/PALM_WEB/index.html (visited on 2018-03-03).
- [21] S. R. Chakravarthy, O. J. Shreenivasan, B. Boehm, A. Dreizler, and J. Janicka. “Experimental characterization of onset of acoustic instability in a nonpremixed half-dump combustor”. In: *The Journal of the Acoustical Society of America* 122.1 (2007), pp. 120–127.
- [22] F. Charlette, C. Meneveau, and D. Veynante. “A power-law flame wrinkling model for LES of premixed turbulent combustion Part II: Dynamic formulation”. In: *Combustion and Flame* 131.1-2 (2002), pp. 181–197.

-
- [23] N. Chevaugéon, J.-F. Remacle, X. Gallez, P. Ploumans, and S. Caro. “Efficient Discontinuous Galerkin Methods for solving acoustic problems”. In: *11th AIAA/CEAS Aeroacoustics Conference*. American Institute of Aeronautics and Astronautics, 2005.
- [24] B. Cockburn, G. E. Karniadakis, and C.-W. Shu, eds. *Discontinuous Galerkin Methods*. Lecture Notes in Computational Science and Engineering. Springer, 2000.
- [25] T. Colonius and S. K. Lele. “Computational aeroacoustics: Progress on non-linear problems of sound generation”. In: *Progress in Aerospace Sciences* 40.6 (2004), pp. 345–416.
- [26] G. Cunha and S. Redonnet. “Development of optimized interpolation schemes with spurious modes minimization”. In: *International Journal for Numerical Methods in Fluids* 80.2 (2016), pp. 140–158.
- [27] G. Cunha and S. Redonnet. “On the signal degradation induced by the interpolation and the sampling rate reduction in aeroacoustics hybrid methods”. In: *International Journal for Numerical Methods in Fluids* 71.7 (2013), pp. 910–929.
- [28] A. P. Dowling and Y. Mahmoudi. “Combustion noise”. In: *Proceedings of the Combustion Institute* 35.1 (2015), pp. 65–100.
- [29] F. Duchaine, S. Jauré, D. Poitou, E. Quémerais, G. Staffelbach, T. Morel, and L. Gicquel. “Analysis of high performance conjugate heat transfer with the OpenPALM coupler”. In: *Computational Science & Discovery* 8.1 (2015).
- [30] L. Durand and W. Polifke. “Implementation of the Thickened Flame Model for Large Eddy Simulation of Turbulent Premixed Combustion in a Commercial Solver”. In: *ASME Turbo Expo 2007*. GT2007-28188. ASME, 2007.
- [31] C. Duwig, B. Gherman, M. Mihaescu, M. Salewski, and L. Fuchs. “Numerical Study of Thermo-Acoustic Waves Generation by a Swirling Flame Using a New Approach Based on Large Eddy Simulation”. In: *ASME Turbo Expo 2005*. GT2005-68136. ASME, 2005.
- [32] Eindhoven University of Technology. *CHEM1D*. URL: <https://www.tue.nl/en/university/departments/mechanical-engineering/research/research-groups/multiphase-and-reactive-flows/our-expertise/research-topics/chem1d/> (visited on 2018-03-08).
- [33] R. Ewert, W. Schröder, M. Meinke, and W. El-Askary. “LES as a basis to determine sound emission”. In: *40th AIAA Aerospace Sciences Meeting & Exhibit*. American Institute of Aeronautics and Astronautics, 2002.

-
- [34] R. Ewert and W. Schröder. “Acoustic perturbation equations based on flow decomposition via source filtering”. In: *Journal of Computational Physics* 188.2 (2003), pp. 365–398.
- [35] J. H. Ferziger and M. Peric. *Numerische Strömungsmechanik*. Springer, 2008.
- [36] F. Flemming, A. Sadiki, and J. Janicka. “Investigation of combustion noise using a LES/CAA hybrid approach”. In: *Proceedings of the Combustion Institute* 31.2 (2007), pp. 3189–3196.
- [37] A. P. Fosso, H. Deniau, N. Lamarque, and T. Poinso. “Comparison of outflow boundary conditions for subsonic aeroacoustic simulations”. In: *International Journal for Numerical Methods in Fluids* 68.10 (2011), pp. 1207–1233.
- [38] C. Fureby. “LES of a multi-burner annular gas turbine combustor”. In: *Flow, Turbulence and Combustion* 84.3 (2010), pp. 543–564.
- [39] G. Geiser, S. Schlimpert, and W. Schröder. “Thermoacoustical noise induced by laminar flame annihilation at varying flame thicknesses”. In: *18th AIAA/CEAS Aeroacoustics Conference*. American Institute of Aeronautics and Astronautics, 2012.
- [40] G. Geiser. “Thermoacoustic Noise Sources in Premixed Combustion”. Doctoral Thesis. RWTH Aachen, 2014.
- [41] G. Geiser, H. Nawroth, A. Hosseinzadeh, F. Zhang, H. Bockhorn, P. Habisreuther, J. Janicka, C. O. Paschereit, and W. Schröder. “Thermoacoustics of a turbulent premixed flame”. In: *20th AIAA/CEAS Aeroacoustics Conference*. American Institute of Aeronautics and Astronautics, 2014.
- [42] M. Germano. “Differential filters for the large eddy numerical simulation of turbulent flows”. In: *Physics of Fluids* 29.6 (1986), p. 1755.
- [43] L. Y. M. Gicquel, G. Staffelbach, and T. Poinso. “Large Eddy Simulations of gaseous flames in gas turbine combustion chambers”. In: *Progress in Energy and Combustion Science* 38.6 (2012), pp. 782–817.
- [44] O. Gicquel, N. Darabiha, and D. Thévenin. “Laminar premixed hydrogen/air counterflow flame simulations using flame prolongation of ILDM with differential diffusion”. In: *Proceedings of the Combustion Institute* 28.2 (2000), pp. 1901–1908.
- [45] J. Gikadi, T. Sattelmayer, and A. Peschiulli. “Effects of the mean flow field on the thermo-acoustic stability of aero-engine combustion chambers”. In: *ASME Turbo Expo 2012*. GT2012-69612. ASME, 2012.

-
- [46] M. M. Gracia, B. Vaneldereren, W. De Roeck, and W. Desmet. “Accurate interfacing schemes for the coupling of CFD data with high order DG methods for aeroacoustic propagation”. In: *Proceedings of the 26th Conference on Noise and Vibration Engineering (ISMA2014)*. Vol. 26. 2014, pp. 1333–1346.
- [47] X. Han, J. Li, and A. S. Morgans. “Prediction of combustion instability limit cycle oscillations by combining flame describing function simulations with a thermoacoustic network model”. In: *Combustion and Flame* 162.10 (2015), pp. 3632–3647.
- [48] J. C. Hardin and D. S. Pope. “An Acoustic / Viscous Splitting Technique for Computational Aeroacoustics”. In: *Theoretical and Computational Fluid Dynamics* 6.5-6 (1994), pp. 323–340.
- [49] C. Hirsch, J. Wäsle, A. Winkler, and T. Sattelmayer. “A spectral model for the sound pressure from turbulent premixed combustion”. In: *Proceedings of the Combustion Institute* 31.1 (2007), pp. 1435–1441.
- [50] C. Hirsch. *Numerical Computation of Internal and External Flows: The Fundamentals of Computational Fluid Dynamics, Second Edition*. Butterworth-Heinemann, 2007.
- [51] F. Q. Hu, M. Hussaini, and P. Rasetarinera. “An Analysis of the Discontinuous Galerkin Method for Wave Propagation Problems”. In: *Journal of Computational Physics* 151.2 (1999), pp. 921–946.
- [52] F. Hu and H. Atkins. “Two-dimensional Wave Analysis of the Discontinuous Galerkin Method with Non-Uniform Grids and Boundary Conditions”. In: *8th AIAA/CEAS Aeroacoustics Conference & Exhibit*. American Institute of Aeronautics and Astronautics, 2002.
- [53] Y. Huang, H.-G. Sung, S.-Y. Hsieh, and V. Yang. “Large-Eddy Simulation of Combustion Dynamics of Lean-Premixed Swirl-Stabilized Combustor”. In: *Journal of Propulsion and Power* 19.5 (2003), pp. 782–794.
- [54] M. Huet et al. “Recent Improvements in Combustion Noise Investigation: from the Combustion Chamber to Nozzle Flow”. In: *AerospaceLab* (2016).
- [55] IATA. *20 Year Passenger Forecast*. 2017. URL: <http://www.iata.org/pressroom/pr/Pages/2017-10-24-01.aspx> (visited on 2018-02-17).
- [56] IATA. *Economic performance of the airline industry*. Report. IATA, 2017.

-
- [57] M. Ihme, D. Bodony, and H. Pitsch. “Prediction of Combustion-Generated Noise in Non-Premixed Turbulent Jet Flames Using LES”. In: *12th AIAA/CEAS Aeroacoustics Conference*. American Institute of Aeronautics and Astronautics, 2006.
- [58] J. Janicka and A. Sadiki. “Large eddy simulation of turbulent combustion systems”. In: *Proceedings of the Combustion Institute* 30.1 (2005), pp. 537–547.
- [59] C. Jiménez, F. Ducros, B. Cuenot, and B. Bédard. “Subgrid scale variance and dissipation of a scalar field in large eddy simulations”. In: *Physics of Fluids* 13.6 (2001), pp. 1748–1754.
- [60] A. Kannan and S. R. Chakravarthy. “A Framework to Predict Combustion Noise and Instability: Case Study of a Partially Premixed Flame in a Backward-Facing Step Combustor”. In: *ASME Turbo Expo 2017*. GT2017-65211. ASME, 2017.
- [61] A. Kannan, B. Chellappan, and S. R. Chakravarthy. “Flame-acoustic coupling of combustion instability in a non-premixed backward-facing step combustor: the role of acoustic-Reynolds stress”. In: *Combustion Theory and Modelling* 20.4 (2016), pp. 658–682.
- [62] G. E. Karniadakis and S. J. Sherwin. *Spectral/hp Element Methods for Computational Fluid Dynamics*. 2nd ed. Oxford University Press, 2005.
- [63] M. Käser and M. Dumbser. “An arbitrary high-order discontinuous Galerkin method for elastic waves on unstructured meshes - I. The two-dimensional isotropic case with external source terms”. In: *Geophysical Journal International* 166.2 (2006), pp. 855–877.
- [64] K. A. Kemenov, H. Wang, and S. B. Pope. “Modelling effects of subgrid-scale mixture fraction variance in LES of a piloted diffusion flame”. In: *Combustion Theory and Modelling* 16.4 (2012), pp. 611–638.
- [65] A. Kempf, M. Klein, and J. Janicka. “Efficient Generation of Initial- and Inflow-Conditions for Transient Turbulent Flows in Arbitrary Geometries”. In: *Flow, Turbulence and Combustion* 74.1 (2005), pp. 67–84.
- [66] T. Klenke. “Hybride numerische Simulation von Verbrennungslärm und thermoakustischen Instabilitäten in technischen Verbrennungssystemen”. Doctoral Thesis. Technische Universität Darmstadt, 2017.
- [67] T. Klenke, F. Lo Presti, K. Lackhove, F. di Mare, A. Sadiki, and J. Janicka. “Two-Way Hybrid LES/CAA Approach Including Acoustic Feedback Loop for the Prediction of Thermoacoustic Instabilities in Technical Combustors”. In: *ASME Turbo Expo 2017*. GT2017-63271. ASME, 2017.

-
- [68] C. Klewer, A. Ketelheun, and J. Janicka. “Numerical Analysis of Thermoacoustic Instabilities Using LES and Computational Aeroacoustics”. In: *Zeitschrift für Physikalische Chemie* 225 (2011), pp. 1393–1403.
- [69] C. Koren, R. Vicquelin, and O. Gicquel. “An Acceleration Method for Numerical Studies of Conjugate Heat Transfer With a Self-Adaptive Coupling Time Step Method: Application to a Wall-Impinging Flame”. In: *ASME Turbo Expo 2017*. GT2017-64224. ASME, 2017.
- [70] C. Koren, R. Vicquelin, and O. Gicquel. “High-Fidelity Multiphysics Simulation of a Confined Premixed Swirling Flame Combining Large-Eddy Simulation, Wall Heat Conduction and Radiative Energy Transfer”. In: *ASME Turbo Expo 2017*. GT2017-64844. ASME, 2017.
- [71] G. Kuenne, A. Ketelheun, and J. Janicka. “LES modeling of premixed combustion using a thickened flame approach coupled with FGM tabulated chemistry”. In: *Combustion and Flame* 158.9 (2011), pp. 1750–1767.
- [72] K. A. Kurbatskii and R. R. Mankbadi. “Review of Computational Aeroacoustics Algorithms”. In: *International Journal of Computational Fluid Dynamics* 18.6 (2004), pp. 533–546.
- [73] O. Labbé, C. Peyret, G. Rahier, and M. Huet. “A CFD/CAA coupling method applied to jet noise prediction”. In: *Computers & Fluids* 86 (2013), pp. 1–13.
- [74] K. Lackhove, A. Sadiki, and J. Janicka. “Efficient Three Dimensional Time-Domain Combustion Noise Simulation of a Premixed Flame Using Acoustic Perturbation Equations and Incompressible LES”. In: *ASME Turbo Expo 2017*. GT2017-63050. ASME, 2017.
- [75] C. J. Lapeyre, M. Mazur, P. Scoufflaire, F. Richecoeur, S. Ducruix, and T. Poinot. “Acoustically Induced Flashback in a Staged Swirl-Stabilized Combustor”. In: *Flow, Turbulence and Combustion* 98.1 (2016), pp. 265–282.
- [76] A. Lario, R. Arina, and A. Iob. “A Discontinuous Galerkin Method for the Solution of the Linearized Navier-Stokes Equations”. In: *19th AIAA/CEAS Aeroacoustics Conference*. American Institute of Aeronautics and Astronautics, 2013.
- [77] R. Léger, C. Peyret, and S. Piperno. “Coupled Discontinuous Galerkin/Finite Difference Solver on Hybrid Meshes for Computational Aeroacoustics”. In: *AIAA Journal* 50.2 (2012), pp. 338–349.
- [78] S. K. Lele. “Compact finite difference schemes with spectral-like resolution”. In: *Journal of Computational Physics* 103.1 (1992), pp. 16–42.

-
- [79] S. K. Lele and J. W. Nichols. “A second golden age of aeroacoustics?” In: *Philosophical Transactions of the Royal Society A: Mathematical, Physical and Engineering Sciences* 372 (2014).
- [80] R. J. LeVeque. *Finite-Volume Methods for Hyperbolic Problems*. Cambridge University Press, 2004, p. 578.
- [81] T. Lieuwen. “Modeling Premixed Combustion-Acoustic Wave Interactions: A Review”. In: *Journal of Propulsion and Power* 19.5 (2003), pp. 765–781.
- [82] T. Lieuwen, H. Torres, C. Johnson, and B. T. Zinn. “A Mechanism of Combustion Instability in Lean Premixed Gas Turbine Combustors”. In: *Journal of Engineering for Gas Turbines and Power* 123.1 (2001), p. 182.
- [83] M. J. Lighthill. “On Sound Generated Aerodynamically. I. General Theory”. In: *Proceedings of the Royal Society A: Mathematical, Physical and Engineering Sciences* 211.1107 (1952), pp. 564–587.
- [84] M. J. Lighthill. “On Sound Generated Aerodynamically. II. Turbulence as a Source of Sound”. In: *Proceedings of the Royal Society A: Mathematical, Physical and Engineering Sciences* 222.1148 (1954), pp. 1–32.
- [85] D. K. Lilly. “A proposed modification of the Germano subgrid-scale closure method”. In: *Physics of Fluids A: Fluid Dynamics* 4.3 (1992), pp. 633–635.
- [86] Y. Liu, A. P. Dowling, N. Swaminathan, R. Morvant, M. A. Macquisten, and L. F. Caracciolo. “Prediction of Combustion Noise for an Aeroengine Combustor”. In: *Journal of Propulsion and Power* 30.1 (2014), pp. 114–122.
- [87] T. Livebardon, S. Moreau, T. Poinsot, and E. Bouty. “Numerical investigation of combustion noise generation in a full annular combustion chamber”. In: *21st AIAA/CEAS Aeroacoustics Conference*. American Institute of Aeronautics and Astronautics, 2015.
- [88] F. di Mare, R. Knappstein, and M. Baumann. “Application of LES-quality criteria to internal combustion engine flows”. In: *Computers & Fluids* 89 (2014), pp. 200–213.
- [89] M. Mazur, W. Tao, P. Scoufflaire, F. Richecoeur, and S. Ducruix. “Experimental and Analytical Study of the Acoustic Properties of a Gas Turbine Model Combustor With a Choked Nozzle”. In: *ASME Turbo Expo 2015*. GT2015-43013. ASME, 2015.
- [90] G. Mengaldo, R. Moura, B. Giralda, J. Peiró, and S. Sherwin. “Spatial eigen-solution analysis of discontinuous Galerkin schemes with practical insights for under-resolved computations and implicit LES”. In: *Computers & Fluids* (2017).

-
- [91] G. Mengaldo, D. D. Grazia, F. Witherden, A. Farrington, P. Vincent, S. Sherwin, and J. Peiro. “A Guide to the Implementation of Boundary Conditions in Compact High-Order Methods for Compressible Aerodynamics”. In: *7th AIAA Theoretical Fluid Mechanics Conference*. American Institute of Aeronautics and Astronautics, 2014.
- [92] S. Menon, C. Stone, V. Sankaran, and B. Sekar. “Large-eddy simulations of combustion in gas turbine combustors”. In: *38th Aerospace Sciences Meeting and Exhibit*. American Institute of Aeronautics and Astronautics, 2000.
- [93] Message Passing Interface Forum. *MPI: A message-passing interface standard*. Standard. Message Passing Interface Forum, 2012.
- [94] M. Moratilla-Vega, H. Xia, and G. J. Page. “A coupled LES-APE approach for jet noise prediction”. In: *46th International Congress and Exposition on Noise Control Engineering (InterNoise 2017)*. Hong Kong, 2017.
- [95] R. C. Moura, S. J. Sherwin, and J. Peiró. “Linear dispersion-diffusion analysis and its application to under-resolved turbulence simulations using discontinuous Galerkin spectral/hp methods”. In: *Journal of Computational Physics* 298 (2015), pp. 695–710.
- [96] D. Moxey, C. Cantwell, R. Kirby, and S. Sherwin. “Optimising the performance of the spectral/hp element method with collective linear algebra operations”. In: *Computer Methods in Applied Mechanics and Engineering* 310 (2016), pp. 628–645.
- [97] E.-A. Müller and F. Obermeier. “The spinning vortices as a source of sound”. In: *AGARD CP-22*. 1967, pp. 21–22.
- [98] C.-D. Munz, M. Dumbser, and S. Roller. “Linearized acoustic perturbation equations for low Mach number flow with variable density and temperature”. In: *Journal of Computational Physics* 224.1 (2007), pp. 352–364.
- [99] D. Nance and L. Sankar. “Low dispersion finite volume schemes in the resolution of vortex shedding noise”. In: *36th AIAA Aerospace Sciences Meeting and Exhibit*. American Institute of Aeronautics and Astronautics, 1998.
- [100] F. Nicoud. “Conservative high-order finite-difference schemes for low-Mach number flows”. In: *Journal of Computational Physics* 158.1 (2000), pp. 71–97.
- [101] Y. Notay. *AGMG software and documentation*. URL: <http://homepages.ulb.ac.be/~ynotay/AGMG> (visited on 2017-12-14).

-
- [102] P. J. O'Rourke and F. V. Bracco. "Two scaling transformations for the numerical computation of multidimensional unsteady laminar flames". In: *Journal of Computational Physics* 33.2 (1979), pp. 185–203.
- [103] J. van Oijen, A. Donini, R. Bastiaans, J. ten Thijsse Boonkcamp, and L. de Goey. "State-of-the-art in premixed combustion modeling using flamelet generated manifolds". In: *Progress in Energy and Combustion Science* 57 (2016), pp. 30–74.
- [104] J. A. van Oijen. "Flamelet-Generated Manifolds: Development and Application to Premixed Laminar Flames". Doctoral Thesis. Eindhoven University of Technology, 2002.
- [105] J. A. van Oijen and L. de Goey. "Modelling of Premixed Laminar Flames using Flamelet-Generated Manifolds". In: *Combustion Science and Technology* 161.1 (2000), pp. 113–137.
- [106] J. A. van Oijen, F. Lammers, and L. de Goey. "Modeling of complex premixed burner systems by using flamelet-generated manifolds". In: *Combustion and Flame* 127.3 (2001), pp. 2124–2134.
- [107] A. T. Patera. "A spectral element method for fluid dynamics: Laminar flow in a channel expansion". In: *Journal of Computational Physics* 54.3 (1984), pp. 468–488.
- [108] T. J. Poinso and S. K. Lele. "Boundary conditions for direct numerical simulations of compressible viscous flows". In: *Journal of Computational Physics* 101.5 (1992), pp. 104–129.
- [109] T. Poinso and D. Veynante. *Theoretical and Numerical Combustion*. 3rd ed. 2012.
- [110] S. B. Pope. *Turbulent Flows*. Cambridge University Press, 2000.
- [111] C. Prax, F. Golanski, and L. Nadal. "Control of the vorticity mode in the linearized Euler equations for hybrid aeroacoustic prediction". In: *Journal of Computational Physics* 227.12 (2008), pp. 6044–6057.
- [112] A. Refloch, B. Courbet, A. Murrone, C. Laurent, J. Troyes, G. Chaineray, J. B. Dargaud, and F. Vuillot. "CEDRE Software". In: *AerospaceLab* (2011).
- [113] Y. Reymen, W. De Roeck, G. Rubio, M. Baelmans, and W. Desmet. "A 3D discontinuous galerkin method for aeroacoustic propagation". In: *12th International Congress on Sound and Vibration 2005, ICSV 2005*. Vol. 1. February 2016. 2005, pp. 761–770.

-
- [114] S. Roux, G. Lartigue, T. Poinso, U. Meier, and C. Bérat. “Studies of mean and unsteady flow in a swirled combustor using experiments, acoustic analysis, and large eddy simulations”. In: *Combustion and Flame* 141.1-2 (2005), pp. 40–54.
- [115] K. Salari and P. Knupp. *Code Verification by the Method of Manufactured Solutions*. Tech. rep. Albuquerque, NM, and Livermore, CA: Sandia National Laboratories, 2000.
- [116] M. Schäfer. *Computational Engineering - Introduction to Numerical Methods*. 1st ed. Springer, 2006.
- [117] M. Schlottke-Lakemper, M. Meinke, and W. Schröder. “A Hybrid Discontinuous Galerkin-Finite Volume Method for Computational Aeroacoustics”. In: *Notes on Numerical Fluid Mechanics and Multidisciplinary Design*. Springer International Publishing, 2016, pp. 743–753.
- [118] M. Schlottke-Lakemper, H. Yu, S. Berger, M. Meinke, and W. Schröder. “A fully coupled hybrid computational aeroacoustics method on hierarchical Cartesian meshes”. In: *Computers & Fluids* 144 (2017), pp. 137–153.
- [119] J.-H. Seo and Y. J. Moon. “Perturbed Compressible Equations for Aeroacoustic Noise Prediction at Low Mach Numbers”. In: *AIAA Journal* 43.8 (2005), pp. 1716–1724.
- [120] W. Shen and J. Sørensen. “Aeroacoustic Modelling of Low-Speed Flows”. In: *Theoretical and Computational Fluid Dynamics* 13.4 (1999), pp. 271–289.
- [121] D. Shepard. “A two-dimensional interpolation function for irregularly-spaced data”. In: *Proceedings of the 1968 23rd ACM national conference*. ACM Press, 1968, pp. 517–524.
- [122] S. E. Sherer and J. N. Scott. “High-order compact finite-difference methods on general overset grids”. In: *Journal of Computational Physics* 210.2 (2005), pp. 459–496.
- [123] S. J. Sherwin and G. E. Karniadakis. “A new triangular and tetrahedral basis for high-order (hp) finite element methods”. In: *International Journal for Numerical Methods in Engineering* 38.22 (1995), pp. 3775–3802.
- [124] C.-W. Shu. “High-order Finite Difference and Finite Volume WENO Schemes and Discontinuous Galerkin Methods for CFD”. In: *International Journal of Computational Fluid Dynamics* 17.2 (2003), pp. 107–118.

-
- [125] B. A. Singer, D. P. Lockard, and G. M. Lilley. “Hybrid Acoustic Predictions”. In: *Computers and Mathematics with Applications* 46.4 (2003), pp. 647–669.
- [126] S. A. Slimon, M. C. Soteriou, and D. W. Davis. “Computational Aeroacoustics Simulations Using the Expansion About Incompressible Flow Approach”. In: *AIAA Journal* 37.4 (1999), pp. 409–416.
- [127] G. P. Smith et al. *GRI-Mech 3.0*. URL: <http://combustion.berkeley.edu/gri-mech/> (visited on 2018-03-01).
- [128] C. K. W. Tam. “Recent advances in computational aeroacoustics”. In: *Fluid Dynamics Research* 38.9 (2006), pp. 591–615.
- [129] C. K. Tam. “Jet Noise: Since 1952”. In: *Theoretical and Computational Fluid Dynamics* 10.1-4 (1998), pp. 393–405.
- [130] C. K. Tam and J. C. Webb. “Dispersion-Relation-Preserving Finite Difference Schemes for Computational Acoustics”. In: *Journal of Computational Physics* 107.2 (1993), pp. 262–281.
- [131] C. Tam and K. Kurbatskii. “An optimized extrapolation and interpolation method for computational aeroacoustics”. In: *38th Aerospace Sciences Meeting and Exhibit*. January. American Institute of Aeronautics and Astronautics, 2000.
- [132] K. W. Thompson. “Time-dependent boundary conditions for hyperbolic systems, II”. In: *Journal of Computational Physics* 89.2 (1990), pp. 439–461.
- [133] K. W. Thompson. “Time dependent boundary conditions for hyperbolic systems”. In: *Journal of Computational Physics* 68.1 (1987), pp. 1–24.
- [134] E. F. Toro. *Riemann Solvers and Numerical Methods for Fluid Dynamics*. 3rd ed. Springer, 2009.
- [135] W. C. Ullrich, Y. Mahmoudi, K. Lackhove, A. Fischer, C. Hirsch, T. Sattelmayer, A. P. Dowling, N. Swaminathan, A. Sadiki, and M. Staufer. “Prediction of Combustion Noise in a Model Combustor Using a Network Model and a LNSE Approach”. In: *Journal of Engineering for Gas Turbines and Power* 140.4 (2017).
- [136] W. C. Ullrich, C. Hirsch, T. Sattelmayer, K. Lackhove, A. Sadiki, A. Fischer, and M. Staufer. “Combustion Noise Prediction Using Linearized NavierStokes Equations and Large-Eddy Simulation Sources”. In: *Journal of Propulsion and Power* 34.1 (2018), pp. 198–212.

-
- [137] G. Wang, L. N. Sankar, and H. Tadghighi. “Prediction of Rotorcraft Noise with a Low-Dispersion Finite Volume Scheme”. In: *AIAA Journal* 38.3 (2000), pp. 395–401.
- [138] M. Wang, J. B. Freund, and S. K. Lele. “Computational Prediction of Flow-Generated Sound”. In: *Annual Review of Fluid Mechanics* 38.1 (2006), pp. 483–512.
- [139] V. L. Wells and R. A. Renaut. “Computing Aerodynamically Generated Noise”. In: *Annual Review of Fluid Mechanics* 29.1 (1997), pp. 161–199.
- [140] F. A. Williams. *Combustion Theory (Combustion Science and Engineering)*. CRC Press, 1994.
- [141] A. Yoshizawa. “Statistical theory for compressible turbulent shear flows, with the application to subgrid modeling”. In: *Physics of Fluids* 29.7 (1986), pp. 2152–2164.